

A miniature atmospheric pressure glow discharge torch for
localized biomedical applications

Valérie Léveillé

Department of Chemical Engineering

McGill University

Dr. Sylvain Coulombe, Supervisor

A Thesis Submitted to the Faculty of Graduate Studies and
Research in Partial Fulfillment of the Requirements for the
Degree of Doctor of Philosophy

McGill University

Montréal, Canada

Valérie Léveillé

September 2006



Library and
Archives Canada

Bibliothèque et
Archives Canada

Published Heritage
Branch

Direction du
Patrimoine de l'édition

395 Wellington Street
Ottawa ON K1A 0N4
Canada

395, rue Wellington
Ottawa ON K1A 0N4
Canada

Your file *Votre référence*
ISBN: 978-0-494-27813-0
Our file *Notre référence*
ISBN: 978-0-494-27813-0

NOTICE:

The author has granted a non-exclusive license allowing Library and Archives Canada to reproduce, publish, archive, preserve, conserve, communicate to the public by telecommunication or on the Internet, loan, distribute and sell theses worldwide, for commercial or non-commercial purposes, in microform, paper, electronic and/or any other formats.

The author retains copyright ownership and moral rights in this thesis. Neither the thesis nor substantial extracts from it may be printed or otherwise reproduced without the author's permission.

AVIS:

L'auteur a accordé une licence non exclusive permettant à la Bibliothèque et Archives Canada de reproduire, publier, archiver, sauvegarder, conserver, transmettre au public par télécommunication ou par l'Internet, prêter, distribuer et vendre des thèses partout dans le monde, à des fins commerciales ou autres, sur support microforme, papier, électronique et/ou autres formats.

L'auteur conserve la propriété du droit d'auteur et des droits moraux qui protègent cette thèse. Ni la thèse ni des extraits substantiels de celle-ci ne doivent être imprimés ou autrement reproduits sans son autorisation.

In compliance with the Canadian Privacy Act some supporting forms may have been removed from this thesis.

Conformément à la loi canadienne sur la protection de la vie privée, quelques formulaires secondaires ont été enlevés de cette thèse.

While these forms may be included in the document page count, their removal does not represent any loss of content from the thesis.

Bien que ces formulaires aient inclus dans la pagination, il n'y aura aucun contenu manquant.


Canada

« Douter de tout ou tout croire sont les deux solutions également commodes qui l'une et l'autre nous dispensent de réfléchir »

Henri Poincaré

La Science et l'hypothèse

CONTRIBUTIONS OF THE AUTHOR

Article published in the “Plasma Sources Science and Technology” journal

This article was written by the Ph.D. candidate and is based on research work done during her Ph.D. project. The section “Impedance matching and plasma torch impedance measurements” was based on a collective work completed by the Ph.D. candidate’s supervisor, Prof. Coulombe, and the Ph.D. candidate.

Complete reference:

V Léveillé and S Coulombe, "Design and preliminary characterization of a miniature pulsed RF APGD torch with downstream injection of the source of reactive species," *Plasma Sources Science and Technology* **14** (3), 467-476 (2005).

Article accepted for publication in the “Measurement Science and Technology” journal

This article was written by the Ph.D. candidate and is based on research work done during her Ph.D. project. The sections “Circuit model” and “Determination of the resistive power” were based on a collective work done by the Ph.D. candidate and her supervisor, Prof. Coulombe.

Article accepted for publication in the “Plasma Processes and Polymers” journal

All the sections of this article were written by the Ph.D. candidate and are based on research work done during her Ph.D. project. The section called “The Effect

of He Flow rate” is the result of a collective work done by Prof. Coulombe and the Ph.D. candidate.

SUMMARY

This thesis presents the design and characterization of a novel pulsed miniature capacitively-coupled Atmospheric Pressure Glow Discharge Torch (APGD-*t*) aimed at localized biomedical applications. Amplitude modulation of the 13.56 MHz carrier signal allows to continuously vary the power level applied to the APGD-*t*. Typically, the APGD-*t* produces a plasma jet with a 150-500 μm diameter and ≈ 2.5 mm length. Helium (He) is the plasma-forming gas with a flow rate ranging from 0.5 to 1.5 slm. The use of a small capillary electrode enhances the electric field, lowering the breakdown voltage (typically 220 $V_{\text{pk-to-0}}$) and allows the injection of small amounts (0 - 50 sccm) of a source of reactive species (O_2) downstream of the plasma-forming region, in the plasma afterglow. The O_2 is electronically dissociated in the plasma afterglow to create atomic oxygen (O) with no effect on the electrical properties. A ratio of 0.3% $_{\text{v}}$ O_2/He generates a maximum in O production.

Careful electrical probe measurements and circuit analyses reveal the strong effect of commercial passive voltage probes on the total load impedance of the APGD-*t* circuit. The larger the probe capacitance and cable length, the larger the component of the phase angle between the load voltage and circuit current signals induced by the probe. The calibration of the phase angles induced by the voltage probes allows to estimate that a resistive power of $\sim 0.24 - 1$ W is dissipated in the APGD-*t* under nominal operating conditions.

The gas kinetic and atomic He excitation temperatures, and the electron density near the APGD-*t* nozzle exit are estimated at ≈ 323 K, ≈ 1914 K and $\approx 10^{11}$ cm^{-3} , respectively. This confirms that the APGD-*t* plasma jet near the nozzle exit is in a non-thermal equilibrium state. The emission spectroscopy study reveals the entrainment of air molecules (N_2 , O_2 and H_2O) in the plasma jet, and that their

excitation by the plasma creates new reactive species (O and OH). A preliminary survey of the chemical reactions taking place in the plasma afterglow reveals that metastable He as well as OH, O, O₂(a¹Δg), O₂(b¹Σg⁺), N₂, N₂⁺ and O₃ are plasma species that can reach and react with organic or biological surfaces located a few mm downstream of the APGD-*t* nozzle exit. This thesis demonstrates that the APGD-*t* is a promising tool for localized biomedical applications.

RÉSUMÉ

Cette thèse décrit le design et la caractérisation d'une mini-torche à plasma pulsé à couplage capacitif opérant à pression atmosphérique (APGD-*t*) pour des applications biomédicales de précision. Une modulation en amplitude du signal excité à 13.56 MHz permet de varier continuellement la puissance délivrée à l'APGD-*t*. Typiquement, l'APGD-*t* produit un jet de plasma de 150-500 μm de diamètre et ≈ 2.5 mm de long. L'hélium (He) est le gaz plasmagène avec un débit volumétrique variant entre 0.5 et 1.5 slm. L'utilisation d'un capillaire métallique comme électrode de puissance amplifie le champ électrique, permettant ainsi une faible tension de claquage ($220 V_{\text{crête-à-0}}$). Il permet aussi d'injecter une petite quantité (0 - 50 sccm) d'une source d'espèce réactive, l'oxygène moléculaire (O_2), en aval de la zone de formation du plasma (post-décharge). L' O_2 , injecté dans la post-décharge, est dissocié par impact électronique pour créer de l'oxygène atomique (O) et ce, en ne perturbant pas les propriétés électriques de l'APGD-*t*. Un ratio de $0.3\% \text{ v/v } \text{O}_2/\text{He}$ permet de maximiser la production d'O.

Des mesures électriques minutieuses et une analyse du circuit électrique de l'APGD-*t* révèlent que l'utilisation de sondes de voltage passives affecte l'impédance totale du circuit. En fait, plus grandes sont la capacité électrique et la longueur de câble de la sonde, plus grand est l'angle de phase mesuré entre le voltage appliqué sur l'APGD-*t* et le courant du circuit. La calibration de l'angle de phase mesuré permet de calculer que la puissance résistive dissipée dans l'APGD-*t* se situe entre ~ 0.24 et 1 W pour des conditions typiques d'opération.

Près de la sortie de la buse, la température cinétique des gaz plasmagènes, la température d'excitation de l'He et la densité électronique sont estimées à ≈ 323 K, ≈ 1914 K et $\approx 10^{11} \text{ cm}^{-3}$, respectivement. Ces estimés confirment que le plasma de l'APGD-*t* près de la buse est dans le régime hors équilibre thermique. La

spectroscopie d'émission révèle que les molécules de l'air (N_2 , O_2 et H_2O) sont entraînées dans le jet de plasma et que leur excitation par le plasma crée des radicaux libres (O et OH). Une étude préliminaire des réactions chimiques dans la post-décharge démontre que les metastables d'hélium ainsi que les espèces O , OH , $O_2(a^1\Delta_g)$, $O_2(b^1\Sigma_g^+)$, N_2 , N_2^+ et O_3 , susceptibles de réagir avec des surfaces organiques et biologiques situées à quelques mm de la sortie de la buse de l'APGD-*t*, sont produites. Cette thèse démontre que l'APGD-*t* est un outil prometteur pour des applications biomédicales de précision.

ACKNOWLEDGMENTS

First of all, I wish to express my profound gratitude to my supervisor, Prof. Sylvain Coulombe. His great knowledge of plasma physics, practical thinking, high scientific standards, open mind and availability allowed me to complete an innovative and challenging Ph.D. research project. Prof. Sylvain Coulombe, you really transformed my life during this Ph.D. journey.

Secondly, I would like to thank my family, Jacques Léveillé, Thérèse Nault and Yann Léveillé, for their continuous support provided during the last 3 ½ years. Even though they could not understand most of the science behind the project, they did understand its importance and my determination in using the science and engineering of plasmas to develop useful applications for the society. I am also thankful to Andy, my life partner, who gave me the necessary guidance to keep as concrete as possible the outcomes of the Ph.D. research project.

I'm also grateful to my research colleague, Ms. Sara Yonson, and to Prof. Richard Leask, with whom I shared interesting discussions on how the plasma can interact with bio/organic materials. Moreover, I want to express my appreciation to the technicians of our department, Lou Cusmich, Alain Gagnon, Gerald Lepkyj and Frank Caporuscio, who helped me so much to make the APGD-*t* and diagnostics set-up work! I also wish to thank the secretaries, Emily Musgrave, Louise Miller-Aspin, Jo-Ann Gadsby and Mélanie Gorman, who did an excellent work with the administrative tasks related to my Ph.D. project.

I wish to thank Mr. Joel Penelon, who assisted me during the construction of the impedance matching network, Mr. Leo Nikkinen for his precious advices on the radio-frequency systems and Dr. Gagik Nersysyan and Dr. Richard Engeln for their useful comments on the laser-induced fluorescence spectroscopy technique.

At last, I want to express my sincere appreciation to the institutions that founded this research project such as the Natural Sciences and Engineering Research Council of Canada (NSERC), through the Discovery, Canada Research Chairs and the Idea to Innovation programs, the Fonds québécois de la recherche sur la nature et les technologies (FQRNT), and of course, the Department of Chemical Engineering of McGill University through the Eugenie Ulmer Lamothe scholarship program.

LIST OF ABBREVIATIONS

AC: Alternative current

AM: Amplitude modulation

APC: Argon plasma coagulation

APG: Atmospheric pressure glow

APGD: Atmospheric pressure glow discharge

APGD-*t*: Atmospheric pressure glow discharge torch

APNTPs: Atmospheric pressure non-thermal plasma sources

APPJ: Atmospheric pressure plasma jet

APPs: Atmospheric pressure plasma sources

BNC: Bayonet Neill-Concelman

BW: Bandwidth

CCD: Charge-coupled device

CCP: Capacitively-coupled plasma

DAQ: Data acquisition

DBD: Dielectric barrier discharge

DC: Duty cycle

dc: Direct current

DNA: Deoxyribonucleic acid

EEDF: Electron energy distribution function

FM: Frequency modulation

GPIB: General purpose interface bus

HAAE-1: Human abdominal aortic endothelial cells

HepG2: Human hepatocellular liver carcinoma cells

ICP: Inductively-coupled plasma

IR: Infrared

LCIF: Laser collision-induced fluorescence

LIF: Laser-induced fluorescence

LSL: Laser stray light

mAPPs: Small-scale atmospheric pressure plasma sources

MFC: Mass flow controller

MHD: Magnetohydrodynamics

MN: Matching network

MPT: Microwave plasma torch

MW: Microwave

NdYAG: Neodymium-doped yttrium aluminum garnet

OES: Optical emission spectroscopy

OPG: Optical parametric generator

OPO: Optical parametric oscillator

PC: Personal computer

PCI: Peripheral component interconnect

PFI: Peak fluorescence intensity

PID: Proportional, integral and derivative

PMT: Photomultiplier tube

PVC: Polyvinyl chloride

RF: Radio-frequency

SEM: Scanning electron microscopy

SS: Steady-state

TALIF: Two-photon laser-induced fluorescence

USB: Universal serial bus

UV: Ultraviolet

UV-VIS: Ultraviolet - visible

VI: Virtual instrument

VUV: Vacuum ultraviolet

YAG: Yttrium-aluminum-garnet

μ -PJ: Micro plasma jet

TABLE OF CONTENTS

SUMMARY	iv
RÉSUMÉ	vi
ACKNOWLEDGMENTS	viii
LIST OF ABBREVIATIONS.....	x
TABLE OF CONTENTS.....	xiii
LIST OF FIGURES	xviii
LIST OF TABLES.....	xxii
CHAPTER 1	5
REVIEW OF LITERATURE	5
1.1. Atmospheric pressure non-thermal plasmas	5
1.2. Small-scale atmospheric pressure plasma sources.....	9
1.3. Plasma sources for biomedical applications	14
1.4. Electrical characterization.....	17
1.5. Optical emission spectroscopy.....	19
1.6. Laser-induced fluorescence spectroscopy.....	21
CHAPTER 2	30
DESIGN AND CHARACTERIZATION OF THE APGD- <i>t</i>	30
2.1 Abstract	32

2.2 Introduction.....	33
2.3 The APGD- <i>t</i>	35
2.3.1 Design rationale	35
2.3.2 Details of the construction	37
2.3.3 Flow conditions.....	39
2.3.4 Auxiliary equipments.....	39
2.4 Results and discussion	41
2.4.1 Breakdown voltage	42
2.4.2 Impedance matching and plasma torch impedance measurement	43
2.4.3 Effect of duty cycle.....	48
2.4.4 Effect of O ₂ addition.....	50
2.4.5 Other species.....	56
2.4.6 He excitation temperature.....	56
2.5 Conclusions.....	58
2.6 Acknowledgments.....	59
2.7 References.....	59
CHAPTER 3	60
DETAILED ASSESSMENT OF THE APGD- <i>t</i> ELECTRICAL CHARACTERISTICS	60
3.1 Abstract	61

3.2 Introduction.....	62
3.3 Calibration of the phase angle.....	64
3.3.1 Circuit model	65
3.3.2 Experimental set-up	67
3.3.3 Results and analysis	67
3.4 Application.....	72
3.4.1 Measurements	73
3.4.2 Determination of the resistive power	74
3.5 Conclusions and recommendations.....	78
3.6 Acknowledgments.....	79
3.7 References.....	79
CHAPTER 4	80
ATOMIC OXYGEN PRODUCTION & PLASMA AFTERGLOW CHEMISTRY	80
4.1 Summary	81
4.2 Introduction.....	82
4.3 Experimental part.....	83
4.4 Results and discussion	86
4.4.1 Optimization of the atomic oxygen production	86
4.4.2 Effect of O ₂ flow rate.....	88

4.4.3 Effect of He flow rate.....	91
4.5 Afterglow plasma chemistry	95
4.6 Conclusions.....	105
4.7 Acknowledgments.....	106
4.8 Collected references.....	106
CHAPTER 5	107
ATTEMPT TO USE THE LASER-INDUCED FLUORESCENCE SPECTROSCOPY TECHNIQUE FOR MEASUREMENT OF THE METASTABLE HE ATOM DENSITY.....	107
5.1 Introduction.....	107
5.2 Experimental set-up	108
5.3 Results and discussion	112
5.4 Conclusions.....	113
FINAL CONCLUSIONS.....	115
CONTRIBUTIONS TO KNOWLEDGE	117
RECOMMENDATIONS FOR FUTURE STUDIES	119
APPENDIX A : ELECTRIC FIELD CALCULATIONS.....	123
APPENDIX B : THE LABVIEW™ INTERFACE.....	125
APPENDIX C : EFFECT OF THE EXCITATION FREQUENCY ON THE APGD- <i>t</i> CHARACTERISTICS.....	130

BIBLIOGRAPHY..... 135

LIST OF FIGURES

Figure 1-1: Schematic of an inductively-coupled plasma torch for mass spectroscopy [4].	10
Figure 1-2: Schematic of a capacitively-coupled plasma torch with concentric electrodes [5].	10
Figure 1-3: Schematic of a single hollow cathode torch [5].	11
Figure 1-4: Schematic of the “torche à injection axiale” MPT [5].	12
Figure 1-5: Picture of the micro-plasma jet (μ -PJ) developed by Yoshiki <i>et al.</i> [11]	13
Figure 1-6: Picture of the small-scale MPT developed by Stonies <i>et al.</i> [15].	14
Figure 1-7: Picture of the Plasma Needle developed by Stoffels <i>et al.</i> [29].	16
Figure 1-8: Energy level diagram for helium. The wavelength units are Angström [69].	27
Figure 1-9: Dominant processes for LIF measurement of the He(2^3S) state in He plasmas.	28
Figure 2-1: a) Schematic of the APGD- <i>t</i> construction. b) Picture of the APGD- <i>t</i> operating with 1 slm He at ≈ 1 W. c) Picture of the APGD- <i>t</i> nozzle area (the silver epoxy was removed to reveal the capillary electrode).	36
Figure 2-2: Schematic of the experimental set-up.	41
Figure 2-3: Representative example of the RF circuit current (<i>i</i>) and voltage pulses (V_T) applied to the APGD- <i>t</i> operating with 1 slm He and 10 % duty cycle.	42

Figure 2-4: Schematic of the electrical circuit.....	43
Figure 2-5: One cycle of the RF current (i) and voltage (V_T) signals applied to the APGD- t operating with 1 slm He.....	46
Figure 2-6: Contour plot of the modulus of the torch-passive voltage probe system complex impedance, ($ Z_{T+p} $), and phase shift (ϕ) versus the torch resistance (R_T) and capacitance (C_T).....	48
Figure 2-7: APGD- t power, P_T [W] (o), gas temperature, T [°C] (Δ), and exposure time to skin, t_e [s] (\square), versus the RF pulse duty cycle for 1 slm He.	49
Figure 2-8: Telemicroscopic images of the plasma jet for $P_T \approx 1$ W. a) 1 slm He, b) 1 slm He with 10 sccm O_2 in the capillary electrode, and c) 1 slm He + 1 v/v% O_2 as plasma-forming gas.....	51
Figure 2-9: Emission spectra of the plasma jet ~ 1 mm downstream of the nozzle exit plane for $P_T \approx 1$ W. a) 1 slm He, b) 1 slm He with 10 sccm O_2 in the capillary electrode, and c) 1 slm He + 1 v/v% O_2 as plasma-forming gas. ..	54
Figure 2-10: Axial profiles of the peak intensity of selected emission lines for $P_T \approx 1$ W. a) 1 slm He with 10 sccm O_2 in the capillary electrode: N_2 (—) at 337 nm, N_2^+ (o) at 391 nm, He (\square) at 587 nm and H_α (Δ) at 656 nm. b) O emission at 777 nm for 1 slm He (-), 1 slm He with 10 sccm O_2 in the capillary electrode (\blacksquare), and 1 slm He + 1v/v% O_2 as plasma-forming gas (\blacktriangle).....	55
Figure 2-11: Boltzmann plot obtained for $P_T \approx 1$ W, 1 slm He and three different distances from the nozzle exit: -0.25 mm (\square), 0 mm (Δ) and 0.25 mm (\circ). The average excitation temperature is 1573K ($R^2=0.88$).....	57
Figure 3-1: Schematic of the model electrical circuit.	66

Figure 3-2: Frequency response of the impedance magnitude and phase angle for a voltage probe model with $R_p = 10 \text{ M}\Omega$ and $C_p = 2.75 \text{ pF}$: Z_p and θ_p (—) and for a resistor + voltage probe model with $R = 1000 \text{ }\Omega$: Z_{R+p} and θ_{R+p} (— - —). 68

Figure 3-3: Phase angle between i and V_R for the P6139A (\blacklozenge : model, \diamond : measured) and the P5100 (\blacksquare : model, \square : measured) probes with respect to the load resistance at 13.56 MHz. 69

Figure 3-4: Relative phase angle $\Delta\theta_{R+p}$ introduced by the difference in cable lengths (current and voltage probes) for the (\diamond) P6139A probe and the P5100 probe with (\square) $C_p = 2.75 \text{ pF}$ and (\circ) $C_p = 4 \text{ pF}$ at 13.56 MHz. 70

Figure 3-5: Phase angle between i and V_R for the P6139A probe (\diamond : measured and corrected, \blacklozenge : model) and the P5100 probe (\circ : measured and corrected, \bullet : model) as a function of load resistance at 13.56 MHz. 71

Figure 3-6: V_T (—) and i (- - -) waveforms for the APGD- t excited at 13.56 MHz. 74

Figure 3-7: Schematic of the electrical circuit of the APGD- t 75

Figure 4-1: a) Schematic of the APGD- t , b) pictures of the APGD- t and c) the APGD- t plasma jet impinging on the forefinger. 84

Figure 4-2: Pictures of the plasma jet produced by the APGD- t at $\approx 1 \text{ W}$ for different He flow rates. 87

Figure 4-3: a) Normalized peak line emission intensity of O at 777 nm (\circ), He at 706 nm (\square) and N_2^+ at 391 nm (\diamond) near the nozzle exit, and b) torch voltage V_T (\square) and circuit current i (\circ) and their relative phase angle (Δ) for different O_2 flow rates in the capillary electrode. 90

Figure 4-4: Axial distribution of the normalized peak emission intensity of a) O at 777 nm), b) He at 706 nm, c) N₂ at 337 nm and d) N₂⁺ at 391 nm for 0.5 (o), 0.75 (◊), 1 (□), 1.25 (Δ) and 1.5 (+) slm of He..... 93

Figure 5-1: Diagram of the LIF experimental set-up. 109

Figure 5-2: Time diagram of the laser synchronization with the plasma modulation signal..... 111

LIST OF TABLES

Table 1-1: Classification of atmospheric pressure non-thermal plasma sources [1].	8
Table 2-1: He excitation temperature (T_{exc}) for different plasma gas compositions and torch power levels.....	58
Table 4-1: Reactions occurring in the plasma glow and afterglow, with their respective rate constants calculated for specific T_e or T_g	97
Table 5-1: LIF signal measured at two different distances from the nozzle exit.	112
Table A-1: Data for the calculation of the electric field distribution.	123
Table C-1: APGD- t characteristics at different plasma excitation frequencies. .	132

INTRODUCTION

In this introduction, the rationale and objectives of the Ph.D. project are presented, as well as the structure of the thesis. The Ph.D. thesis is a manuscript-based document, where essentially, each chapter corresponds to one article published or accepted for publication in an international journal.

a. Rationale and objectives

A decade ago, very few plasma sources for localized biomedical applications were reported and neither conference nor workshop was organized on the matter. Nowadays, we find a dozen plasma sources developed in various laboratories for localized biomedical applications, while some have already been commercialized. The interest in those plasma sources is correlated to the phenomenal diversity of their applications and to their unique capabilities.

During the Ph.D. project, a new plasma source was developed to surpass the capability of the existing bench scale and commercial plasma sources developed for localized biomedical applications. Amongst the technological limitations of the existing plasma sources are 1) the use of heat, 2) the transfer of an electrical current to the biological surface, 3) the failure to treat surface areas less than 1 mm, 4) the impossibility to treat complex (i.e. three dimensional) geometries and finally, 5) the incapacity to inject various chemical species in the plasma without perturbing its electrical characteristics and stability.

The plasma source developed in this project permits the injection of any chemical species in the plasma in order to treat areas of less than 500 μm width on biological or organic surfaces with any type of geometries and without heat damage, electrical coupling with the surface or perturbation of the plasma

electrical characteristics and stability. The developed plasma source was named the Atmospheric Pressure Glow Discharge torch, APGD-*t* in short, and this document reports on all the development steps and characterization work.

The main objective of the Ph.D. project was to develop, characterize and assess the performance of the APGD-*t* meant for localized biomedical applications. The construction of this new plasma source opened the door to a wide and fascinating field of study, including the afterglow plasma chemistry and plasma interactions with biological and organic materials, which subjects are likely to be investigated by plasma scientists for many more decades.

b. Description of the thesis

This thesis is a manuscript-based document containing three articles published or accepted for publication. The thesis is structured so that one chapter is associated to one article. At the beginning of each chapter, a short text is written to introduce the content of the chapter and to connect the chapters together. Each chapter encloses the text of an original article, although the actual location of the figures and tables differs from the publisher's presentation (for the Plasma Sources Science and Technology article). The numbering of the figures, tables and references is also different from the one seen in the original articles so as to produce a single, clear and ordered document.

In order to abridge the thesis, the list of references associated to each article has been withdrawn from the individual chapters and compiled as a global list of references situated at the end of the thesis. Lastly, appendices are presented at the end of the thesis to describe additional substantial work done during the Ph.D. project, but not presented in the articles.

The first chapter consists of a literature review divided in two parts. A first part describes various non-thermal plasma sources operating at atmospheric pressure, plasma sources developed for small-scale applications, and plasma sources developed for localized biomedical applications. The second part reviews the electrical and optical measurement techniques used to characterize plasma sources with an emphasis on their limitations.

In the second chapter, the design and a preliminary characterization of the plasma source developed during the Ph.D. project are presented. This chapter is composed of an article published in the *Plasma Sources Science and Technology* journal in August 2005.

The third chapter details a method to calibrate the phase angle that appears between the load voltage and the circuit current due to the use of commercial passive voltage probes. Such method is used to calculate the power dissipated in the plasma source. This chapter consists of an article accepted for publication in the *Measurement Science and Technology* journal in September 2006.

The fourth chapter presents a parametric optimization study for the production of atomic oxygen. It also presents a survey of the afterglow plasma chemistry in order to identify the reactive species possibly reaching and reacting with biological or organic surfaces located a few mm downstream of the nozzle exit. This chapter consists of an article accepted for publication in the *Plasma Processes and Polymers* journal in August 2006.

The fifth chapter reports on an attempt to use the laser-induced fluorescence spectroscopy technique to investigate the helium metastable states in the plasma afterglow. Since the technique was not successful with the current APGD-*t* set-up, comments are made on the technical difficulties encountered and recommendations are presented in order to improve the technique.

Finally, general conclusions and recommendations for future work are presented.

The appendices regroup research works that have not been published or accepted for publication in articles. However, they are complementary research outcomes of the Ph.D. project. In appendix A, the radial electric field distribution in the plasma glow and at the nozzle exit of the plasma source is presented. Appendix B presents the LabVIEW™ interface developed for the monitoring and control of the plasma source, and the instruments used. Appendix C presents the APGD- t characteristics obtained using excitation frequencies of 10 kHz, 65 kHz and 13.56 MHz to excite the plasma.

CHAPTER 1

REVIEW OF LITERATURE

This literature review has two main sections. The first section presents a non-exhaustive review of the existing atmospheric pressure non-thermal plasma sources, micro-plasma sources and plasma sources developed specifically for localized biomedical applications.

The second section reviews some current techniques used to obtain the electrical characteristics of plasma sources as well as two spectroscopic techniques, namely the optical emission and laser-induced fluorescence spectroscopy techniques.

1.1. Atmospheric pressure non-thermal plasmas

Plasmas are omnipresent in the visible universe: they represent 99% of it. They are called ionized gases since they consist of a mixture of electrons, ions and neutrals (atoms and molecules), which are in their fundamental and excited states. Plasmas contain free charge carriers and are thus electrically conductive; though at the macroscopic level, they are electrically neutral (the positive and negative charge densities are balanced). Plasmas are generated when electrical energy is provided to a gaseous specie, which modifies its electronic structure and produces excited and ionized states.

Depending on the way the plasmas are generated and sustained, they can be classified as thermal or non-thermal (“cold”). The two main properties which allow classifying the various plasmas are the electron density and temperature. Atmospheric pressure thermal plasmas have a high electron temperature, T_e , (~5000 – 500 000 K), which is similar to the gas kinetic temperature, T_g , and their

electron density ranges between 10^{18} and 10^{26} m^{-3} . The T_e of atmospheric pressure non-thermal plasmas ($\sim 1000 - 50\,000 \text{ K}$) is much higher than their T_g ($\sim 300 - 2000 \text{ K}$) [1] and their electron density is usually less than 10^{19} m^{-3} [2].

Atmospheric pressure plasma sources (APPs) possess some advantages over low-pressure plasmas that are relevant to this project. For instance, the generation of low-pressure plasmas requires many pieces of equipment (i.e. vacuum pump, sealed vessel), which greatly increase the infrastructure and operation costs of the plasma system. Moreover, more materials can be processed with APPs since no vacuum vessel limits their size or geometry. Finally, a particular important feature of APPs, is the fact that atmospheric pressure conditions do not damage mechanically sensitive materials such as biological samples. Indeed, important gradients of pressure across the cellular membrane can cause its rupture. Many applications, first developed with low-pressure non-thermal plasmas, are now being developed using APPs as it will be seen in sections 1.2 and 1.3 of this literature review.

Habitually, low-pressure plasmas are non-thermal because the collisions between electrons and heavy particles are mainly inelastic (excitation and ionization) and the efficiency of the momentum transfer between the electrons and the heavy species is low, resulting in low gas heating. When the plasma pressure increases, the rate of elastic collisions between electrons and heavy particles increases, bringing the plasma closer to the thermal equilibrium state. However, an exception exists for the APPs, because they can remain non-thermal. Indeed, if strong gradients of plasma properties (i.e. particle density and temperature, electric field) exist in the APPs, the thermal equilibrium between the electrons and heavy particles is refrained. The departure from the thermal equilibrium state is particularly strong in APP jets, where strong gradients of electron density and

temperature exist, and thus the high-energy electrons are found in the plasma jet core and the low-energy heavy particles are found in the plume.

As can be seen in Table 1-1, atmospheric pressure non-thermal plasma sources (APNTPs) can be classified according to the excitation frequency (f [kHz]) of the voltage applied on the discharge, since this parameter strongly influences the velocity of the free charge carriers (ions and electrons), and consequently the conditions leading to the production of excited and ionized species. The two main types of excitation are the direct current (dc), including steady state (SS) and pulsed voltages, and the alternative current (AC), including the low frequency (<100 kHz), radio-frequency (RF) (100 kHz-100 MHz) and microwave (MW) (>100 MHz) ranges. At very low f , electrons and ions follow the oscillations of the electric field. At RF, only electrons follow the electric field oscillations, while ions are influenced by the averaged temporal value of the electric field in the plasma. Finally, at MW frequencies, the phenomenon observed at RF is amplified and the non-thermal equilibrium is more pronounced.

Beside the f parameter, (Table 1-1 presents typical properties and parameters of plasma sources), other important parameters include the power density (P , [W/cm³]), reduced energy loading (PV/Q , [J/L], V , [cm³], Q , [L/s]: gas flow rate), maximum gas kinetic temperature (T_{\max} , [K]), gas flow velocity (U , [m/s]) and the discharge electrode gap (D , [mm]).

Several experimental techniques are available to allow APNTPs to reach a non-thermal equilibrium state: 1) limiting the transit time of the gas in the plasma region (less heat is deposited in the gas), 2) using cooled electrodes and vessel walls to increase the diffusional cooling of the gas, and 3) pulsing the power dissipated in the plasma. On one hand, if T_g is controlled by diffusional cooling, the maximal temperature is found in the center of the plasma (the furthest point from the cooling objects). On the other hand, if T_g is cooled by limiting the

transient time of the gas in the plasma, its value increases, while passing across the plasma volume and reaches a maximum at the plasma end.

Table 1-1: Classification of atmospheric pressure non-thermal plasma sources [1].

Discharge type	PV/Q (J/L)	P (W/cm ³)	T _{max} (K)	U (m/s)	D (mm)	f (kHz)
Pulsed corona	0.1-100	1-50	≈298	≤ 50	≤ 350	1-1000
Pulsed glow	100-500	10-500	≤ 600	10-200	10-50	0.05-5
Glow	1-100	50-500	≈298	10-150	5-20	SS
Micro-hallow cathode	-	≤10 ⁴	≈ 2000	Slow	1-2	SS, RF
Plasma torch	-	≈10 ⁴	≈ 3000	100	20	SS
DBD	-	1-50	≈298	Slow	1-5	0.05-100
RF	-	3-30	≤ 600	5-10	1-2	13560
MW	-	-	-	≈ 10	-	2.45x10 ⁶

Several interesting applications have been developed for the APNTPs. However for the scope of this project, the following section reviews only the APNTPs developed for small-scale applications reported in the published literature.

1.2. Small-scale atmospheric pressure plasma sources

Over the last two decades, numerous small-scale atmospheric pressure plasma sources (mAPPs) have been developed and commercialized worldwide. The first workshop on the subject, “The New World of Microplasmas”, was hosted in February 2003 by Professor Tachibana (Kyoto University) in Hyogo. Since then, two international workshops have been organized (2nd International Workshop on Microplasmas (IWM), October 2004, New Jersey and the 3rd IWM, May 2006, Greifswald).

Microplasmas (also called microcavity plasmas or microdischarges) are characterized by plasma dimensions smaller than 1 mm and operating pressures up to and above atmospheric pressure. In addition, the cathode fall dimension is usually similar to the microcavity radius. On one hand, the short transient time of the gas in the microplasmas and large ratio of reactor wall area to plasma volume result in low gas kinetic temperature (~300 – 2000 K). On the other hand, these characteristics permit the development of strong electric field gradients, which leads to relatively higher electron densities (10^{21} - 10^{22} m⁻³) [3] compared to the large-scale APNTPs. Also, due to the strong electric field gradients, the distribution of the electron energy tends to be non-Maxwellian.

The mAPPs are attracting a growing number of researchers due to their ease of construction and recently discovered applications. Different mAPPs configurations, which lead to the production of a small plasma jet, are now briefly described. Inductively-coupled plasma torches consist of an electrode, which is a coil of flat metal wound like a spiral or a spring around a plasma chamber as it is demonstrated in Figure 1-1. Plasma-forming gases flow inside the chamber and a small plasma jet is produced at the exit of the plasma chamber nozzle.

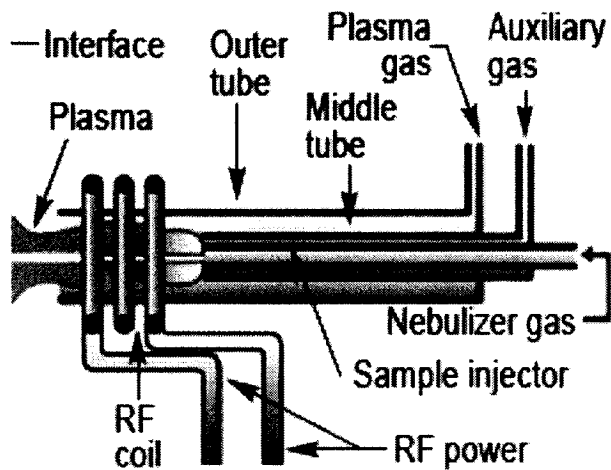


Figure 1-1: Schematic of an inductively-coupled plasma torch for mass spectroscopy [4].

Capacitively-coupled plasma torches have two electrodes. In rectangular reactors, electrodes are flat and located on opposite sides of the reactor. In cylindrical reactors, electrodes can be in concentric configuration or they are two sheets of metal wound around the reactor at different locations, which delimit the plasma volume. An example of a concentric electrodes configuration is illustrated in Figure 1-2. The plasma-forming gases flow in the inter-electrode gap and produce a small plasma jet at the torch nozzle exit.

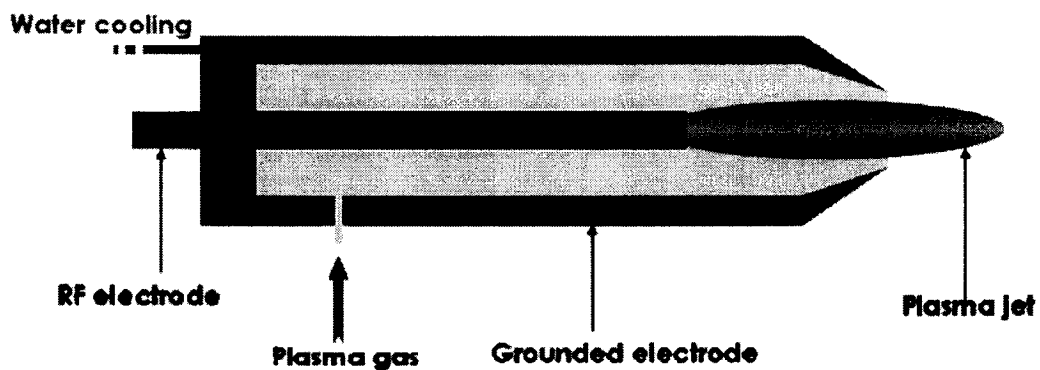


Figure 1-2: Schematic of a capacitively-coupled plasma torch with concentric electrodes [5].

Single hollow cathode torches can also produce small plasma jets. As presented in Figure 1-3, the hollow electrode acts as the inlet channel nozzle for the plasma-forming gases. When the speed of the plasma-forming gases is high enough, a small plasma jet outside the sharp top of the needle is produced.

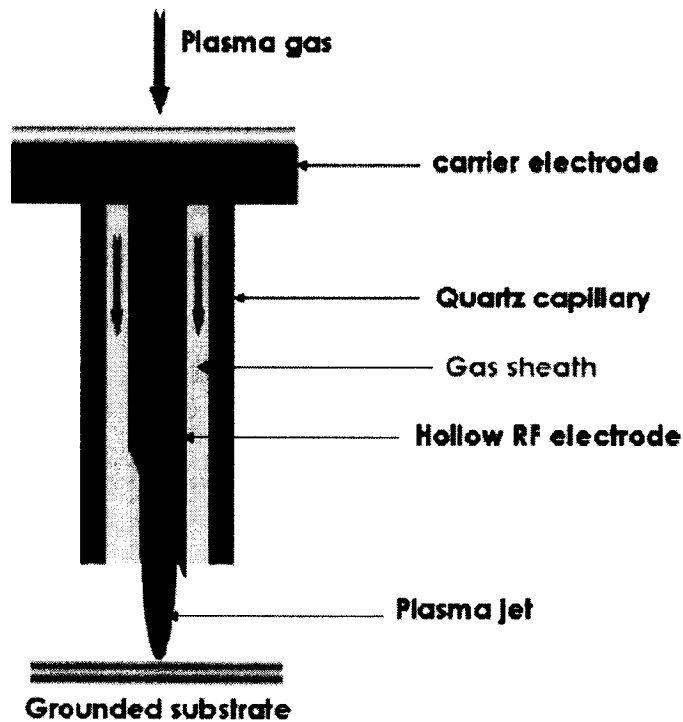


Figure 1-3: Schematic of a single hollow cathode torch [5].

Microwave plasma torches (MPTs) are also developed to produce small-scale plasma jets. In the configuration as seen in Figure 1-4, the plasma-forming gases flow inside an inner coaxial conductor and exits through a nozzle exit.

At the laboratory scale, several mAPPs torches have been developed for various applications. Amongst them, a miniature inductively-coupled plasma (ICP) torch using an Ar/halogen gas mixture was developed for local and high rate etching of silicon wafers [6].

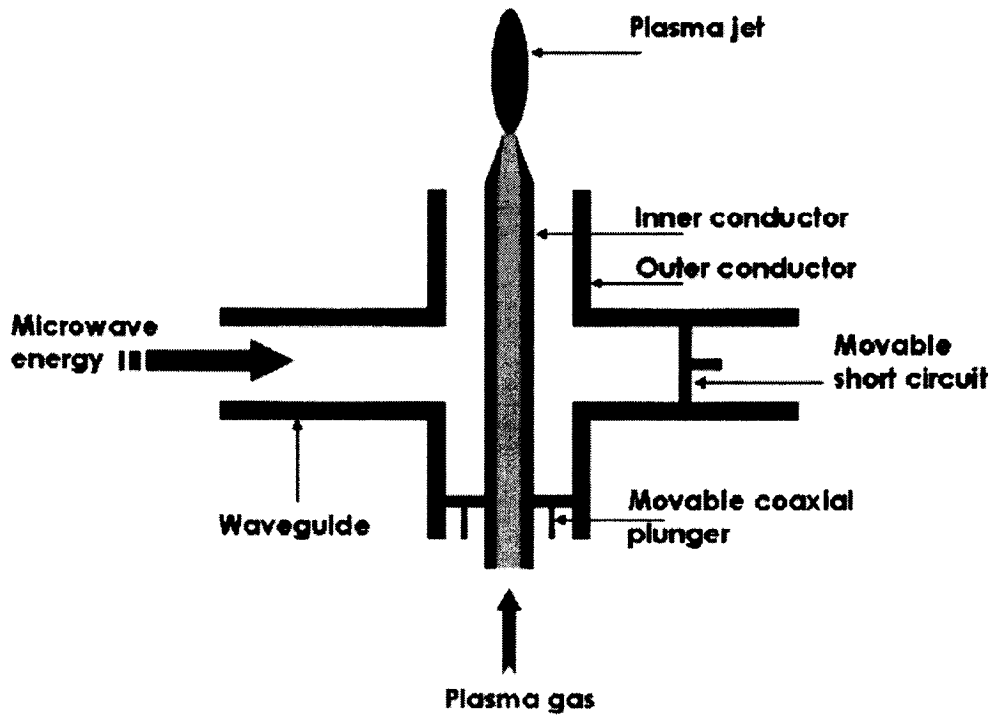


Figure 1-4: Schematic of the “torche à injection axiale” MPT [5].

Miniature capacitively-coupled plasma (CCP) torches, using a mixture of He with an halogen gas or oxygen, have also been developed for the local etching of silicon [7] and polyimide [8], the treatment of heat sensitive materials [9], and for the depletion of contaminants present in liquid hydrocarbons [10]. Several mAPPs with a single hollow cathode electrode configuration were also reported. The μ -plasma jet from Yoshiki *et al.* was used for local removal of photoresist [11] (see Figure 1-5). The single electrode configuration was also used for silicon oxidation and synthesis of carbon nanostructures [12], restoration of archeological glass and metal artifacts, fragmentation of molecules for micro-electrophoresis and plasma polymerization [13].

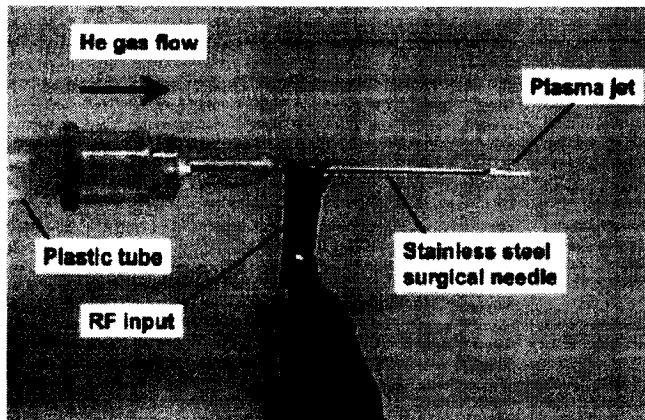


Figure 1-5: Picture of the micro-plasma jet (μ -PJ) developed by Yoshiki *et al.*[11]

The small MPT were developed as excitation sources for atomic spectroscopy for remote analytical system [14-16]. One example is the MPT developed by Stonies *et al.* (see Figure 1-6). The commonalities amongst those sources are: 1) the high-frequency excitation (RF or MW, except for [10]) which favors the formation of a non-thermal plasma at atmospheric pressure under low-voltage excitation conditions (few hundreds volts); 2) the use of He or Ar as the main plasma-forming gas, 3) the use of minute amounts of an additional gas as the source of reactive species, and 4) the torch configuration which permits the rapid transport of excited species to the surface of interest in remote exposure applications.

To date, several mAPPs have been commercialized to produce small non-thermal plasma streams. To name of few, the handheld PlasmaPenTM [17] and Plasmabrush® [18] are used to modify, coat or clean heat-sensitive surfaces.

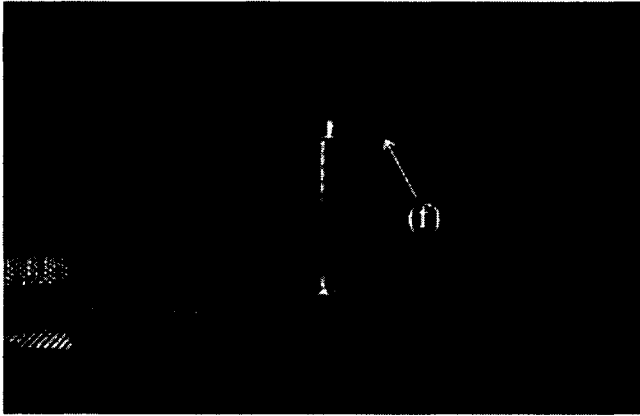


Figure 1-6: Picture of the small-scale MPT developed by Stonies *et al.* [15].

1.3. Plasma sources for biomedical applications

The interest in plasma sources specifically designed for the treatment of organic and biological materials has grown significantly over the last decade. The plasma-based treatments so far developed aim at chemical modification and cleaning of surfaces and deposition of organic or inorganic films. A few examples of chemical modification of surfaces are *in-vitro* or *in-vivo* modification of biological tissues and surface functionalization of polymeric surfaces. As for surface cleaning, examples are the sterilization of polymers and metals. Finally, deposition of inorganic films is used to enhance cell adhesion to surfaces.

Low-pressure plasmas are commonly used for surface functionalization. For instance, a two-step plasma process was developed to functionalize different polymeric materials [19]. A low-pressure ammonia MW plasma was used to functionalize a polymeric surface. A “passivation” step followed, where a hydrogen plasma flowed through a mask located above the functionalized surface to remove functional groups at specific locations and creating inhospitable micro-patterns for cell adhesion. Thin films of diamond-like carbon and silicon were

also deposited on a surface using a low-pressure plasma and a mask to create micro-patterns for selective attachment of neuronal networks [20].

The development of non-thermal plasmas operating at atmospheric pressure has increased the number and diversity of possible biomedical applications. As a result, APNTPs are currently being tested for sterilization [21,22], surface functionalization [23], microcontact printing of proteins onto polymer substrates [24] and preparation of drug delivery systems [25].

The development of such plasma sources is not without challenges. The most important difficulties encountered are: 1) the difficulty to sustain a stable and uniform glow discharge over large surface areas in film deposition and surface functionalization; 2) the need to maintain a high degree of non-thermal equilibrium to minimize the thermal load to the substrates of interest, while maintaining a high degree of chemical reactivity, and 3) the extremely rapid recombination of the reactive species in the plasma afterglow when a torch configuration is used.

Some mAPPs have been reported for clinical medical applications since the early 1990's. One of them is the argon plasma coagulation (APC) device, which uses a small rod as the powered electrode, while the patient is used as the ground electrode. It was commercialized as a small-scale electrocoagulation tool [26]. The APC produces an electrical discharge between the electrode and the lesion which desiccates, coagulates, and devitalizes through heat effects [27,28]. It was demonstrated through clinical trials that the APC caused significantly less damage to tissues than YAG lasers.

Several experimental techniques (refer to section 1.1 for more details) are used to bring down the T_g close to room temperature, which allows an even broader range of biomedical applications. It enables the treatment of extremely heat-sensitive materials such as living cells and tissues. For instance, Stoffels *et al.* [29-32]

developed an atmospheric pressure single electrode RF torch, the Plasma Needle, operating at power levels ranging from 10-100 mW, for localized bio-applications. A picture of the Plasma Needle is shown in Figure 1-7. Tests performed on hamster ovarian and human cells of lung carcinoma showed that the plasma was temporarily altering the cells' adhesion molecules, leading to cell-detachment without necrosis. The authors of the study proposed that plasma-produced radicals and UV radiation are responsible for the detachment mechanism.

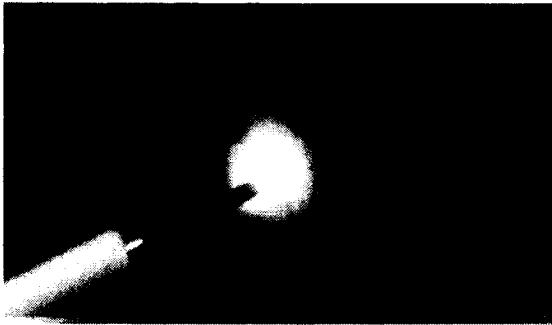


Figure 1-7: Picture of the Plasma Needle developed by Stoffels *et al.*[29].

Both devices just described (i.e. the APC and the Plasma Needle) involve some degree of electrical coupling of the plasma source with the surface. Moreover, the very low-power plasma generated by the Plasma Needle will probably be quenched when sources of reactive species are added in the plasma-forming region. Also, its open configuration, as oppose to a confinement tube with a nozzle exit, does not favor the transport of reactive species to a remote surface.

Several new mAPPs are reported every year. As an example, lately, the so-called Plasma Pencil, has been developed by Laroussi and Hue [33] for local biomedical applications. Finally, a mAPPs developed for esthetic applications, the

Portrait@PSR³ [34], has been commercialized for skin regeneration and removal of aged stains and wrinkles by use of plasma.

1.4. Electrical characterization

Electrical measurements are essential to characterize plasma sources. Nowadays, a variety of instruments are commercially available ranging from voltage, current and Langmuir probes [35,36] to integrated monitoring devices such as impedance monitors [37], power meters ([38], [39], [40] and [41]) and network analyzers. Electrical measurements are invasive by their very nature and special precautions are taken to minimize the effects on the measurements and/or to account for these effects. This task is particularly challenging with today's miniature capacitively-coupled plasma sources, which represent, most often, high capacitive loads due to the small inter-electrode gaps used, the high excitation frequency (MHz to GHz) and the comparatively small resistive impedance.

Some of the most useful measured electrical plasma properties are the power delivered to the electrical circuit driving the plasma load and the power dissipated in the plasma. Common instruments used to evaluate those power levels are bi-directional power meters and electrical probes. Some examples of their applications to small-scale plasma sources follow. The power meters can be used for monitoring the reflected power during plasma etching, thus providing a simple and inexpensive tool for end-point detection [42]. Stonies *et al.* [15] used a power meter to match a small microwave plasma torch (MPT) impedance to the generator's 50 Ω output impedance using microstrip circuits. Kieft *et al.* [31] used a power meter to optimize the matching network of the Plasma Needle excited at 13.56 MHz. Another power meter, the Z-scan® RF probe [43], was used by Zhu *et al.* [44] to characterize an atmospheric pressure plasma jet (APPJ) excited at 13.56 MHz. Though very useful, power meters have some drawbacks. They tend

to be expensive, they generally have a narrow measurement range and frequency bandwidth, and usually, they are not designed to measure low-level and/or pulsed powers. Moreover, only the high-end power meters can display signal waveforms, which are good indicators of signal distortion, saturation and arcing phenomena.

The use of current and voltage probes in combination with a fast digital oscilloscope appears to be an inexpensive and easy to set up method to electrically characterize miniature plasma sources ([9], [45] and [46]). Such probes are used to quantify breakdown, sustaining and operating voltages, circuit current and the relative phase angles between the circuit current and the load voltage signals. They have wide measurement ranges and bandwidths, but they too have some drawbacks. One of their major downsides is the voltage probe capacitive loading. Indeed, when a voltage probe is connected to a load circuit, the probe capacitance adds a reactive impedance to it, which induces an additional phase angle between the circuit current and the load voltage. The probe loading can also reduce the measured signal amplitude depending on the frequency at which the circuit is excited.

A second negative effect of voltage probes is the systematic time delay Δt induced by the length of the probe cable. This latter delay is constant in the time domain, but its equivalent phase angle $\Delta\theta$ between the circuit current and the load voltage signals increases with the excitation frequency f , as revealed by $\Delta\theta = (360^\circ)f\Delta t$. The consequence is a misreading of the phase angle induced only by the capacitive or inductive nature of the load resulting in a deterioration of the accuracy on the calculations relying on that measured phase angle. One of the standard procedures to calibrate the phase angle between signals measured by current and voltage probes is to take the difference in their nominal propagation time delays, as provided by the probe manufacturer, subtract this value from the measured time delay, and convert it into a phase angle. The accuracy of this

method relies strongly on the uncertainty of the probe characteristics given by the manufacturer. A more reliable method to calibrate the phase angle was used by Sobolewski *et al.* [47]. Instead of taking the propagation time delay given by the manufacturer, they measured *in situ* the time delay induced by the probe capacitance and cable length.

1.5. Optical emission spectroscopy

Optical emission spectroscopy (OES) is a technique widely used to characterize plasmas and the species present in them. A thorough description of this technique can be found in several books such as in the book of Vacquié [48]. In this section, a short description of the OES principles and instrumentation is presented, along with a method to estimate the electronic temperature in the plasma.

OES is a non-intrusive, easy-to-use and relatively sensitive technique. The basic principle of OES lies in the fact that when a material is heated to incandescence, the atoms are excited to elevated electronic states. When the excited electrons fall to lower energy states, photons with energy equal to the energy difference between the excited and lower states are emitted. The emitted light is characteristic of the material being probed and consequently, can be used for identification and sometimes quantification purpose. Therefore, plasmas, which are electronically heated, host a variety of excited species and are ideal media for OES.

The core of the OES detection system consists of a spectrometer, which is used to disperse the incoming light. Early spectrometers were composed of a prism that breaks up the light into its constituent spectral colors, which were then represented on a wavelength spectrum. In modern spectroscopy, the prism has been replaced by gratings, with high groove densities, which allows to separate

more precisely the incoming light. A movable slit and a photon detector complete the spectrometer apparatus and the entire system is controlled by a personal computer. Lenses and optical fibers can be used to collect and transmit the emitted light.

The absolute density, n_m , of a chemical specie in a given excited electronic level m can be determined by measuring its emission intensity, ϵ_{mn} , from the level m to a lower level n . The parameters which have to be known are the emission line wavelength, λ_{mn} , and the atomic transition probability, A_{mn} , from the level m to the lower level n as it is shown in equation (1-1).

$$\epsilon_{mn} = \left(\frac{hc}{4\pi\lambda_{mn}} A_{mn} n_m \right) \quad (1-1)$$

If the plasma is in a state of local thermal equilibrium, the electron temperature, T_e , can be calculated using the Boltzmann equation (1-2) [48]. However, for non-thermal plasmas, provided the distribution of the excited level populations obeys a Boltzmann distribution, its slope is associated to the excitation temperature of the plasma species, T_{exc} , which gives an estimate of T_e .

$$n_m = n_T \frac{g_m}{U(T_{exc})} \exp\left(\frac{-E_m}{kT_{exc}}\right), \quad U(T_{exc}) = \sum g_m \exp\left(\frac{-E_m}{kT_{exc}}\right) \quad (1-2)$$

$$\ln\left(\frac{\epsilon_{mn}\lambda_{mn}}{A_{mn}g_m}\right) = \ln\left(n_T \frac{hc}{4\pi U(T_{exc})}\right) - \frac{E_m}{kT_{exc}} \quad (1-3)$$

In the Boltzmann equation (1-2), n_T is the total density of a particular plasma specie, g_m the statistical weight of the excited level m , and U , the partition function for the species investigated. h is the Planck constant, m_e the electron

mass, k the Boltzmann constant, and E_m , the energy of the level m . By rearranging equations (1-1) and (1-2) in terms of natural logarithm, equation (1-3) is obtained.

For a given T_{exc} , n_T and U are constant and thus, the first term on the right hand side of equation (1-3) is constant. By plotting $\ln(\epsilon_{mn}\lambda_{mn}/A_{mn}g_m)$ versus E_m for several excited levels m of a single specie, it is possible to determine T_{exc} from the slope of the plotted curve ($-1/kT_{exc}$).

For a preliminary study of the plasma gas composition, it is sufficient to know the relative density of the plasma species. To compare the relative density of various species in the plasma, the only requirement is to calibrate the light transmission of the optical system and the optical response of the photon detector using a continuous radiation source such as a tungsten lamp. In addition, if the emission lines have a Lorentzian line profile, their relative intensities can be compared by monitoring only their peak intensities, since the peak intensity is proportional to the total area under each line profile [49].

1.6. Laser-induced fluorescence spectroscopy

The OES can only measure chemical species in electronically excited states, states which are weakly populated in most laboratory plasmas. Therefore, another technique, such as the laser-induced fluorescence (LIF), is required to investigate atoms in the ground states or in metastable states. Well-documented descriptions of the LIF technique can be found in specialized books on laser spectroscopy such as the book of Clyne and McDermid [50]. This section describes the LIF history, theory and principles of operation, detection capability and use for the detection of the helium metastable state atoms.

1.6.1 History

LIF was initially developed by Marvin Minsky in 1957 as an enhancement approach in confocal imaging microscopy, in order to improve the visualization capability with biological specimens and materials (solid or liquid) with dimensions in the sub-mm to mm range [51]. In the 1970s, the LIF technique was first used to measure the relative populations of individual quantum states in the gaseous phase [52]. Since then, it has been used as an analytical method to measure very small concentrations of chemical species. For instance, LIF was used to measure trace amounts of formaldehyde (HCOH) [53] and hydroxyl (OH) radicals in the atmosphere [54]. Later on, LIF was used to study the kinetics of collision-free and elementary collision processes and to measure the lifetime and relaxation rate of chemical species [55].

It was only in 1975 that LIF technique was first used for plasma diagnostics. Stern and Johnson [56] used LIF for the determination of the ion velocity distribution in an argon plasma. Since then, LIF has been used for the detection of molecules and atoms in the ground and metastable states. For instance, Hu *et al.* [57] used LIF to detect ppm levels of nitric oxide (NO) in the ground state in a non-thermal pulsed corona reactor at pressures slightly above atmospheric pressure. A LIF-derivative technique, two-photon laser-induced fluorescence (TALIF), which will be described later, has been used to detect the absolute density of atomic oxygen (O) in the ground state [58] in a RF excited plasma jet operating in air. Several other species of importance in the context of the current project have been detected using LIF, namely hydrogen (H) (using TALIF) [59], the hydroxyl radical (OH) [60], nitrogen (N) [61], NO [62], and He [63].

1.6.2 Theory and principles

To observe the fluorescence from a sample, a laser light has to strike this sample and the laser radiation energy must be tuned to the absorption transition energy from the state investigated to a known upper electronic state. When the upper state de-excites to a lower energy state, the resulting photon emission is called “laser-induced fluorescence”.

The radiative power of fluorescence depends on the population density of the lower state, the transition probability between the excited and lower states, and the frequency of the fluorescence photon. As shown in equation (1-4), the absolute population of a specie in the excited state k is n_k and can be determined from the measurement of the fluorescence rate, n_{Fl} , (# of photons emitted per second from the reaction volume V_R) only if the total spontaneous emission coefficient, A_k , from the level k to all lower levels i is known. In reality, it is very rare that A_k is known, because the transitions from the k level to lower levels i are not all quantified and thus, n_k value is generally not determined.

$$n_{Fl} = n_k A_k V_R = n_i V_R \frac{B_{ik} \rho}{1 + B_{ik} \rho / A_{ki}} \quad (1-4)$$

n_{Fl} can also be measured to determine the population density in a particular electronic state, n_i (right hand side of equation (1-4)). In this case, the laser is tuned to one specific wavelength so that a photon is absorbed by the transition i (lower level) \rightarrow k (excited level) and the fluorescence rate from the level k is measured. In this case, the parameters that have to be known are ρ the spectral energy distribution, β_{ik} the induced-absorption coefficient for the transition from the levels $i \rightarrow k$ and A_{ki} the spontaneous emission from the level k to level i . Under stationary conditions, if one knows which phenomenon between the spontaneous emission (A_{ki}) or the induced-absorption (β_{ik}) dominates, the

fluorescence process in equation (1-4) can be simplified and the lower state population densities (n_i) can be calculated.

For a preliminary identification of the ground state and metastable species in the plasma, a relative intensity measurement is satisfactory and it is easily determined since it is proportional to the measured fluorescence rate.

Briefly, a modern LIF system is composed of three main components. The first one is the laser system, which comprises a narrow line width pump laser and a tunable laser (dye, optical parametric oscillator (OPO), optical parametric oscillator (OPG)) that disperses the laser wavelengths (i.e. 350 to 800 nm), from which any given wavelength can be selected. Optionally, a UV-enhancement optical system can be added to extend the laser emission to the UV region (i.e. 200 to 350 nm). The second component is the optical system that allows the beam transport, focusing and collection. The last component consists of a photon detector (i.e. multiplier tube (PMT) or charge-coupled device (CCD)).

1.6.3 Detection capability

Most of the metallic atoms and light molecules can be detected by LIF. However, several light atoms and molecules have their first electronic excited state in the VUV range ($\lambda < 190$ nm), which corresponds to energies higher than 6.5 eV. In order to produce laser photons with sufficient energy to induce such transitions, a technique called two-photon absorption laser-induced fluorescence (TALIF) can be used. This technique consists of using a UV generator system or an optical set-up to produce a laser beam whereby two photons are absorbed simultaneously. This technique is valid as long as the two photons are absorbed in a time-scale smaller than the spontaneous de-excitation time of the laser-populated state.

LIF can detect species density as low as $\sim 10^4$ atoms/cm³ (typically of $\sim 10^6$ atoms/cm³), which sensitivity is comparable to the mass spectrometry sensitivity. In some reported cases, densities as low as $\sim 10^2$ atoms/cm³ [64] were detected by LIF. The spectral resolution of the LIF technique is mainly determined by the laser line width. A narrow laser spectral line width enables the selectivity of species. Also, strong laser beam intensity allows the detection of species having weak absorption cross-sections.

The LIF technique is non-intrusive and its spatial resolution is determined by the laser beam dimensions at the location of the measurement and the focusing of the detection system, which beam can be trimmed and focused to reach small dimensions (i.e. < 1 mm).

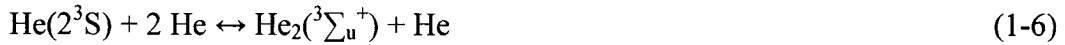
Therefore, LIF is a very sensitive non-intrusive technique, which permits the characterization of species in a specific quantum state with a very good spatial resolution. It is seen as a complement to OES, since it allows to probe the ground state density, the most populated one in weakly excited plasmas.

1.6.4 Detection of helium metastable states

Interesting species to investigate in the context of this research project are the metastable states of He. The first excited states of He are metastable states with high-energy levels of 19.4 eV for the 2^3S state and 20.4 eV for the 2^1S state, as shown in the He energy diagram (Figure 1-8). Radiative transitions from the He metastable states to the ground state are forbidden and thus, He metastable states lose their energy only through collisional processes.

In He plasmas, the collisions of metastable He states with other molecules generate new chemical species and free electrons, which help to sustain the plasma. According to Tsuchida [65], the dominant processes in a low electron

density ($<10^{13} \text{ cm}^{-3}$) He plasma are radiation processes and collisional transfers of electrons as depicted Figure 1-9. However, in a He plasma operating at elevated pressure (few atm), the amount of He(2^3S) atoms detected by LIF could be underestimated since some He(2^3S) atoms are used to produce He $_2(a^3\Sigma_u^+)$ molecules by processes described in equations (1-5) and (1-6) [66]).



As can be seen in Figure 1-9, a method to detect the He(2^3S) state is to pump this state with a laser tuned at 388.9 nm to the He(3^3P) state and to observe the fluorescence at the same wavelength. Many researchers have used this method in low-pressure plasma systems. To name a few, Tsuchida used LIF to measure the He(2^3S) density in the glow of a DC He plasma ($\sim 0.4 \text{ Pa}$, $n_e \sim 10^{12} \text{ cm}^{-3}$, $T_e \sim 7 \text{ eV}$ and plasma column radius $\sim 1 \text{ cm}$) [65]. Den Hartog *et al.* used LIF to measure the He(2^3S) density in the glow of a DC He plasma (467 Pa, $n_e \sim 10^{11} \text{ cm}^{-3}$, $T_e \sim 0.12 \text{ eV}$, electrodes diameter = 3.2 cm, electrode gap = 0.62 cm) [67]. De Benedictis *et al.* used LIF to detect the He(2^3S) density in a parallel-plates pulsed RF post-discharge of He-N $_2$ /O $_2$ plasma (6.6 – 400 Pa, $n_e \sim 10^{10} \text{ cm}^{-3}$, $T_e = 0.2\text{-}0.6 \text{ eV}$, electrode diameter = 10 cm, electrode gap = 5.5 cm) [63],[68].

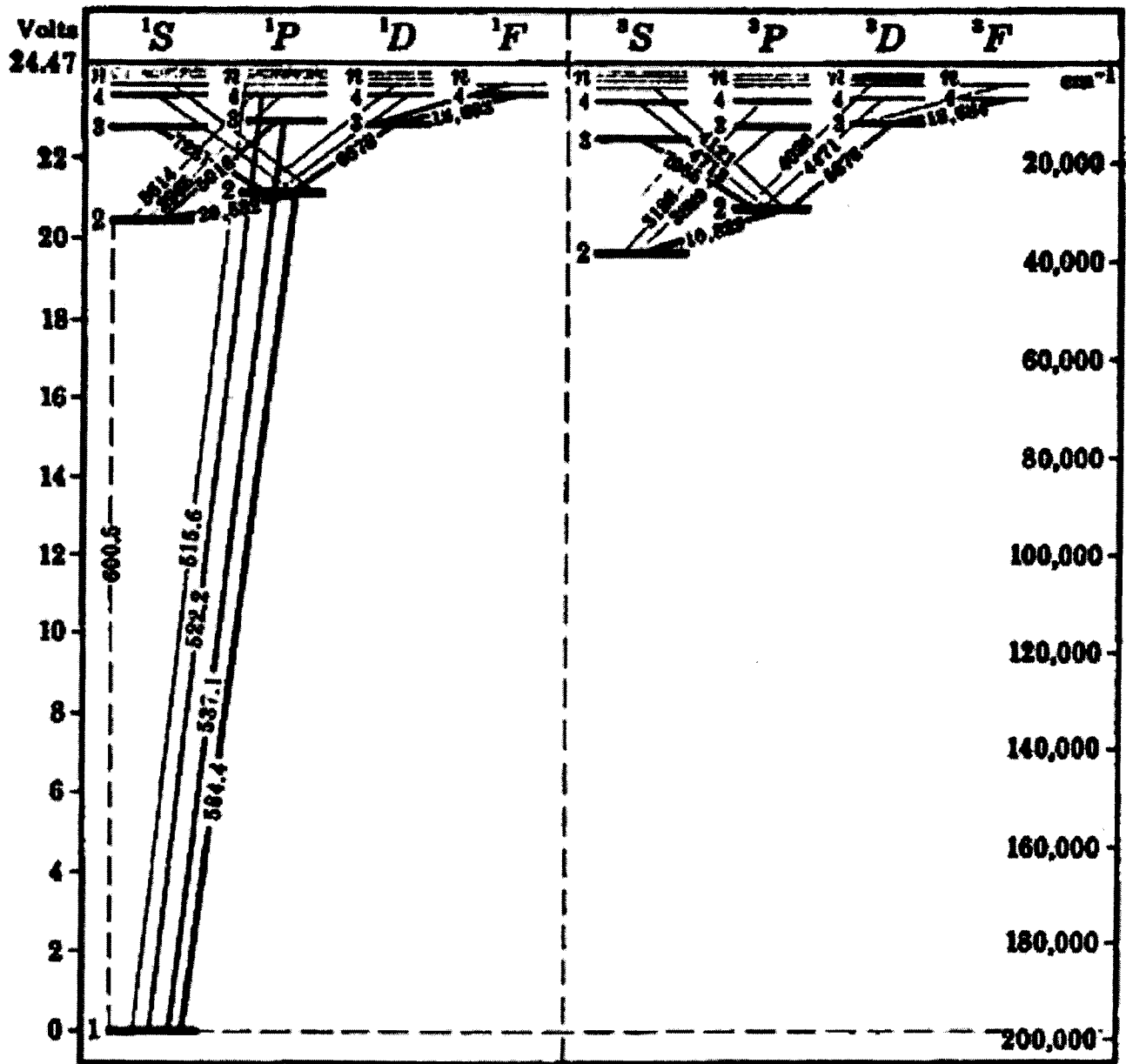


Figure 1-8: Energy level diagram for helium. The wavelength units are Angström [69].

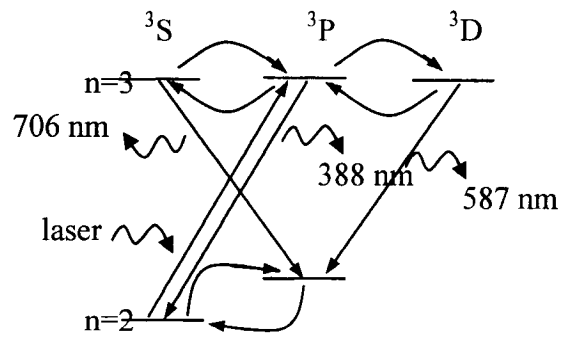


Figure 1-9: Dominant processes for LIF measurement of the He(2^3S) state in He plasmas.

Few researchers used LIF to measure the He(2^3S) in mm-scale He plasmas at atmospheric pressure. Boudam [70] used the LIF technique to measure the He(2^3S) state in a MW He and He/N₂ plasmas ($P = 706$ kPa, $n_e = 10^{14}$ cm⁻³, $T_e = n/a$, plasma length ≈ 3 cm, plasma diameter < 2 mm) operating in a controlled environment. According to our survey of the published literature, none have used the LIF technique to detect mm-scale He plasmas operating in air.

The He(2^3S) state can be detected using wavelengths other than 388.9 nm. For instance, one can pump the He(2^3S) state to the (4^3P) state using a laser at 318.8 nm and observe the fluorescence at the same wavelength. In addition, the metastable He state can be detected by considering the fluorescence from the (3^1P) state to the (2^1S) state, where the (3^1P) state de-excitation generates fluorescence at 501 nm. However, the (3^1P) state also de-excites to the (1^1S) state, generating fluorescence at 53.7 nm, a wavelength which cannot be observed under atmospheric pressure conditions. Moreover, some researchers [65,71] have found that the He(2^1S) state density is two orders of magnitude lower than the He(2^3S) state density. Therefore, choosing to observe the He(2^3S) state gives a better representation of the He metastable state density.

A derived technique of LIF, laser-collision-induced fluorescence (LCIF) [72], can be used to measure the relative density of the He(2^3S) state. For instance, using this technique, the (2^3S) state is pumped to the (3^3P) state by a laser at 388.9 nm. Then, the (3^3P) state de-excites by electron collisions to the (3^3S) state, and the resulting fluorescence from the (3^3S - 2^3P) transition is observed at 706.5 nm. The (3^3P) state is also excited to the (3^3D) state and from there, de-excites to the (2^3P) state and fluoresces at 587.56 nm. This technique has the advantage that the wavelength of the pumping laser differs from the fluorescence wavelength.

CHAPTER 2

DESIGN AND CHARACTERIZATION OF THE APGD-*t*

This chapter encloses an article written by Prof. Sylvain Coulombe and the Ph.D. candidate and published in the *Plasma Sources Science and Technology* journal [73] in August 2005. It describes the design rationale and the construction details of the APGD-*t*. This article also presents the preliminary electrical characterization and optical emission spectroscopy work done on the APGD-*t*.

As it will be seen in this article, the APGD-*t* does not fall in a unique category of APNTPs (see Table 1-1). It has a PV/Q (69 J/L) comparable to the one found in pulsed coronas and glow discharges; a P (15 W/cm³), which is similar to the one found in pulsed coronas, pulsed glows, RF discharges and DBD and a T_g (323 K) comparable to the one found in pulsed coronas, glow discharges and DBD. Its V (85-172 m/s) is like that V found in plasma torches, pulsed glows and glow discharges and its d (0.822 mm) is lower than that of micro-hallow cathodes, RF discharges, and DBD. If the APGD-*t* was to be classified according to those characteristics, it would lie in a category regrouping mainly pulsed coronas, glow discharges and DBD. Therefore, it is proposed that the APGD-*t* belongs to a new category of pulsed RF glow discharge torch.

In APPs, the gas kinetic temperature can be assumed equal to the gas rotational temperature, which value can be determined by optical emission thermometry [74]. Unfortunately, the spectrometer used during this project had a very poor spectral resolution (1.3 nm), and could not be used to perform thermometry.

Nevertheless, Kim *et al.* [75] have demonstrated that gas temperature, measured by a thermocouple and by optical emission thermometry in the plasma afterglow of a cold RF APGD, were comparable for low plasma powers (<180 W). In our

case, powers dissipated in the APGD-*t* are very low (<1 W). Therefore, throughout this project, a thermocouple was used as a quick and cheap way to measure the gas kinetic temperature in the plasma jet. However, this temperature should be compared to temperatures obtained using optical emission thermometry and by other methods, such as liquid crystal temperature strips as Kieft *et al.* used in [76].

Design and Preliminary Characterization of a Miniature Pulsed RF APGD Torch with Downstream Injection of the Source of Reactive Species

V. Léveillé and S. Coulombe

Department of Chemical Engineering, McGill University,

Montréal (QC), Canada, H3A 2B2

2.1 Abstract

The design of a miniature low-power Atmospheric Pressure Glow Discharge torch (APGD-*t*) and the results of its preliminary electrical and spectroscopic characterization are presented. A capacitively-coupled pulsed RF (13.56 MHz) helium plasma jet is formed in a converging confinement tube and O₂ is injected downstream in the plasma afterglow region through a capillary electrode. With 1 slm He, the APGD-*t* produced a non-thermal plasma jet of 500 μm-diameter and ≈2.5 mm-long at power levels ranging from 1 to 5 W. At ≈1 W, the gas temperature and He excitation temperature near the nozzle exit were ≈50 °C and slightly below 2000 K, respectively. The breakdown voltage in 1 slm He is approximately 220 V_{pk-to-0}. Careful electrical probe measurements and circuit analysis revealed the strong effect of the voltage probe on the total load impedance. The injection of 10 sccm O₂ through the capillary electrode led to the transport of atomic O further downstream in the plasma jet and to a slight increase of the He excitation temperature, without significant effects on the electrical properties and jet length. Alternatively, the addition of an equivalent amount of O₂ (1 %v/v) to the plasma-forming gas affected the electrical properties slightly,

but led to a drastic contraction of the plasma jet. The atomic oxygen production and transport conditions provided by the APGD-*t* are promising for localized bio-applications such as the treatment of skin tissues and cells.

2.2 Introduction

The interest in atmospheric pressure non-thermal plasma sources specifically designed for the modification and treatment of biological and biocompatible surfaces has grown considerably over the last decade. Such sources offer convenient means for sterilization [22,77] surface functionalization [23], cell removal [29], and microcontact printing of proteins onto polymer substrates [24]. The development of such plasma sources is not without challenges though, especially when one envisions bio-applications. The most important difficulties one encounters are: 1) the difficulty to sustain a stable and uniform glow discharge over large surface areas in film deposition and surface functionalization; 2) the need to maintain a high degree of non-thermal equilibrium to minimize the thermal load to the substrates of interest, while maintaining a high degree of chemical reactivity and 3) the extremely rapid recombination of the reactive species in the plasma afterglow when a torch configuration is used.

Several devices have been developed to produce relatively small non-thermal plasma streams at atmospheric pressure. A miniature inductively-coupled plasma (ICP) torch using an argon/halogen mixture was recently developed for localized and high rate etching of silicon wafers [6]. Miniature capacitively-coupled plasma torches using mixtures of He and halogen gases, or oxygen, have also been developed for local etching of silicon [7] and etching of polyimide [8]. Other capacitively-coupled plasma torches have been developed for the treatment of heat sensitive materials [9] and as a source of active species for the depletion of

contaminants present in liquid hydrocarbons [10]. Single electrode configurations were also reported for silicon oxidation, synthesis of carbon nanostructures [12] and removal of photoresist [11]. There have been other miniature sources developed for remote analytical systems, such as the microwave plasma torch (MPT), used as an excitation source for atomic spectroscopy [14-16]. The commonalities amongst these sources are: 1) the high-frequency excitation (RF or microwave, except for [10]) which favors the formation of a non-thermal plasma at atmospheric pressure under low-voltage excitation conditions (few hundred volts); 2) the use of He or Ar as the main plasma-forming gas, 3) the use of minute amounts of an additional gas as the source of reactive species, and 4) the torch configuration which permits the rapid transport of excited species to the surface of interest in remote exposure applications.

In the field of local bio-applications, atmospheric pressure plasma sources have been scarcely reported since the early 1990's. The argon plasma coagulation (APC) device, which uses a small rod as the powered electrode and the patient as the ground electrode, was commercialized as a small-scale electrocoagulation tool [26]. It was demonstrated through clinical trials that the APC caused significantly less damage to tissues than YAG lasers. The APC produces an electrical discharge between the electrode and the lesion which desiccates, coagulates, and devitalizes through heat effects [27,28].

Stoffels and colleagues [29-31] developed an atmospheric pressure unipolar RF "plasma needle", operating at power levels ranging from 10-100 mW, for localized bio-applications. Tests performed on hamster ovarian cells and human cells of lung carcinoma showed that the plasma was temporarily altering the cell's adhesion molecules and membrane, without necrosis, leading to cell-detachment. The authors of the study proposed that the plasma-produced radicals and UV radiation are responsible for this detachment mechanism.

Both devices just described (i.e. the APC and the “plasma needle”) involve some degree of coupling of the plasma source with the surface, and were not designed to efficiently generate and transport reactive chemicals to the heat-sensitive surfaces. In fact, the torch configuration discussed previously would be more appropriate.

We thus present, in this study, the design and results of a preliminary electrical and spectroscopic characterization of a novel low-power atmospheric pressure glow discharge torch for local bio-applications.

2.3 The APGD-*t*

2.3.1 Design rationale

The applications envisioned for the new plasma source are the etching of skin cancer cells, the detachment of cells, the removal of skin pigmentation, and the deposition of temporary organic films. All the above-mentioned treatments are superficial in nature due to the expected low-penetration depth of the plasma (see ref. [27]), and because of the low diffusivity of reactive gases into the skin. The plasma stream formed by this new plasma source needs to be small for localized treatment. For instance, if aligned mammalian cells (~30 μm OD) were treated with a 500 μm -diameter plasma jet, roughly 15 cells would be affected.

Furthermore, the new source must be capable of producing reactive species from a variety of reactive gas mixtures in order to accommodate the requirements of each process. Ideally, the source could easily be mounted on a small robotic arm or even hand-held, and would operate at low power and voltage levels.

Those specific requirements defined constraints on the design of the plasma source, namely: i) The need to use a torch configuration with a concentric capillary electrode, in order to form a well-defined plasma jet, to separate the plasma-forming and reactive species production-zones, and to avoid (electrical) coupling between the plasma and substrate. ii) The need to maintain a stable plasma at low voltage, in a gas that contains high-energy metastable species, which allow for the generation of reactive species in the afterglow. iii) The need for rapid transport of the reactive species formed in the afterglow to the surface of interest, iv) The need to operate the device at low-power levels suitable for bio-applications (ex. skin treatment). All those design constraints led us to adopt the torch configuration presented on Figure 2-1a, and b shows a prototype of the APGD-*t* using He as the plasma-forming gas and discharging into ambient air.

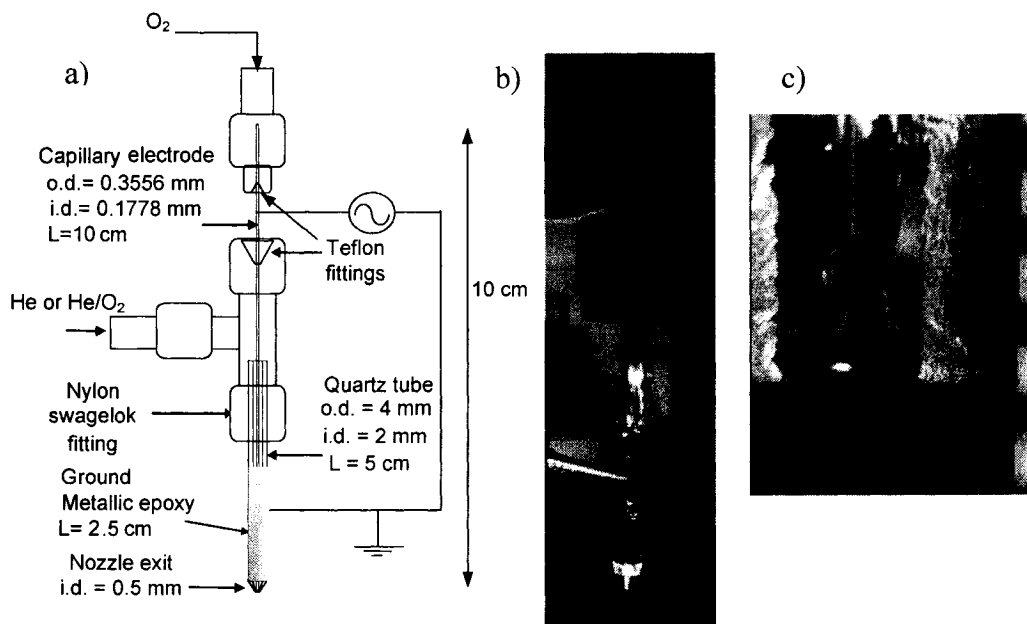


Figure 2-1: a) Schematic of the APGD-*t* construction. b) Picture of the APGD-*t* operating with 1 slm He at ≈ 1 W. c) Picture of the APGD-*t* nozzle area (the silver epoxy was removed to reveal the capillary electrode).

2.3.2 Details of the construction

From the electrical standpoint, the torch consists of a concentric electrode capacitor which uses as dielectric medium a quartz confinement tube (2 mm-ID x 4 mm-OD). The plasma-forming gas flows through the confinement tube at relatively high speed (1 slm He). Figure 2-1c shows the downstream end of the plasma confinement tube which is shaped into a converging nozzle (500 μm exit ID), in order to impart a high velocity to the plasma stream and to form the jet. An electrically-conductive silver paste deposited on the external surface of the confinement tube acts as the ground connection.

The powered electrode is a stainless steel capillary tube, centered inside the confinement tube. The inside and outside diameters of the capillary tube are 0.0070 ± 0.0005 " (0.1778 ± 0.0127 mm) and 0.0140 ± 0.0005 " (0.3556 ± 0.0127 mm), respectively. The end of the capillary tube is located approximately 1 mm upstream from the end of the quartz tube (this parameter can easily be changed). The gap formed between the external surface of the capillary electrode and the inner surface of the confinement tube is 822 μm -wide in the straight section, and reduces to 72 μm at the nozzle exit (assuming a perfect alignment of both tubes). The small outside diameter of the capillary electrode allows for the local enhancement of the electric field and thus, a considerable reduction of the breakdown voltage requirement. The entire assembly, which is roughly 10 cm-long, is held together with a Teflon Swagelok® tee.

The plasma-forming gas (He) is fed through the side arm of the tee, while reactive gases can be injected through the capillary electrode, or added to the plasma-forming gas. Under typical operating conditions in He, a glow discharge fills the entire annular space contained between the quartz tube and the capillary electrode. Helium allows operation at relatively low voltage under atmospheric pressure and

AC excitation conditions [78], and is known to provide excellent excitation conditions for emission spectroscopy [79]. Long-lived He metastable states provide excitation conditions in the decaying plasma: it is known that under low-frequency excitation (i.e. kHz), the He metastables provide seed electrons for re-ignition of the discharge every half-cycle. It is also believed that long-lived high-energy He metastable states (≈ 20 eV) can dissociate and ionize light molecules such as O_2 .

In a torch configuration with injection of the source of reactive species downstream of the plasma-forming region, the decaying He metastable atoms will thus act as an excitation source. Such a configuration was used by Jin *et al.* [14] where the analytes to be excited were injected downstream of the microwave plasma-forming region. Bilgic *et al.* [16] calculated the electric field at the nozzle of the microwave torch and, indeed, distinguished a plasma generation region from the excitation region for the analytes.

Molecular oxygen (O_2), which forms strong oxidizers once injected into a He plasma, is used as the source of reactive species in the present study (up to 10 sccm). O_2 -containing plasmas are known to provide efficient sterilization conditions [80-82] due to their etching capability and, therefore, are of interest for bio-applications. Atomic oxygen is produced by electron impact dissociation ($e^- + O_2 \rightarrow e^- + 2O$) and by dissociative attachment ($e^- + O_2 \rightarrow O + O^-$)[83]. It was suggested that the impact dissociation of O_2 by high energy (19.8 eV) He metastable atoms ($He(2^3S) + O_2 \rightarrow He + 2O$) is another possible mechanism for the production of O [45,78,84]. Unfortunately, no reference confirming this hypothesis is given (laser-induced fluorescence studies are currently underway in order to verify this hypothesis).

Lastly, an important flow rate of helium is used in an attempt to minimize the ratio of the gas convection to chemical reaction (recombination) time scales. This

favors the rapid transport of newly created radicals and excited species to the surface under treatment.

2.3.3 Flow conditions

In the absence of plasma and at a gas temperature of 25 °C, an annular flow of 1 slm of He between the capillary electrode and the nozzle exit gives rise to a mean gas velocity of 172 m/s, a value that corresponds to a Reynolds number (Re) of approximately 205 (laminar flow conditions)[85]. If one neglects the presence of the capillary electrode at the nozzle exit, a flow of 1 slm of He gives rise to a mean gas velocity of 85 m/s at the nozzle exit and a corresponding Re of 351. At 10 sccm in the capillary, O_2 is injected at a mean gas velocity of 7 m/s. The corresponding Re is approximately 75. Thus, laminar and subsonic flow conditions will prevail at the nozzle exit under cold flow conditions. The important velocity difference between the He and O_2 gas flow velocities will cause a significant shear at the injection point, thus favoring the mixing of the two gas streams.

2.3.4 Auxiliary equipments

A schematic of the APGD- t and associated electrical equipments are presented in Figure 2-2. The RF signal is generated using an arbitrary waveform generator (HP 33120A, 15 MHz bandwidth) set at a carrier waveform frequency, f , of 13.56 MHz, and which is amplitude-modulated (10-50% duty cycle) by a variable duty-cycle square wave generator (Racal-Dana model F64 AM-FM-sweep-trig/pulse-function generator). The amplitude modulation allows for easy control of the power level at constant torch voltage, and to switch off the plasma for a user-defined fraction of the cycle. The signal is amplified with a broadband RF

amplifier (Amplifier Research 75A250, 75W, 10 kHz-250 MHz, 50 Ω input/output impedances).

A homemade series inductor is used in order to provide near-resonance circuit conditions. The APGD-*t* is mounted on a 3-axes support, allowing the micrometric displacements necessary for localized optical measurements and surface treatments. The torch voltage and circuit current are measured using a voltage probe (Tektronix P6139A, 10X, 500 MHz, 10 M Ω , 8 pF), a current probe (Tektronix CT-2 current transmitter, 1mV/1mA into 50 Ω , with a Tektronix P6041 probe, 1X) and a digital oscilloscope (TDS3054B, BW = 100-500 MHz, 5 GS/s). The voltage and current measurements are transferred to a PC through a GPIB interface and displayed on a LabViewTM interface. A proportional, integral and derivative (PID) control loop is used in order to regulate the torch power and monitor the operating parameters.

Helium (99.998 % purity) or a certified mixture of He + 1 v/v% O₂ (± 5 %) is used as a plasma-forming gas. Extra dry oxygen (99.6 % purity) is injected through the capillary electrode as a source of reactive species. The gas flow rates are regulated using thermal mass flow controllers (Qualiflow, AFC 80 MD). The plasma jet temperature is measured using a 0.5 mm-OD, ungrounded and shielded type K thermocouple. Pictures and optical emission of the plasma jet were captured with a telemicroscope (Edmund Optics, 16X) and a low-resolution UV-VIS spectrometer (Ocean Optics USB2000). A bi-convex lens (50 mm-diameter, 15 cm focal length) was used to collect the plasma emission and to focus it onto a 400 μm optical fiber attached to the spectrometer. The optical response of the system was calibrated with a tungsten filament lamp (EPT-1373) over the 200-850 nm wavelength range.

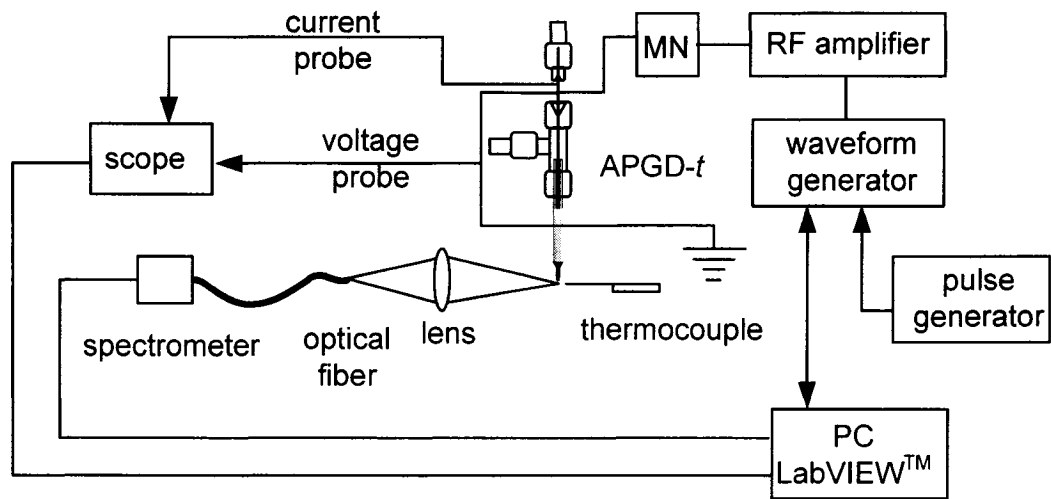


Figure 2-2: Schematic of the experimental set-up.

2.4 Results and discussion

This preliminary investigation of the APGD- t focused on determining the breakdown voltage and reasonable impedance matching conditions, measuring the torch's complex impedance, observing the effect of the duty cycle on the power level and jet temperature, observing the effect of O₂ injection on the plasma jet's structure, identifying species present in the jet, and estimating the excitation temperature. Unless specified otherwise, He (1 slm) was used as the plasma-forming gas while the duty cycle and pulsation rate of the RF excitation were 10 % and 100 Hz, respectively.

Typical torch voltage and circuit current signals are presented in Figure 2-3. The current signal reveals the complete extinction of the discharge following every pulse and the ease of re-ignition.

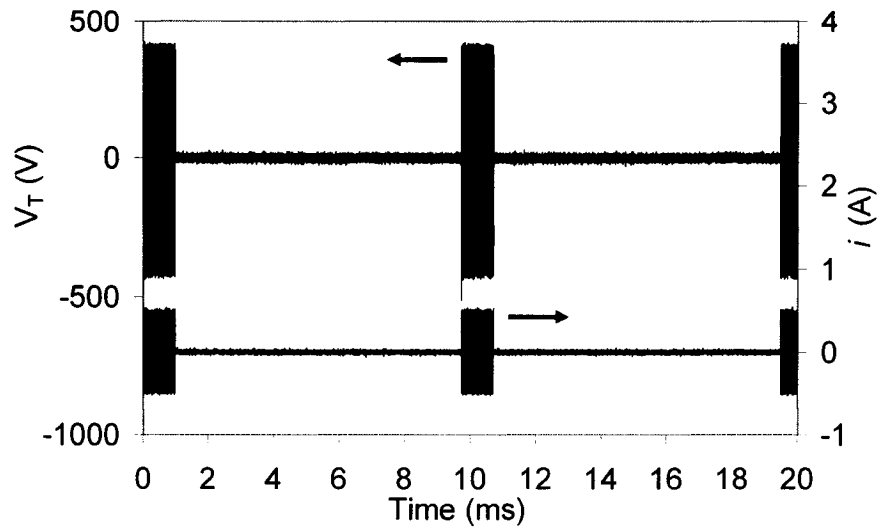


Figure 2-3: Representative example of the RF circuit current (i) and voltage pulses (V_T) applied to the APGD- t operating with 1 slm He and 10 % duty cycle.

2.4.1 Breakdown voltage

The breakdown voltage in He was measured by slowly increasing the voltage applied to the torch until the onset of light emission. At the breakdown voltage, the discharge ignites around the center capillary electrode where the electric field is most intense. The discharge spreads inside the volume available as the voltage is further increased. The breakdown voltage of the torch is approximately $220 V_{\text{pk-to-0}}$ ($\pm 2\%$). This low value is attributed to the geometrical amplification of the electric field at the capillary electrode surface. In fact, approximate calculations of the electric field at the breakdown voltage and of the geometrical amplification factor β at the surface of the capillary electrode (with respect to the planar geometry) gave values of $\approx 5 \times 10^5 \text{ V/m}$ and 4.4, respectively. Note that this breakdown electric field value compares well with the value of $\approx 2 \times 10^5 \text{ V/m}$

obtained by extrapolation of the Paschen's curve data reported for the high-frequency breakdown of He [86]. As a comparison, the reported sustaining (i.e. breakdown) voltage for the plasma needle spreads from $100 V_{pk-to-0}$ to $140 V_{pk-to-0}$ [30,31].

2.4.2 Impedance matching and plasma torch impedance measurement

Figure 2-4 shows a schematic of the electrical circuit considered for the impedance matching study. According to the usual model [87], the plasma torch is represented by a capacitor C_T mounted in series with a resistor $R_T [\Omega]$.

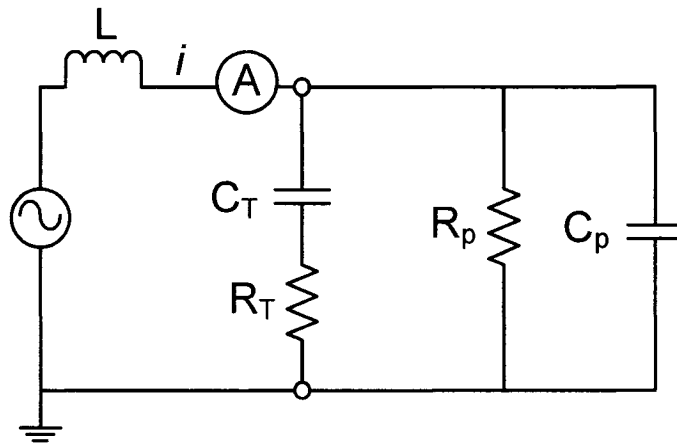


Figure 2-4: Schematic of the electrical circuit.

The complex impedance of the torch is thus described as ($s =$ Laplace domain variable):

$$Z_T(s = j\omega) = \frac{C_T s}{\tau_T s + 1} = R_T - \frac{j}{\omega C_T} \quad (2-1)$$

where $\tau_T = R_T C_T$ [s] is the torch's time constant and $\omega = 2\pi f$ [rad/s] is the carrier frequency in angular units. The complex impedance of the voltage probe is:

$$Z_p(s = j\omega) = \frac{R_p}{\tau_p s + 1} = \frac{R_p}{1 + \omega^2 \tau_p^2} - \frac{R_p \omega \tau_p}{1 + \omega^2 \tau_p^2} j \quad (2-2)$$

where $\tau_p = R_p C_p$ is the probe's time constant. At $f = 13.56$ MHz, the complex impedance of the voltage probe ($R_p = 10$ M Ω , $C_p = 8$ pF) is $Z_p = 0.215 - 1467j$ Ω . This small impedance value implies that the presence of the probe is likely to affect the dynamics of the electrical circuit and, thus, must be accounted for in the analysis. The complex impedance of the torch-voltage probe system is given by:

$$\begin{aligned} Z_{T+p}(s = j\omega) &= R_p \frac{(\tau_T s + 1)}{\tau_p \tau_T s^2 + \tau' s + 1} = \dots \\ \dots &= \frac{R_p}{(1 - \omega^2 \tau_p \tau_T)^2 + \omega^2 \tau'^2} \left[(1 - \omega^2 \tau_p \tau_T + \omega^2 \tau_T \tau') - \omega(\tau' - \tau_T + \omega^2 \tau_p \tau_T^2) j \right] \end{aligned} \quad (2-3)$$

with $\tau' = \tau_T + \tau_p + R_p C_T$. The phase shift, ϕ [$^\circ$], between the torch voltage, $V_T (= Z_{T+p} \cdot i)$ and circuit current, i , is given by:

$$\phi(\omega) = \frac{360^\circ}{2\pi} \cdot \tan^{-1} \left(-\frac{\omega(\tau' - \tau_T + \omega^2 \tau_p \tau_T^2)}{1 - \omega^2 \tau_p \tau_T + \omega^2 \tau_T \tau'} \right) \quad (2-4)$$

From the measurement of $|Z_{T+p}| = V_{T-RMS} / i_{RMS}$ and ϕ during the "ON" phase, the torch's resistance (R_T) and capacitance (C_T) values can be determined directly using equations (2-3) and (2-4).

A rudimentary homemade matching network consisting of a constant value inductor, L [H], mounted in series between the amplifier and the torch was used in order to achieve near-resonance conditions. No additional variable capacitors were used (in series or parallel) and thus, the circuit could not be fine-tuned. The

“cold” capacitance of the torch assembly (i.e. when the glow discharge is not yet ignited) was used in order to determine a suitable value for L . This capacitance was estimated by representing the torch assembly as a set of two concentric metal conductors of length l separated by a dielectric gap:

$$C_T^{Cold} = \frac{2\pi l \epsilon_0}{\left(\frac{\ln(r_2/r_1)}{\epsilon_{pr}} + \frac{\ln(r_3/r_2)}{\epsilon_{qr}} \right)} \approx 1.5 \text{ pF} \quad (2-5)$$

In the above equation, $l = 5$ cm, $\epsilon_{pr} = 1$ is the relative dielectric constant of air (or He), $\epsilon_{qr} = 3.75$ is the relative dielectric constant of quartz, $r_1 = 0.1778$ is the outside radius of the capillary electrode, while $r_2 = 1$ mm and $r_3 = 2$ mm are the inside and outside radii of the quartz tube, respectively. The circuit resonance is observed when:

$$L_o = \frac{R_p \tau}{1 + \omega^2 \tau^2} \quad (2-6)$$

with $\tau = R_p (C_T^{Cold} + C_p)$. At $f = 13.56$ MHz, one finds $L_o = 14.5$ μ H. On the other hand, the actual circuit was slightly de-tuned to accommodate the larger capacitance values expected when the glow discharge is present, and to account for the additional capacitive and inductive sources which were not considered in the analysis (ex. ground leads). It was found that an inductance value of 6.3 μ H (measured with a simple RL circuit ($f = 100$ kHz and $R = 3.3$ Ω)) led to easy ignition of the glow discharge and electrical stability of the plasma in the desired torch power range. The inductor was built from a coated copper wire wound onto a PVC tube using the following design equation [88]:

$$L = \frac{d^2 n^2}{45.7 d + 102 w} \quad (2-7)$$

In the above equation, d [89] is the outside diameter of the PVC tube, n is the number of turns, and w [89] is the length of coil wound on the tube. Equation (2-7) indicates that a $n = 8.5$ turns inductor built with $w = 1.3$ cm on a $d = 6$ cm tube has a theoretical inductance value of $6.4 \mu\text{H}$, which is close the measured value of $6.3 \mu\text{H}$.

Figure 2-5 shows one complete cycle of the 13.56 MHz excitation voltage applied to the torch and circuit current measured for conditions which are representative for all situations investigated in this study (with duty cycle $DC = 10\%$). The peak torch voltage and current are $405 \text{ V}_{\text{pk-to-0}}$ and $0.46 \text{ A}_{\text{pk-to-0}}$ respectively, while the phase shift between both signals is $-83^\circ (\pm 1.5 \%)$. The corresponding modulus of the impedance and power delivered to the torch-voltage probe system are $|Z_{T+p}| = 880 \Omega$ and $P_{T+p} = V_{T-RMS} \cdot i_{RMS} \cdot \cos \phi \cdot DC = 1.14 \text{ W}$, respectively.

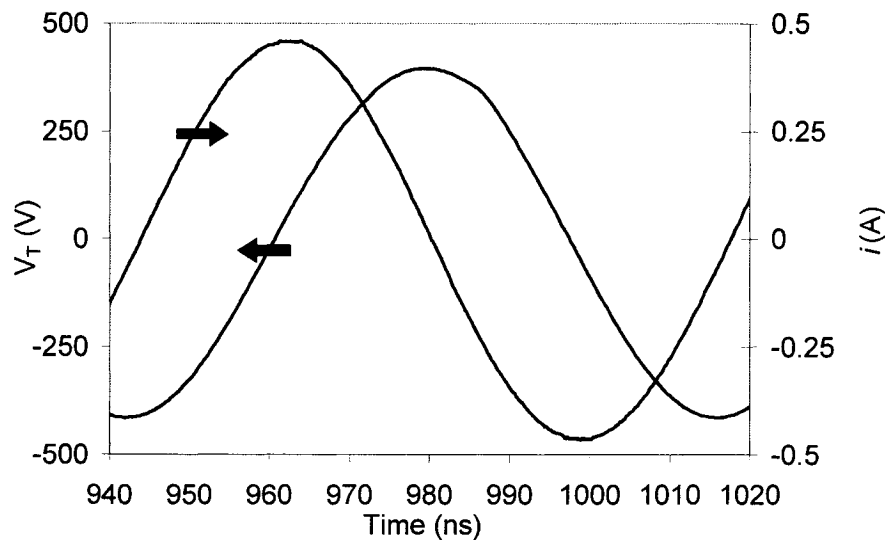


Figure 2-5: One cycle of the RF current (i) and voltage (V_T) signals applied to the APGD- t operating with 1 slm He.

Note the absence of current spikes which are associated with the formation of filamentary discharges, thus justifying the APGD appellation. Note also that the circuit current leads the torch voltage by a phase angle of -83° , revealing the highly-capacitive nature of the torch-voltage probe system. An abacus constructed using equations (2-3)-(2-4), with R_T and C_T as independent parameters, is used to determine the plasma torch impedance, Z_T , from those measurements. The continuous lines plotted on Figure 2-6 correspond to constant values of $|Z_{T+p}|$ while the dashed lines are associated with constant values of ϕ in the R_T - C_T plane. For $|Z_{T+p}| = 880 \Omega$ and $\phi = -83^\circ$, we find $R_T \approx 640 \Omega$ and $C_T \approx 5.8 \text{ pF}$ and consequently, the complex impedance of the APGD- t is $Z_T \approx 640 - 2024j \Omega$ (at $f = 13.56 \text{ MHz}$).

The resistive power dissipated in the torch is calculated using equation (2-8). At 10 % duty cycle, the resistive power dissipated in the torch was 1.14 W. Consequently, all the power supplied to the torch/voltage probe system is dissipated in the torch (since $R_T \ll R_p$). The power density under those conditions is 15 W/cm^3 (the volume occupied by the glow discharge is $\approx 76 \text{ mm}^3$).

$$P_T = \frac{V_{R_T-RMS}^2}{R_T} \cdot DC = \frac{\left(V_{T-RMS} \cdot \frac{R_T}{|Z_T|} \right)^2}{R_T} \cdot DC \quad (2-8)$$

Assuming that all the resistive power is used to heat up a substrate exposed to the plasma jet, one obtains a heat flux at the nozzle exit of $6 \times 10^6 \text{ W/m}^2$. In reality, this flux is expected to be significantly lower due to the radiative losses of the torch, and the spreading of the plasma jet over working distances of 1 to 2 mm.

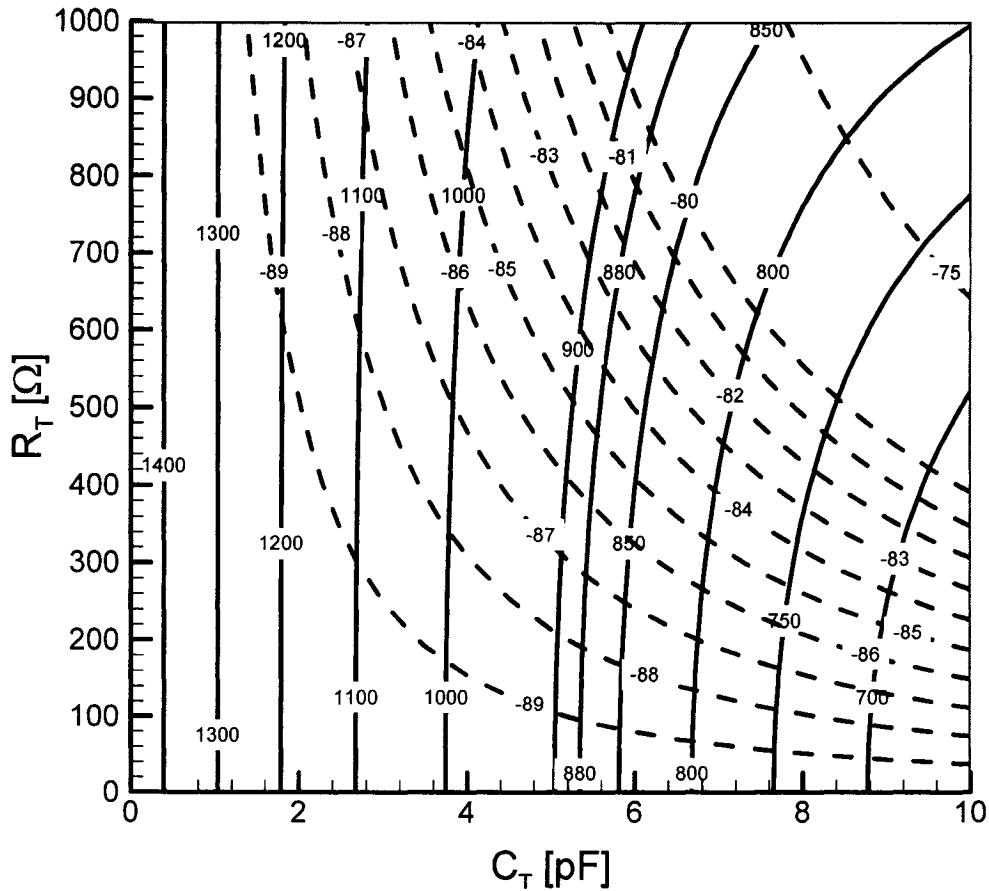


Figure 2-6: Contour plot of the modulus of the torch-passive voltage probe system complex impedance, $(|Z_{T+p}|)$, and phase shift (ϕ) versus the torch resistance (R_T) and capacitance (C_T).

2.4.3 Effect of duty cycle

Figure 2-7 presents the measured resistive power delivered to the torch, $P_T \approx P_{T+p}$, and the gas temperature measured by the thermocouple 1.5 mm downstream of the nozzle exit, as a function of the pulse duty cycle (DC). The results show that the torch power can be continuously modulated over the 1-5 W range by varying the duty cycle from 10 to 50%. Since both the torch voltage and circuit current

during the “ON” phase should not be affected by the duty cycle, one expects a linear increase of the resistive power with the duty cycle; this is indeed observed in Figure 2-7 (trend line slope of 0.1 W/% ($R^2=0.93$)).

Also plotted in Figure 2-7 is an approximate measurement of the maximum plasma exposure time to the skin (t_e). This time lapse was obtained by exposing a finger to the plasma jet, approximately at the same location as the thermocouple, until a burning sensation was felt. At 10% duty cycle, the gas temperature is 50 (± 2) °C, while this number increases to 122 (± 2) °C at 50%. It was found that a gas temperature of 50 °C is tolerable over a 10 second treatment time. As a comparison, the thermal neutrality zone for human skin spreads from 26 to 36 °C [24], and exposure to a heat source held at a temperature above 50 °C causes a burning sensation [90,91].

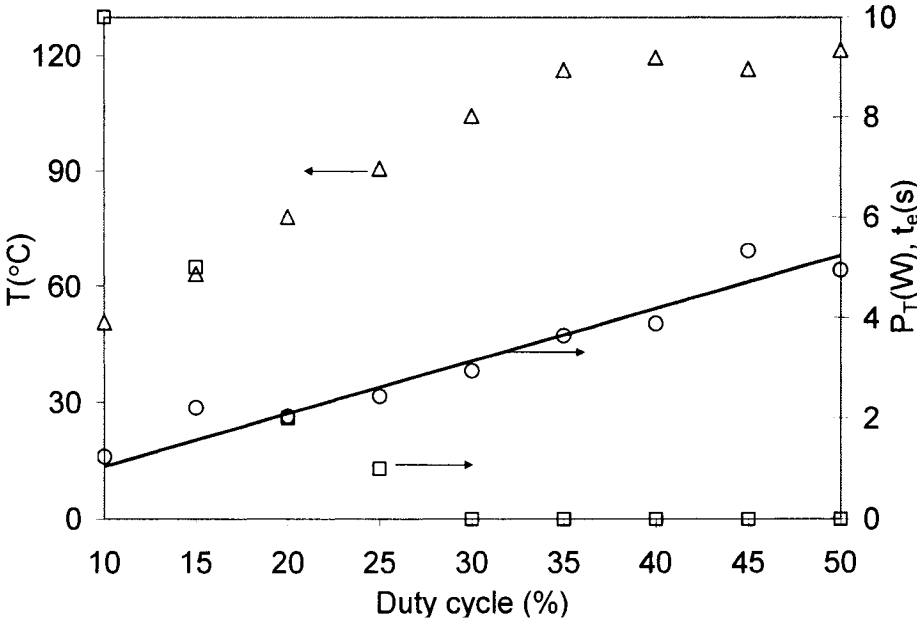


Figure 2-7: APGD- t power, P_T [W] (o), gas temperature, T [°C] (Δ), and exposure time to skin, t_e [s] (\square), versus the RF pulse duty cycle for 1 slm He.

2.4.4 Effect of O₂ addition

One important design aspect of the APGD-*t* is the downstream injection of the source of reactive species in an attempt to de-couple the plasma-forming region from the excitation region. The addition of 10 sccm O₂ through the capillary electrode did not disturb the torch voltage and circuit current characteristics. However, the addition of the same amount of O₂ to the He plasma-forming gas led to a 3% increase of the torch voltage and a 4% decrease of the circuit current (results not shown here). No appreciable effect to the shape of the electrical waveforms was observed. It is suspected that the addition of a trace amount of an electronegative gas to the inert plasma-forming gas causes a reduction of the electron density and consequently, a reduction of the electrical conductivity.

More dramatic changes were observed with the visual appearance of the plasma jet. Figure 2-8 shows telemicroscopic images of the ≈ 1 W plasma jet discharging in ambient air for three conditions: a) He (1 slm) as the plasma-forming gas, b) He (1 slm) as the plasma-forming gas with 10 sccm O₂ injected through the capillary electrode and c), He + 1 $\frac{1}{v}$ % O₂ (1 slm) as the plasma-forming gas. The top and middle figures reveal a whitish plasma cone, its color characteristic of He plasmas, followed by a bluish afterglow. It is interesting to notice a flow structure near the nozzle exit, suggesting a transition to supersonic conditions (Figure 2-8a-b). One can speculate that the additional acceleration of the flow is due to gas expansion caused by heating, and to some MHD pumping (these effects will be studied in a subsequent paper).

The injection of O₂ through the capillary electrode led to a slight elongation of the plasma cone, without significantly affecting the overall length of the jet. On the other hand, when a similar amount of O₂ was added to the plasma-forming gas, the jet length reduced to less than 1 mm. The plasma jet disappeared completely at a slightly higher O₂ flow rate.

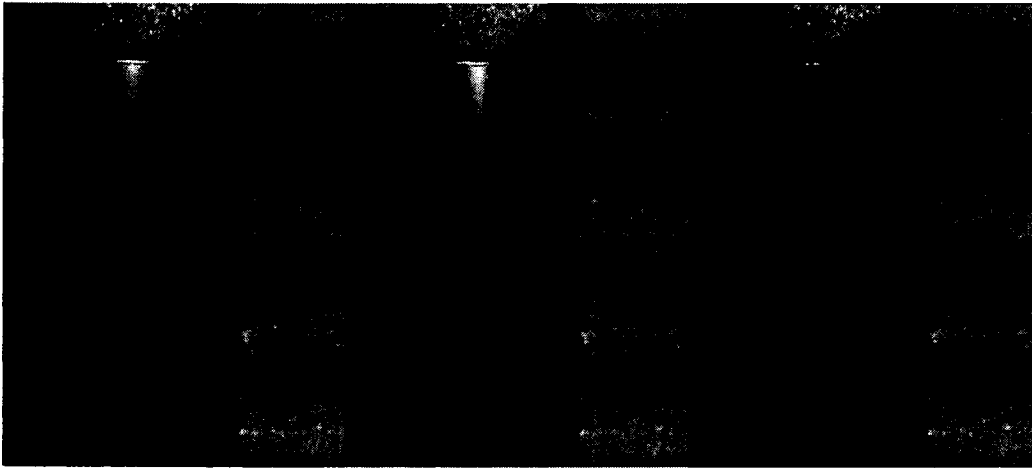


Figure 2-8: Telemicroscopic images of the plasma jet for $P_T \approx 1$ W. a) 1 slm He, b) 1 slm He with 10 sccm O_2 in the capillary electrode, and c) 1 slm He + 1 v/v% O_2 as plasma-forming gas.

Those observations were confirmed with the optical emission spectra taken 1 mm downstream of the nozzle exit (Figure 2-9). All emission spectra reveal the presence of excited He and atomic oxygen in the plasma jet, as well as some excited air molecules (entrained in the plasma jet). The addition of O_2 to the plasma-forming gas led to a significant decrease of the He emission (up to 90 % for 2^3P-3^3S transition of He at 706 nm) and air molecules emission, but without affecting the atomic oxygen emission (3^5S-3^5P at 777 nm). This suggests that a significant fraction of the plasma electrons are used to produce O-containing species from the O_2 molecules present in the plasma-forming gas (i.e. excited O_2 and O, and O-), leaving fewer electrons to collide and excite the He atoms and entrained air molecules.

The poor spectral resolution of the spectrometer does not permit differentiation of the spectral emission of N_2 (309, 316 and 391 nm) and N_2^+ (427 nm) from the Schumann-Runge O_2 system, OH band heads [92], and O_2^+ emission at 427 nm.

The probable formation paths of O_2^+ in a He plasma are direct electron-impact ionization ($e^- + O_2 \rightarrow 2e^- + O_2^+$) and Penning ionization ($He(2^1S) + He(2^3S) + O_2 \rightarrow He + O_2^+ + e^-$ [93,94]).

Since N_2 represents 79 % of air, its emission is likely to be significant with respect to O_2 and OH emission. The presence of N_2 lines (337, 357, 375, 380 and 405 nm) and N_2^+ lines (353, 391, 427 and 470 nm) in Figure 2-9 a-b clearly reveals air entrainment. Those N_2 and N_2^+ lines were reported by other researchers [10,79],[95]. Massines and Gouda [79] mentioned that N_2 molecules are very effective at quenching the He metastables resulting in the excitation of N_2 , and subsequent spectral emission. For instance, the N_2^+ emission at 391 nm is attributed to Penning ionization of N_2 with He metastables [96]. Thus, the emission lines at 391 nm and 337 nm, present up to 6 mm downstream of the nozzle exit, seen in Figure 2-10a, indicate the presence of He metastables in the plasma afterglow.

Atomic oxygen emission resulting from the 3^5S-3^5P transition at 777 nm was observed on all spectra, including the spectrum of Figure 2-9a, where no oxygen was voluntarily added, thus confirming the entrainment of ambient air in the plasma jet.

In Figure 2-10b, each O emission profile showed a maximum at the nozzle exit, and a monotonic decrease with the distance from the nozzle. In the case of O_2 injection in the capillary electrode, the O profile stretched further downstream of the nozzle exit. This is attributed to the higher density of O_2 introduced in the excitation region, and the slightly higher jet momentum (due to the O_2 flow).

The monotonic decrease of the excited O emission, and the peak in the excited N_2 species emission intensities, located downstream of the nozzle exit, are indicators of the decay of the electron and metastable He atom densities. Finally, it is

suspected that the density of ground state oxygen atoms is significant in the plasma afterglow since the 777 nm transition originates from a high energy level (9.146 eV).

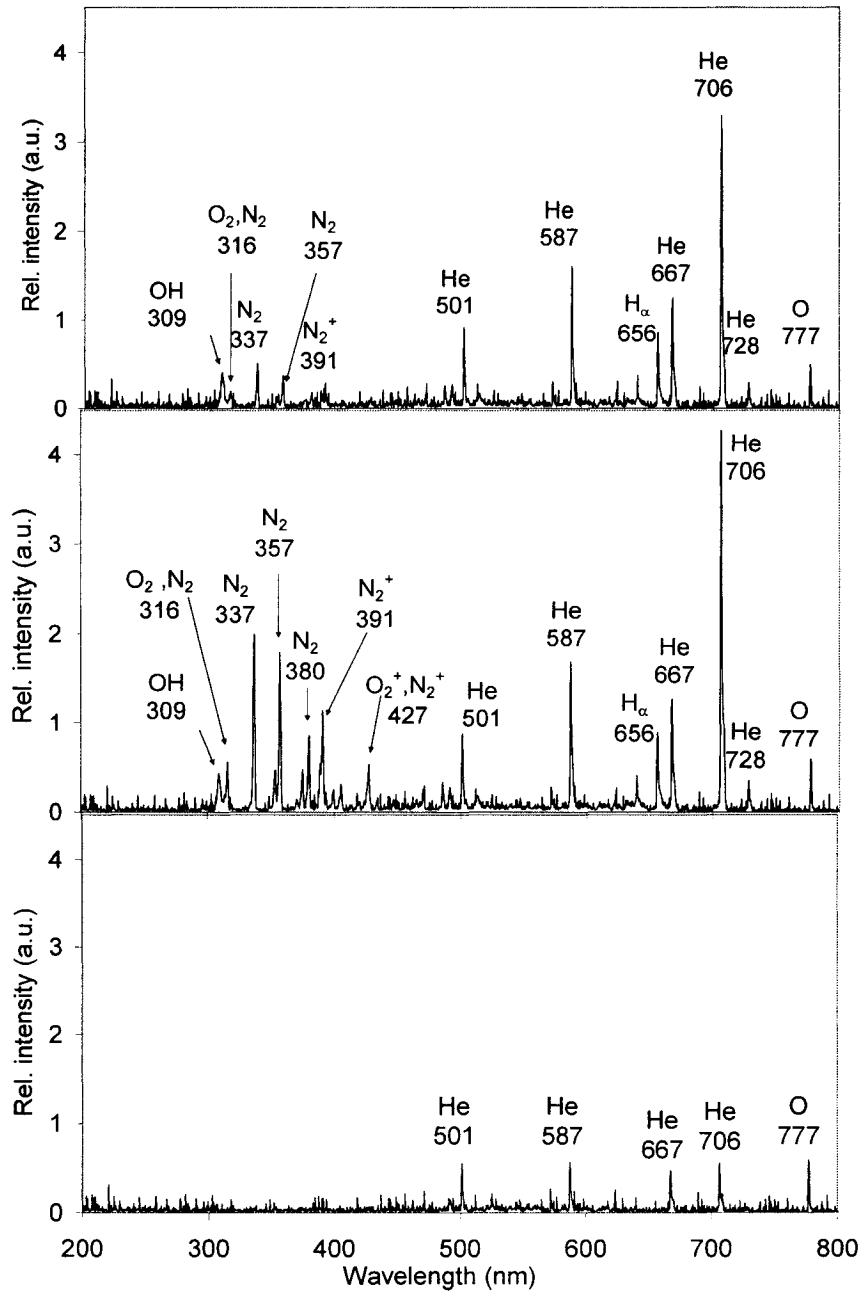


Figure 2-9: Emission spectra of the plasma jet ~1 mm downstream of the nozzle exit plane for $P_T \approx 1$ W. a) 1 slm He, b) 1 slm He with 10 sccm O₂ in the capillary electrode, and c) 1 slm He + 1 v/v% O₂ as plasma-forming gas.

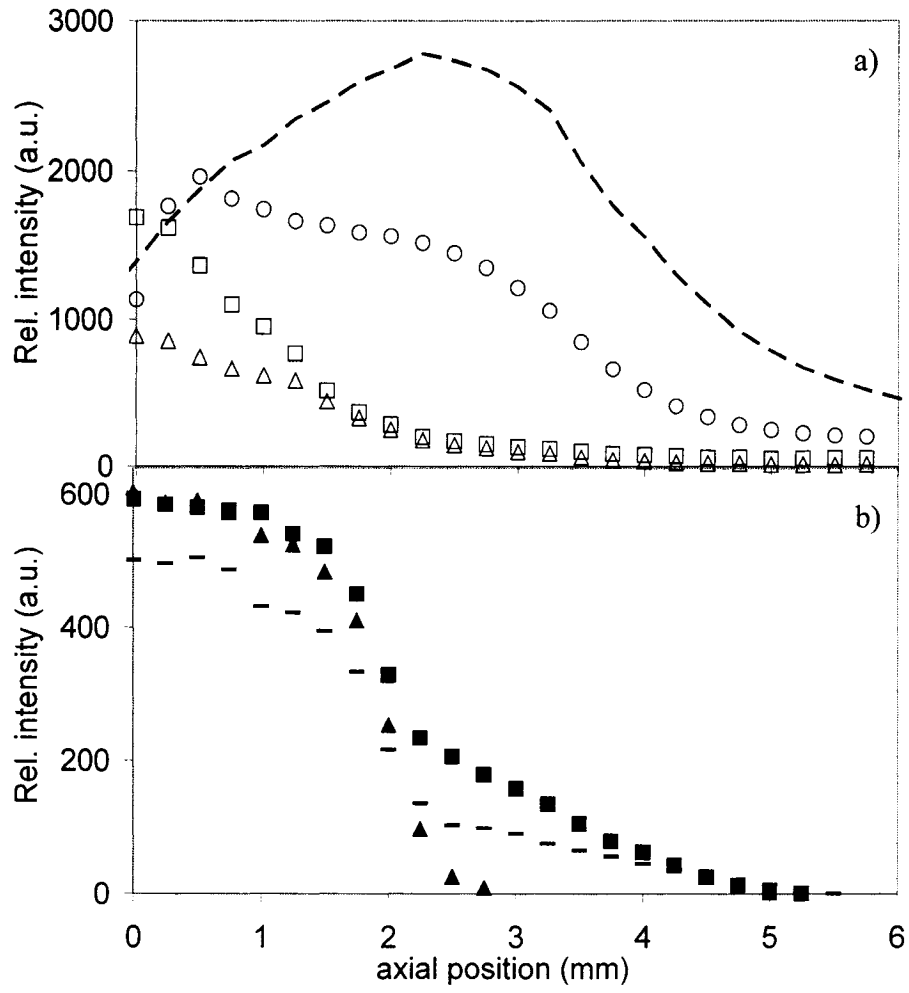


Figure 2-10: Axial profiles of the peak intensity of selected emission lines for $P_T \approx 1$ W.
 a) 1 slm He with 10 sccm O_2 in the capillary electrode: N_2 (---) at 337 nm, N_2^+ (o) at 391 nm, He (\square) at 587 nm and H_α (Δ) at 656 nm. b) O emission at 777 nm for 1 slm He (-), 1 slm He with 10 sccm O_2 in the capillary electrode (\blacksquare), and 1 slm He + 1 v/v% O_2 as plasma-forming gas (\blacktriangle).

2.4.5 Other species

Other He neutral lines can be identified on Figure 2-9 ($3^1\text{P}-2^1\text{S}$ at 501 nm; $2^3\text{P}-3^3\text{D}$ at 587 nm; $2^1\text{P}-3^1\text{D}$ at 667 nm and $2^1\text{P}-3^1\text{S}$ at 728 nm). The strong emission line observed at 656 nm corresponds to the H_α line since water vapor molecules from the ambient air can be entrained and dissociated in the plasma jet [69]. In fact, emission from the OH molecule at 309 nm was only observed when the 656 nm line was present. OH radicals can be formed by the reaction of excited O with water vapor ($\text{H}_2\text{O} + \text{O}^* \rightarrow 2\text{OH}$) and by electronic impact dissociation ($\text{H}_2\text{O} + \text{e}^- \rightarrow \text{H} + \text{OH} + \text{e}^-$).

2.4.6 He excitation temperature

The line-of-sight excitation temperature of the He atoms, $T_{exc}(\text{He})$, was determined by the Boltzmann plot method to get a feel for the excitation conditions prevailing in the plasma afterglow near the nozzle exit plane. It was assumed that the peak intensity of each line was proportional to its total integrated intensity [48], and that each line was optically thin. The neutral He atomic emission lines used to construct the Boltzmann plot were the 501 nm, 587 nm, 667 nm, 706 nm and 728 nm. Figure 2-11 shows the Boltzmann plot obtained with 1 slm He at $P_T \approx 1$ W, where $T_{exc}(\text{He})$ was 1573 K. For all conditions investigated, $T_{exc}(\text{He})$ was of the order of 2000 K or less.

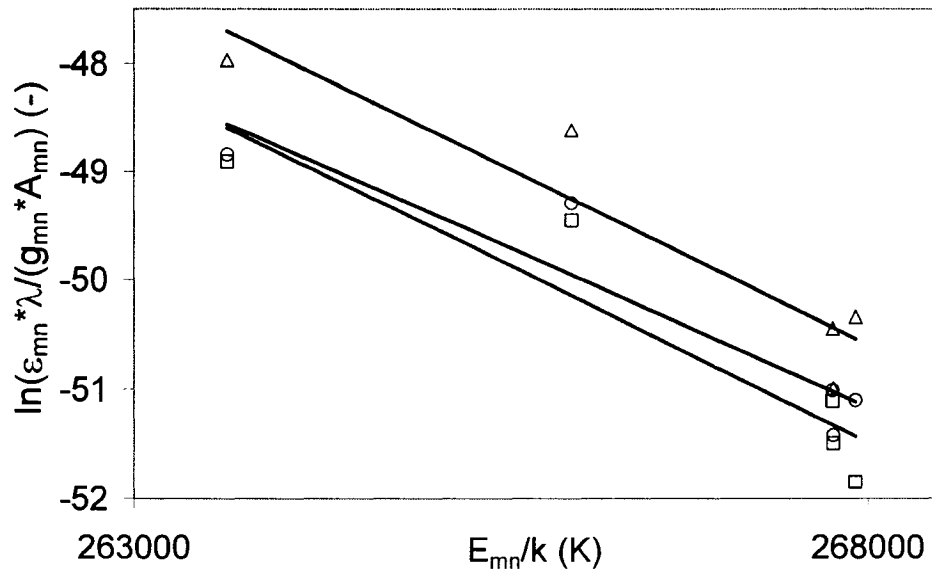


Figure 2-11: Boltzmann plot obtained for $P_T \approx 1$ W, 1 slm He and three different distances from the nozzle exit: -0.25 mm (\square), 0 mm (Δ) and 0.25 mm (\circ). The average excitation temperature is 1573K ($R^2=0.88$).

$T_{exc}(\text{He})$ showed a strong dependency on torch power and increased slightly with the injection of O_2 both in the capillary electrode and with the plasma-forming gas, as seen in Table 2-1. The presence in the plasma of O_2 , a source of electronegative species, causes an increase of the sustaining voltage and consequently, of the electric field strength. Therefore, the mean electron kinetic energy is increased, and this leads to an increase of the excitation temperature. Low excitation temperatures were also reported with other low-power atmospheric pressure plasma sources. A $T_{exc}(\text{He})$ of ≈ 1900 K was reported for a capacitive-coupled plasma discharge operating at 5 W with 475 sccm He [97], ≈ 2900 K with a single needle RF discharge operating with 1 slm He at 8 W [12] and ≈ 3000 K for the plasma needle operating at a few hundred mW [30].

Table 2-1: He excitation temperature (T_{exc}) for different plasma gas compositions and torch power levels.

Exp #	1	2	3	4	5
Plasma gas Composition	He	He + 1%v/vO ₂	He + 1%v/vO ₂	He + 10 sccm O ₂ capillary	He +10 sccm O ₂ capillary
P _T (W)	≈1	≈1	≈1.25	≈0.6	≈1
T _{exc} (K)	1573	1658	1739	1653	1914

2.5 Conclusions

In this study, the design of an atmospheric pressure glow discharge torch (APGD-*t*), and the results of a preliminary electrical and spectroscopic characterization were presented. The APGD-*t* produced a non-thermal plasma jet of 500 μm-diameter and ≈2.5 mm-length at power levels ranging from 1 to 5 W.

A methodology for the determination of the electrical figures of the APGD-*t* (i.e. complex impedance, resistance, capacitance, and resistive power) from careful electrical probe measurements was developed. The use of pulsed RF excitations at low duty cycle (10%) allowed the operation of the APGD-*t* at a ≈1 W power level. Under these conditions, the gas temperature was ≈50 °C, while the He excitation temperature was less than 2000 K.

The addition of 1 %v/v O₂ to the plasma-forming gas led to a drastic contraction of the jet. Alternatively, the injection of 10 sccm O₂ through the capillary electrode

led to the production and transport of atomic O further downstream in the plasma jet, without significantly affecting the electrical properties and jet length.

The capability to produce and transport reactive species under non-thermal plasma conditions is of potential interest for bio-applications where localized chemical treatments of heat-sensitive materials are involved. The near-future research activities will focus on the detection of metastable He and ground state oxygen atoms using laser-induced fluorescence to better understand the reaction processes. The plasma jet hydrodynamics is currently under investigation.

2.6 Acknowledgments

The authors wish to thank L. Cusmich, F. Caporuscio, and A. Gagnon for their technical assistance. The project was funded by the Natural Sciences and Engineering Research Council of Canada (NSERC), through the Discovery and Canada Research Chairs programs, the Fonds québécois de la recherche sur la nature et les technologies (FQRNT), and McGill University.

2.7 References

See the global bibliography at the end of the thesis document.

CHAPTER 3

DETAILED ASSESSMENT OF THE APGD-*t* ELECTRICAL CHARACTERISTICS

This chapter consists of an article accepted for publication in the *Measurement Science and Technology* journal on September 2006. It presents a meticulous electrical characterization study that was conducted, in order to assess the impact of commercial passive voltage probes on the response of the APGD-*t* electrical circuit and to calculate, with a relatively good accuracy, the resistive power dissipated in the APGD-*t*.

First, an introduction describes various techniques used for the electrical characterization of plasma sources and a comparison is made of their advantages and disadvantages. Second, a method to calibrate the phase angle measured between the torch voltage and the circuit current is presented. This method is based on a simple circuit model supported by experiments with similar parameters. The following section describes how the calibrated phase angle is used to calculate the resistive power dissipated in the APGD-*t* for typical operating conditions. Finally, a conclusion and recommendations are presented to comment mainly on the uncertainty associated with the use of this electrical characterization method.

Electrical probe calibration and power calculation for a miniature 13.56 MHz plasma source

V. Léveillé and S. Coulombe

Department of Chemical Engineering, McGill University,

Montréal (QC), Canada, H3A 2B2

3.1 Abstract

The article highlights and provides solutions to the difficulties encountered with electrical probe measurements performed on a miniature, high capacitive impedance plasma device excited at 13.56 MHz. It is shown that a proper calibration of the phase angle between the circuit current and load voltage signals is required when commercial capacitive voltage probes (Tektronix P6139A and P5100 models) are used. A method to calculate the electrical characteristics of the plasma source and accounting for this calibration is described. The P6139A probe, which has the largest input capacitance and shortest cable length, introduced the smallest phase angle ($-2 \pm 1^\circ$), while the P5100 probe, which is used for higher input voltages and has a longer cable length, introduced a considerably larger phase angle ($-34 \pm 1^\circ$) for typical resistive loads. Simple circuit models are developed in an attempt to isolate the phase induced by the probe capacitance and cable length. The application of the proposed calibration to a miniature atmospheric pressure glow discharge source considerably reduced the error on the calculation of the power dissipated in the plasma device, though it remained relatively high ($1 \text{ W} \pm 42\%$) due to the highly-capacitive nature of the device.

3.2 Introduction

Electrical measurements are essential to characterize plasma sources. Nowadays, a variety of instruments are commercially available ranging from voltage, current and Langmuir probes [35,36] to integrated monitoring devices such as impedance monitors [37], power meters ([38], [39], [40] and [41]) and network analyzers. Electrical measurements are invasive by their very nature and special precautions are taken to minimize the effects on the measurements and/or to account for these effects. This task is particularly challenging with today's miniature plasma sources, which represent, most often, high-capacitive loads due to the small inter-electrode gaps used, the high excitation frequency (MHz to GHz) and the comparatively small resistive impedance.

Some of the most useful measured electrical plasma properties are the power delivered to the electrical circuit driving the plasma load and the power dissipated in the plasma. Common instruments used to evaluate those power levels are bi-directional power meters and electrical probes. Some examples of their applications to small-scale plasma sources follow. The power meters can be used for monitoring the reflected power during plasma etching providing a simple and very inexpensive tool for end-point detection [42]. Stonies *et al.* [15] used a power meter to match a small microwave plasma torch (MPT) to the generator's 50Ω impedance using microstrip circuits. Kieft *et al.* [31] used a power meter to optimize the matching network of the Plasma Needle excited at 13.56 MHz. Another power meter, the Z-scan® RF probe [43], was used by Zhu *et al.* [44] to characterize an atmospheric pressure plasma jet (APPJ) excited at 13.56 MHz. Though very useful, power meters have some drawbacks. They tend to be expensive, they generally have a narrow measurement operating range and frequency bandwidth, and they are not designed to measure low level and/or pulsed powers. Moreover, only the high-end power meters can display signal

waveforms, which are good indicators of signal distortion, saturation and arcing phenomena.

The use of current and voltage probes in combination with a fast digital oscilloscope appears to be an easy to set up and inexpensive method to electrically characterize miniature plasma sources ([9], [45] and [46]). Such probes are used to quantify breakdown, sustaining and operating voltages, circuit current and the relative phase angles between the circuit current and the load voltage signals. They have wide measurement ranges and bandwidths, but they too have some drawbacks. One of their major downsides is their capacitive loading. Indeed, when a voltage probe is connected to a circuit, it adds a reactive impedance to it, which induces an additional phase angle between the circuit current and the load voltage. The probe resistive loading can also reduce the probed signal amplitude depending on the frequency at which the circuit is excited.

A second negative effect of voltage probes is the systematic time delay Δt induced by the length of the probe cable. This latter delay, Δt , is constant in the time domain, but its equivalent phase angle $\Delta\theta$ between the circuit current and the voltage signals increases with the excitation frequency f as revealed by $\Delta\theta = (360^\circ)f\Delta t$. The consequence is a misreading of the phase angle induced only by the capacitive or inductive nature of the load and thus, a deterioration of the accuracy on the calculations relying on that measured phase angle. One of the standard procedures to calibrate the phase angle between signals measured by current and voltage probes is to take the difference in their nominal propagation time delays, as provided by the probe manufacturer, and subtract this value from the measured time delay and convert it into a phase angle. The accuracy of this method relies strongly on the uncertainty given by the probe manufacturer. A more reliable method to calibrate the phase angle was used by Sobolewski *et al.*[47]. Instead of taking the propagation time delay from the manufacturer, they

measured *in situ* the total time delay induced by the probe capacitance and cable length.

This article presents a technique to calibrate the phase angle between the load voltage and circuit current signals. The calibration technique is applied to a range of load resistances to test its applicability. A method is also presented for the calculation of the power dissipated in the miniature atmospheric pressure glow discharge torch (APGD-*t*) [73] using the calibrated phase angle. Recommendations to improve the accuracy on the calculation of the power dissipated in highly capacitive sources are presented.

3.3 Calibration of the phase angle

The phase angle that appears between the circuit current and voltage across a purely resistive load of resistance value ranging from 50 Ω to 1500 Ω is calibrated using two commercial passive voltage probes at an excitation frequency of 13.56 MHz. Six values of load resistance R [Ω] are considered: $51.4 \pm 0.1 \Omega$, $99.2 \pm 0.3 \Omega$, $202.3 \pm 0.7 \Omega$, $510.6 \pm 0.7 \Omega$, $897 \pm 0.9 \Omega$ and $1501 \pm 0.4 \Omega$. Those values are chosen because they reflect common values of the resistance estimated for a miniature plasma source [73]. A circuit model is developed to calculate the phase angle induced by the probe capacitance alone. Experiments are conducted to measure the phase angle between the circuit current and load voltage signals. Since the measured phase angle includes both the phase angle induced by the probe capacitance and the probe cable length, it is then possible to isolate the phase angle induced by the probe cable length itself.

3.3.1 Circuit model

A circuit model is developed to determine how the input resistance and capacitance of a passive voltage probe and the excitation frequency affect the phase angle between the circuit current and the voltage across different load resistors. The circuit model is also used to determine the phase angle induced by the probe cables.

The commercial passive voltage probe is represented by a resistance, R_p [Ω], mounted in parallel with a capacitance, C_p [F], as shown in the electrical circuit of Figure 3-1. Depending on the type of probe, the values of R_p and C_p can vary. Two commercially available voltage probes are chosen with their respective R_p and C_p : the Tektronix model P6139A (10X \pm 0.5%, $R_p = 10 \text{ M}\Omega \pm 0.5\%$, $C_p = 8 \pm 0.8 \text{ pF}$, cable length = 1.36 m, typical propagation delay = 5.5 ns, ground lead length = 0.15 m with a crocodile clip and BW = 500 MHz), and the high input voltage Tektronix model P5100 (100X \pm 1.75%, $R_p = 10 \text{ M}\Omega$, $C_p < 2.75 \text{ pF}$ typical, cable length = 3.1 m, typical propagation delay = 14.9 ns, ground lead length = 0.29 m with a crocodile clip and BW = DC to 250 MHz). In the model, C_p is set to 2.75 pF for the P5100 probe.

A Tektronix CT-2 transmitter and the Tektronix model P6041 current probe (1X \pm 0.3%, cable length = 1.07 m, typical propagation delay = 6.1 ns, BW = 1.2 kHz to 200 MHz) are used to measure the circuit current i [A]. To simplify the model, it is assumed that the ground lead of the voltage probe has a negligible inductance L_g [μH].

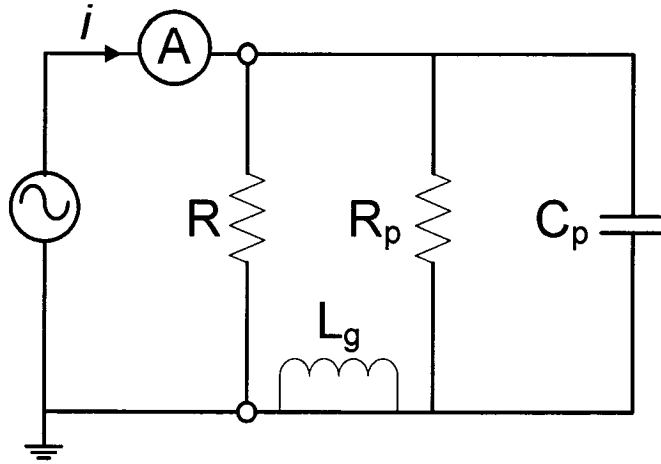


Figure 3-1: Schematic of the model electrical circuit.

The MATLAB[®] software and accompanying Simulink[®] toolbox [98] are used to analyze the response of the electrical model. The equations are written in the Laplace domain, programmed using a transfer function block diagram and the solution obtained and plotted in the time domain. The probe impedance, Z_p [Ω], and phase angle, θ_p , are given by equations 3-1 and 3-2, where the probe time constant τ_p [s] is $R_p C_p$. The equivalent impedance of the resistive load and voltage probe, Z_{R+p} [Ω], is given by equation 3-3. The voltage across the load is V_R [V] = $Z_{R+p}i$.

$$Z_p(s = j\omega = j2\pi f) = \frac{R_p}{\tau_p s + 1} \quad (3-1)$$

$$\theta_p = \frac{360^\circ}{2\pi} \tan^{-1} \left(\frac{\text{Im}(Z_p)}{\text{Re}(Z_p)} \right) = \frac{360^\circ}{2\pi} \tan^{-1}(-\tau_p \omega) \quad (3-2)$$

$$Z_{R+p}(s) = \frac{R'}{\tau' s + 1}, \text{ where } R' = \frac{RR_p}{R + R_p} \text{ and } \tau' = \frac{R\tau_p}{R + R_p} \quad (3-3)$$

$$\theta_{R+p} = \frac{360^\circ}{2\pi} \tan^{-1} \left(\frac{\text{Im}(Z_{R+p})}{\text{Re}(Z_{R+p})} \right) = \frac{360^\circ}{2\pi} \tan^{-1}(-\tau' \omega) \quad (3-4)$$

3.3.2 Experimental set-up

The electrical circuit is powered by a waveform generator (Hewlett-Packard 33120A, BW = 15 MHz, 50mV_{ppk}-10V_{ppk}, 50 Ω output impedance, max. power = 250 mW). The source voltage, V_s , was set to 5 V_{ppk} and the excitation frequency, f , to 13.56 MHz. The resistor R is connected to the circuit using a short dual binding post-to-BNC male adaptor to make sure no inductive or capacitive load is added to the circuit. The waveforms of the voltage measured across R and the circuit current i are displayed on a high-speed digital oscilloscope (Tektronix TDS3054B, 500 MHz, 4 channels, 50 Ω input impedance).

3.3.3 Results and analysis

The frequency responses of the model P5100 voltage probe as well and the equivalent impedance of a model 1000 Ω resistor + P5100 voltage probe are presented on figure 3-2. The value of θ_p decreases drastically to -90° with the increase of the excitation frequency. At 13.56 MHz, the $|Z_p|$ is reduced from its DC value of 10 MΩ to a value of 4268 Ω. However, the frequency response of the model 1000 Ω resistor load + P5100 voltage probe is less pronounced. The θ_{R+p} decreases monotonically with the excitation frequency and reaches a value of -13° at 13.56 MHz. $|Z_{R+p}|$ decreases to 973 Ω, confirming that the probe resistive loading is small at this frequency.

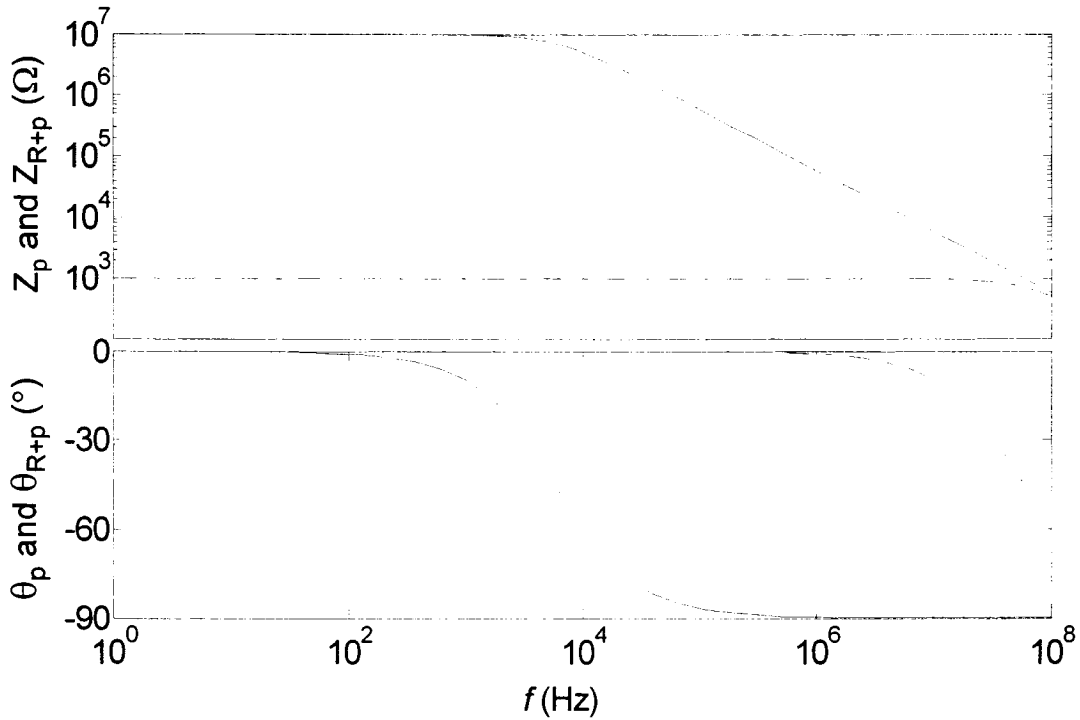


Figure 3-2: Frequency response of the impedance magnitude and phase angle for a voltage probe model with $R_p = 10 \text{ M}\Omega$ and $C_p = 2.75 \text{ pF}$: Z_p and θ_p (—) and for a resistor + voltage probe model with $R = 1000 \text{ }\Omega$: Z_{R+p} and θ_{R+p} (---).

The effect of the load resistance, R , and probe capacitance, C_p , on the phase angle between i and V_R is now evaluated for both commercial probes used ($R_p = 10 \text{ M}\Omega$ for both probes). Equation 3-4 indicates that predicted θ_{R+p} , which takes into account the probe capacitance but not the cable length, depends on R , R_p , C_p and f . In Figure 3-3, it can be seen that θ_{R+p} decreases monotonically with rising R . It is worth remembering that a purely resistive load has no complex impedance and thus, that it does not introduce a phase angle between i and V_R . The decrease of θ_{R+p} with the increase in R confirms the presence of probe loading as prescribed by an increase of the Z_R/Z_p ratio. Also, the slope of θ_{R+p} versus R for the P5100 probe ($C_p = 2.75 \text{ pF}$) is not as steep as for the P6139A probe ($C_p = 8 \text{ pF}$), which

effect demonstrates the dependency on C_p . For the P6139A probe, the measured and predicted phase angles agree for small load resistance values ($<100 \Omega$). On the other hand, a small discrepancy for larger R is observed.

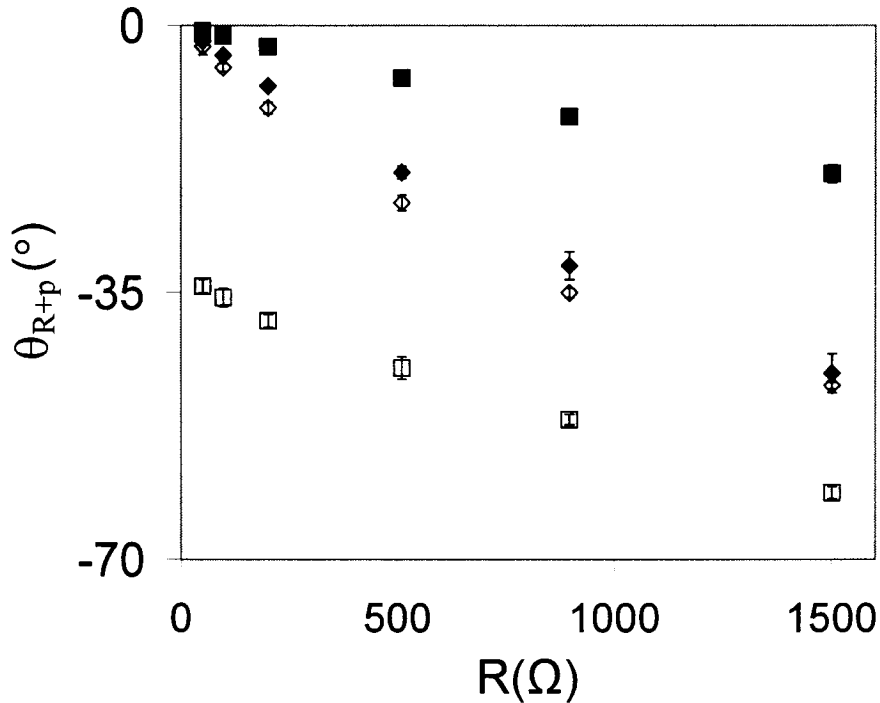


Figure 3-3: Phase angle between i and V_R for the P6139A (◆: model, ◇: measured) and the P5100 (■: model, □: measured) probes with respect to the load resistance at 13.56 MHz.

For the P5100 probe, this difference is much larger, even with a load resistance near 50Ω . This significant difference is associated with the difference in cable lengths of the voltage and current probes. This difference in cable length is 2.03 m for the P5100 probe, while it is only 0.29 m for the P6139A probe. The subtraction of the predicted θ_{R+p} from the measured θ^m_{R+p} gives the relative phase angle $\Delta\theta_{R+p}$ [°] introduced by the difference in cable lengths. Figure 3-4 shows that $\Delta\theta_{R+p}$ is relatively constant with respect to the load resistance for the P6139A

probe. In fact, considering the measurement uncertainties, it can be assumed constant over the range of load resistances considered and its value is equal to $-2 \pm 1^\circ$. This value agrees with the difference in propagation delays between the P6139A voltage (5.5 ns) and the P6041 current probes (6.1 ns), $\Delta t_{P6139A} - \Delta t_{P6041} = 0.6$ ns, with the corresponding difference in phase angles, $\Delta \theta_{P6139A} - \Delta \theta_{P6041} = (360^\circ)f(\Delta t_{P6139A} - \Delta t_{P6041}) = -2.9^\circ$.

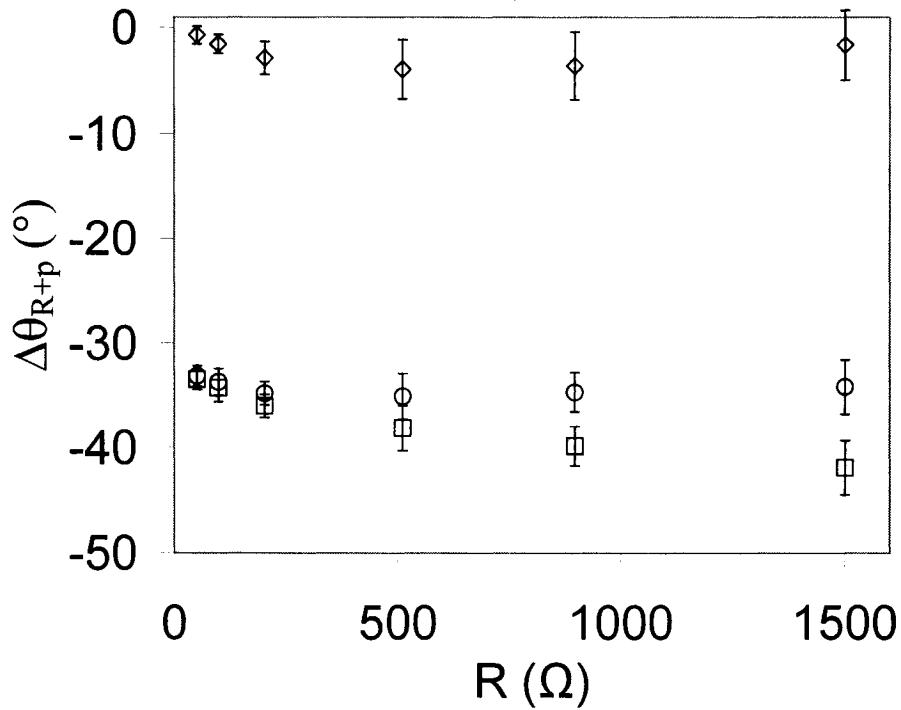


Figure 3-4: Relative phase angle $\Delta \theta_{R+p}$ introduced by the difference in cable lengths (current and voltage probes) for the (◇) P6139A probe and the P5100 probe with (□) $C_p = 2.75$ pF and (○) $C_p = 4$ pF at 13.56 MHz.

Regarding the $\Delta \theta_{R+p}$ behavior for the P5100 probe, one can see that the measurements do not fit the model prediction as well: we observe a decrease of the phase angle induced by the probe cables with the increase of R . This deviation

cannot be accounted for by the measurement uncertainty. This deviation might be due in part to the parasitic capacitances of the relatively long probe cable (3.1 m) or to the inaccurate value of C_p given by the probe manufacturer (< 2.75 pF).

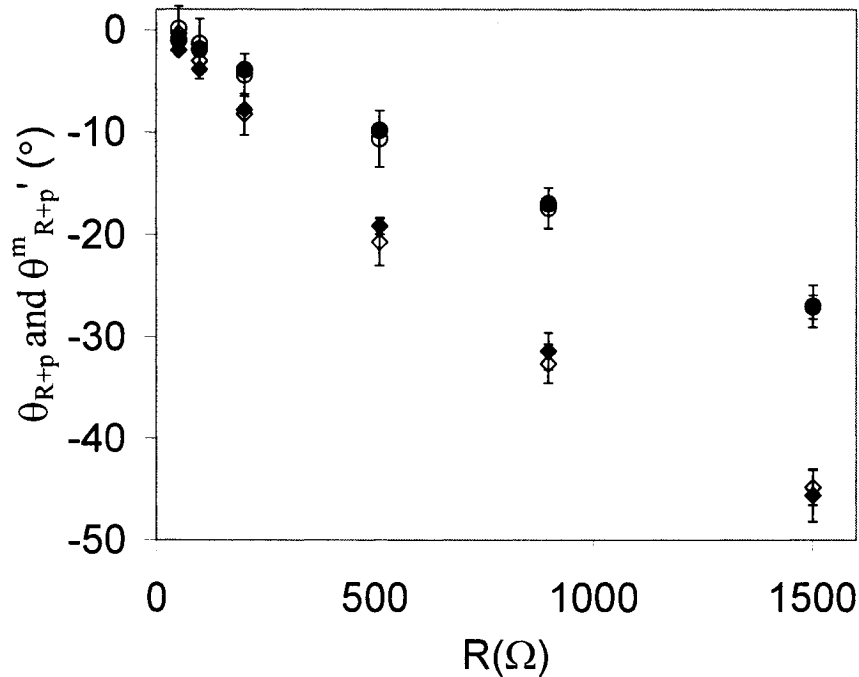


Figure 3-5: Phase angle between i and V_R for the P6139A probe (\diamond : measured and corrected, \blacklozenge : model) and the P5100 probe (\circ : measured and corrected, \bullet : model) as a function of load resistance at 13.56 MHz.

We decided to modify the value of C_p to see if a small modification of it can lead to a constant $\Delta\theta_{R+p}$. Therefore, the model was executed again while the probe capacitance value was increased. Using a $C_p = 4$ pF, a relatively constant value of $\Delta\theta_{R+p}$ (considering the measurement uncertainty) was found, and this value is equal to $-34 \pm 1^\circ$ as can be seen in Figure 3-4. From now on, a corrected C_p value

of 4 pF is used for the P5100 probe. The predicted θ_{R+p} and corrected measured phase angle $\theta_{R+p}^m [\circ] = (\theta_{R+p}^m - \Delta\theta_{R+p})$ are shown in Figure 3-5.

3.4 Application

The results obtained from the calibration of the phase angle are now applied to assess the electrical characteristics of a miniature pulsed atmospheric pressure glow discharge plasma torch, the so-called APGD-*t*. Briefly, the APGD-*t* consists of two concentric electrodes electrically isolated from each other by a plasma confinement quartz tube (2 mm i.d. and 4 mm o.d.). The central electrode is a capillary tube (0.17 mm i.d. and 0.36 mm o.d.) and the ground electrode is made of a silver epoxy layer painted along a 2.5 cm length on the exterior of the quartz tube. Helium gas flows between the inner electrode and the quartz tube at 1 slm resulting in an approximated plasma total volume of 76 mm³ and jet of ~3 mm long and 0.5 mm diameter. The estimated electron density and temperature at the exit of the quartz tube are 10¹¹ cm⁻³ and 1900 K, respectively (see [73] for a detailed description of its construction and properties).

The analysis is conducted with an ultimate goal of calculating the resistive power dissipated in the APGD-*t*. Atmospheric pressure glow discharge (APGD) sources are capacitively-coupled plasma devices which, when miniaturized, represent very large capacitive loads as compared to other standard-size plasma devices of such geometry [99,100]. In fact, their small capacitance gives rise to large capacitive impedance, the magnitude of which increases with rising excitation frequency. Thus, at high frequency, miniature capacitive sources accentuate the probe loading effect on the circuit.

In the set-up of the APGD-*t*, a homemade series inductor L [μ H] is used in order to best match the complex impedance of the APGD-*t* + voltage probe system. A L

= 6.3 μH is used with the P6139A probe, while for the P5100 probe, this value is increased to $L = 12.9 \mu\text{H}$. Both arrangements give rise to a system gain (described as the ratio of the torch voltage to the source voltage, $V_T [\text{V}] / V_s$) close to 10. As a confirmation of the probe loading effect, the impedance matching become poor and the gain of the system was reduced by 3 fold when the voltage probe is withdrawn from the circuit.

3.4.1 Measurements

The RF signal delivered to the APGD- t is generated using an arbitrary waveform generator (Hewlett-Packard 33120A, BW = 15 MHz, $50 \text{ mV}_{\text{ppk}}-10 \text{ V}_{\text{ppk}}$, 50Ω output impedance, max. power = 250 mW) set at a carrier waveform frequency of 13.56 MHz, and which is amplitude-modulated (10-50% duty cycle) by a variable duty-cycle square wave generator (Racal-Dana F64, AM-FM-sweep-trig/pulse-function generator). The signal is amplified with a broadband RF amplifier (Amplifier Research 75A250, 75 W, 10 kHz-250 MHz, 50Ω input/output impedances). The P5100 voltage probe is used to measure the voltage across the APGD- t and the CT-2 transmitter with the P6041 probe are used to measure the circuit current.

Typical measured waveforms of the plasma torch voltage V_T and circuit current i are presented in Figure 3-6. During the ON phase (of the 10% duty cycle), the torch voltage and circuit current are $439 \text{ V}_{\text{pk-to-0}}$ ($310 \text{ V}_{\text{rms}}$) ($\pm 2\%$) and $287 \text{ mA}_{\text{pk-to-0}}$ ($203 \text{ mA}_{\text{rms}}$) ($\pm 2\%$), respectively. The corresponding plasma torch + voltage probe impedance amplitude is $|Z_{T+p}| = 1527 \Omega$. The measured phase angle θ_{T+p} is $-115 \pm 3^\circ$ ($\pm 3\%$), which value, before correcting for the cable lengths effect, appears unrealistic (i.e. higher than -90°). By subtracting the phase angle induced

by the probe cable length, $\Delta\theta_{T+p} = -34 \pm 1^\circ (\pm 3\%)$, one obtains a corrected phase angle of $\theta_{T+p}' = -81 \pm 4^\circ (\pm 5\%)$.

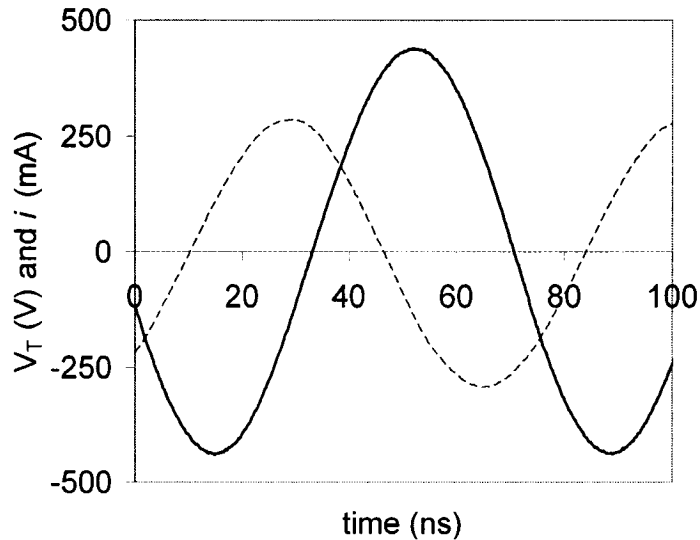


Figure 3-6: V_T (—) and i (- - -) waveforms for the APGD- t excited at 13.56 MHz.

3.4.2 Determination of the resistive power

An electrical model of the plasma device + probe circuit is developed in order to calculate the resistive power dissipated in the APGD- t from the measured electrical characteristics. Capacitively-coupled discharges, such as the APGD- t , can be represented by a RC circuit. The resistance and capacitance can be mounted either in parallel [[99], [31], [101], [72]] or in series [46]. The schematic of the APGD- t electrical circuit is presented in Figure 3-7. The plasma torch is represented by a capacitor, C_T [F], in series with a resistor, R_T [Ω]. C_T represents the device dielectric layer and the electrode sheaths, while R_T represents the bulk quasi-neutral region of the plasma. This model is a simple yet reliable representation of such a device. For cold conditions (no plasma), R_T is removed

from the circuit and the APGD-*t* is then represented by a pure capacitance $C_T = 1.5 \text{ pF}$ [73]. When the plasma is ignited, R_T appears due to the formation of an electrically-conductive region which makes up for most of the plasma volume, and C_T increases following the compression of the electrode sheaths.

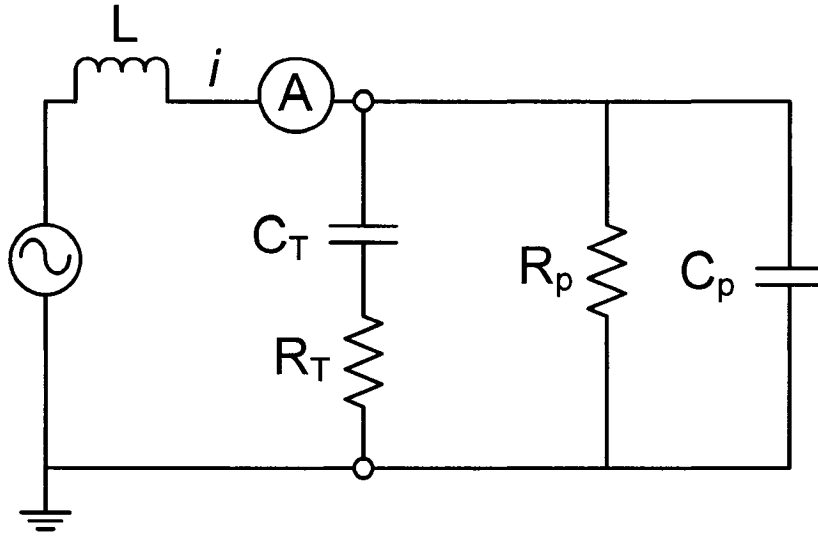


Figure 3-7: Schematic of the electrical circuit of the APGD-*t*.

Equation 3-5 describes the plasma torch impedance, $Z_T [\Omega]$, in the Laplace domain, where the plasma torch time constant is $\tau_T [s] = R_T C_T$. The voltage probe impedance, Z_p , was given earlier by equation 3-1 and a value of $C_p = 4 \text{ pF}$ is used (P5100 probe capacitance). The equivalent impedance of the plasma torch combined with the voltage probe is described by equation 3-6 and the total impedance of the circuit, $Z_{Total} [\Omega]$, is described by equation 3-7. Equations 3-8 and 3-9 describe the basic relations between V_{T+p} , V_s , V_T and i .

$$Z_T(s = j\omega) = \frac{\tau_T s + 1}{C_T s} \quad (3-5)$$

$$Z_{T+p}(s) = R_p \frac{(\tau_T s + 1)}{(\tau_p \tau_T) s^2 + (\tau_p + \tau_T + R_p C_T) s + 1} \quad (3-6)$$

$$Z_{Total}(s) = \frac{L \tau_p \tau_T s^3 + (\tau_p + \tau_T + R_p C_T) L s^2 + (L + R_p \tau_T) s + R_p}{(\tau_p \tau_T) s^2 + (\tau_p + \tau_T + R_p C_T) s + 1} \quad (3-7)$$

$$V_s = Z_{Total} i \quad (3-8)$$

$$V_{T+p} = Z_{T+p} i = Z_{T+p} \frac{1}{Z_{total}} V_s \quad (3-9)$$

$$\theta_{T+p} = \frac{360^\circ}{2\pi} \tan^{-1} \left(\frac{\text{Im}[Z_{T+p}]}{\text{Re}[Z_{T+p}]} \right) = \dots$$

$$\dots = \frac{360^\circ}{2\pi} \tan^{-1} \left(\frac{R_p \tau_T \omega (1 - \tau_p \tau_T \omega^2) - R_p (\tau_p + \tau_T + R_p C_T) \omega}{R_p \tau_T \omega^2 (\tau_p + \tau_T + R_p C_T) + R_p (1 - \tau_p \tau_T \omega^2)} \right) \quad (3-10)$$

From the measurements of Z_{T+p} and θ_{T+p}' , R_T and C_T are determined with the help of equations 3-6 and 3-10. The resistive power dissipated in the plasma torch is determined through the following steps:

1. Define the plasma parameters: f [s^{-1}] and duty cycle DC [%].
2. Define the probe characteristics: R_p and C_p .
3. Measure $V_{T-rms} = V_{T+p}$, i_{rms} , θ_{T+p}' and calculate θ_{T+p}' .
4. Calculate $P_{T+p} = V_{T-rms} i_{rms} \cos(\theta_{T+p}') DC$. (3-11)
5. Calculate $Z_{T+p} = V_{T-rms} / i_{rms}$.

6. Knowing Z_{T+p} and θ_{T+p}' , solve equations 6 and 10 to get R_T and C_T .

7. Knowing R_T and C_T , calculate Z_T .

8. Calculate $V_{R_T-rms} = R_T i_{T-rms} = R_T V_{T-rms} / |Z_T|$. (3-12)

9. Calculate $P_{R_T} = V_{R_T-rms} i_{R_T} DC = [(V_{R_T-rms})^2 / R_T] DC$. (3-13)

The plasma excitation conditions are $f = 13.56$ MHz and $DC = 10.12\%$ ($\pm 0.02\%$). Consequently, $|Z_{T+p}| = 1527 \Omega$ ($\pm 29\%$) and $\theta_{T+p}' = -81^\circ$ ($\pm 5\%$). The power dissipated in the torch and voltage probe is $P_{T+p} = 1$ W ($\pm 29\%$) with $R_T = 979 \Omega$ ($\pm 34\%$) and $C_T = 4$ pF ($\pm 6\%$) with $|Z_T| = 3100 \Omega$ ($\pm 2\%$). The voltage across the plasma torch resistance is $V_{R_T-rms} = 98$ V_{rms} ($\pm 38\%$) while the resistive power dissipated in the plasma is $P_{R_T} = 1$ W ($\pm 42\%$). This power value agrees with the one reported in a previous study on the APGD-*t* [73], and though the voltage probe strongly affects the phase angle, the power is completely dissipated in the plasma torch and not in the voltage probe ($P_{T+p} = P_{R_T}$). The uncertainty on the power measurement is considerable, but it is explained by its large sensitivity to the phase angle value as reported independently by Guo *et al.* [102]. The uncertainties of 3% and 5% on θ_{T+p} and θ_{T+p}' respectively are relatively small compared to the uncertainty found in other studies [47]. The uncertainty on the power calculation is greatly amplified by the use of the cosine of θ_{T+p}' in eq.11. Also, the difference in uncertainty between R_T and C_T is explained by the calculation algorithm where R_T does not affect $|Z_{T+p}|$ over a large range of values, while a small change in C_T has a drastic effect (see [73] for more detailed on this phenomenon).

3.5 Conclusions and recommendations

This study reported on the difficulties associated with the use of commercial voltage probes to assess the electrical properties of a miniature, high-capacitive impedance plasma source excited at 13.56 MHz. It was found that large probe capacitance, excitation frequency and difference in cable lengths all introduce a considerable phase angle between the probed circuit current and voltage signals. Both experiments and model-based calculations confirm that the phase angle must be calibrated when high-frequency excitation is used. For the Tektronix P6139A voltage probe, the averaged phase angle induced by the probe cable was $-2 \pm 1^\circ$. For the Tektronix P5100 voltage probe, the resulting averaged phase angle induced by the probe cable was $-34 \pm 1^\circ$.

This paper also presented a practical, economic and reasonably accurate method to assess the plasma parameters of a miniature capacitive plasma source. The method requires the measurement of the voltage across the plasma source, the circuit current and their relative phase angle as well as the knowledge of the probe capacitance, resistance and their uncertainties. An electrical model of a miniature plasma source, the APGD-*t*, was created and the probe calibration methodology applied. The resistive power dissipated in the torch was estimated at 1 W ($\pm 42\%$). The torch resistance, capacitance and impedance magnitude were 979Ω ($\pm 34\%$), 4 pF ($\pm 6\%$) and 3100Ω ($\pm 2\%$), respectively. For a better accuracy on the calculation of the electrical properties, it is recommended to select voltage probes with small capacitance and with cable lengths equal to the length of the current probe cable (if used). Also, probe manufacturers should provide the true value, not a typical one, of impedance and capacitance for each probe they sell.

3.6 Acknowledgments

The authors wish to thank L. Cusmich, F. Caporuscio, and A. Gagnon for their technical assistance as well as Randy White and Dave McDonald from Tektronix for their technical support. This project was funded by the Natural Sciences and Engineering Research Council of Canada (NSERC), through the Discovery and Canada Research Chairs programs, the Fonds québécois de la recherche sur la nature et les technologies (FQRNT), and McGill University.

3.7 References

See the global bibliography at the end of the thesis document.

CHAPTER 4

ATOMIC OXYGEN PRODUCTION & PLASMA AFTERGLOW CHEMISTRY

This chapter consists of an article accepted for publication in the *Plasma Processes and Polymers* journal in July 2006. The editors of the journal invited the Ph.D. candidate to submit an article based on the presentation she made at the 17th *International Symposium on Plasma Chemistry* held in Toronto in August 2005. This article presents essentially an optimization study of the gas flow rates used in the APGD-*t* to improve the production of atomic oxygen and a survey of the plasma afterglow chemistry.

In the first section, an introduction describes various plasma sources used for biomedical applications. A section presenting the experimental details follows. A discussion follows on the effect of the helium and molecular oxygen flow rates on the atomic oxygen production. A survey of the possible reactions paths in the plasma afterglow is also presented, in order to identify the reactive species that can possibly react with a remote biological tissue or polymeric surface located a few millimeters downstream of the APGD-*t* nozzle exit.

Atomic Oxygen Production and Exploration of Reaction Mechanisms in a He-O₂ Atmospheric Pressure Glow Discharge Torch

Valérie Léveillé* and Sylvain Coulombe

Department of Chemical Engineering, McGill University, 3610 University Street,
Montréal (Québec), Canada, H3A 2B2 Fax : +1 (514) 398-6678;

*E-mail: valerie.leveille1@mail.mcgill.ca

4.1 Summary

This article reports the performance of a miniature atmospheric pressure glow discharge torch (APGD-*t*) conceived for the production of reactive species participating in bio-applications. Two operating parameters were varied: the plasma-forming gas flow rate (0.5-1.5 slm He) and the flow rate of O₂ (0-50 sccm), which was injected downstream from the plasma-forming zone and used as a source of reactive species. The production of reactive species (O) was optimized and the air entrainment in the plasma jet minimized for a He gas flow rate of 1-1.5 slm and an O₂/He volumetric ratio of 0.3 vol.-%. A survey of the possible reaction pathways in the plasma afterglow (plasma jet) suggests that the reactive species present in the plasma afterglow and possibly reaching a remote substrate are metastable He(2³S), ground state O, OH, O₂(a¹Δg), O₂(b¹Σg⁺), N₂ and N₂⁺ and O₃.

4.2 Introduction

There have been several recent investigations reporting the use of atmospheric pressure non-thermal plasma sources for bio-applications. Amongst the main applications we find sterilization, surface functionalization, micro-contact printing of proteins on polymers, preparation of drug delivery systems and regeneration of skin [21-24,29,30,103]. An increasing number of novel applications such as micro-surgery, local removal or modification of cells and surface patterning require a localized treatment capability. In such situations, large area APGD (atmospheric pressure glow discharge) sources are being replaced by compact size, potentially handheld, plasma sources capable, in some instances, of producing directed plasma jets. Amongst those novel miniature non-thermal plasma sources, we recognize the “Plasma Needle” of Stoffels and colleagues, the “Plasma Pencil” of Laroussi and Lu and the Atmospheric Pressure Glow Discharge Torch (APGD-*t*) developed in our laboratory by L veill  and Coulombe [29,33,73,104].

The APGD-*t* produces a non-thermal plasma jet that generates and efficiently transports reactive species towards a remote substrate. Its novelty lies in the use of a central capillary electrode that both enhances the electric field and allows the injection of various sources of reactive species downstream from the plasma-forming region without affecting the plasma characteristics [73]. In this study, basic performance data and the results of the optimization of the atomic oxygen (O) production for various plasma-forming gas (He) and O₂ flow rates are reported. O₂ is chosen as the source of reactive species since it is known to be a powerful oxidant for the etching of organic films and bacterial membranes [8,80,81]. It is also known to alter the wettability of polymeric surfaces and is suspected to oxidize the cells’ membrane and adhesion proteins [29,105]. Also, a

survey of potential reaction pathways in the plasma afterglow is presented in an attempt to identify the reactive species that are likely to reach and react with a remote substrate.

4.3 Experimental part

The APGD-*t* is a miniature, handheld, capacitively-coupled dielectric barrier discharge (DBD) device made up of sterilizable parts (Figure 4-1b). The APGD-*t* construction, presented in details in a previous publication, consists of two concentric electrodes electrically isolated from each other by a plasma confinement quartz tube as can be seen in Figure 4-1a [73]. The stainless steel, central, capillary tube electrode (0.36 mm o.d.) is powered with an amplitude-modulated 13.56 MHz excitation. Under nominal conditions, square-wave amplitude modulation at 10% duty cycle and 100 Hz is used. The ground electrode consists of silver epoxy paste painted over the downstream end of the plasma confinement tube (see Figure 4-1c). The same end of the quartz tube is shaped into a converging nozzle with an exit diameter of 500 μm (a torch with a 150 μm exit diameter was also developed).

The plasma-forming gas, helium, is injected through the side arm of the tee holding the torch assembly together, while the source of reactive species (O_2) is injected either in the capillary electrode or with the plasma-forming gas (see Figure 4-1a). It was shown that the injection of the source of reactive species through the capillary electrode is less disruptive to the stable operation of the plasma torch and leads to a higher rate of production of O species at the nozzle exit plane of the APGD-*t* [73]. This configuration was adopted for the present study. The input voltage to the RF amplifier was kept constant for all conditions reported in the present study and, thus, the power delivered to the torch adjusted itself to its impedance.

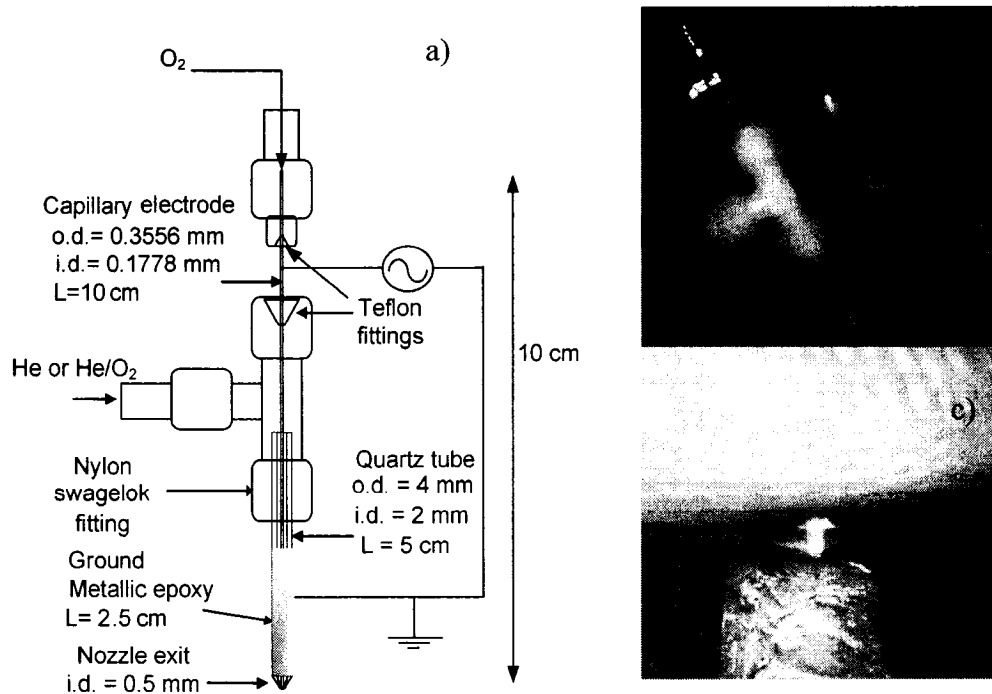


Figure 4-1: a) Schematic of the APGD-*t*, b) pictures of the APGD-*t* and c) the APGD-*t* plasma jet impinging on the forefinger.

We previously reported on the constraints imposed on a plasma source used in bio-applications [106]. Most importantly, the jet must have a low temperature, typically under 50°C, and be able to produce and transport reactive species to the surface under treatment. Other constraints, such as the need to sterilize the torch assembly, to avoid contamination of the treated surface due to normal torch operation, and the formation of a straight jet must be considered as well. Of particular concern is the erosion of the unprotected capillary electrode. SEM images of the tip and outside wall of the capillary electrode, aged for approximately 20 hours under normal conditions, revealed no sign of melting and/or evidences of arcing. Corroborating the SEM observations, no atomic emission lines, associated with the metallic constituents of the stainless steel, were present in the optical emission spectra [73]. Conversely, such atomic emission

was observed when the APGD-*t* was operated at low-frequency alternative current (AC) excitation (~10 kHz) and high voltage (>1 kV) (results not published).

The alignment of the capillary electrode tip along the vertical axis of the torch is critical for the formation of a long and straight jet, and for the efficient generation and transport of the reactive species. Unfortunately, achieving the perfect alignment of the capillary tube proves to be a difficult task and thus, some variability in the performance data is expected over time. Under typical operating conditions, the tip is recessed by a few 100 μm from the nozzle exit plane. If the tip end is located outside of the quartz nozzle, other excitation and dissociation channels involving air molecules are promoted at the expense of exciting He atoms to metastable states, as well as dissociating and exciting the source of reactive species injected in the capillary electrode.

Helium (He: 99.998 vol.-% purity) was used as the plasma-forming gas and extra dry oxygen (O₂: 99.6 vol.-% purity) as the source of reactive species. Pictures of the plasma jet were captured with a telemicroscope (Edmund Optics, 16X) and the optical emission spectra with a low-resolution UV-VIS spectrometer (Ocean Optics USB2000) covering the 200-850 nm spectral window (the intensity was calibrated with a tungsten filament lamp EPT-1373). A bi-convex lens (50 mm-diameter, 15 cm focal length) was used to collect the plasma emission and to focus it onto a 400 μm optical fiber (200-800 nm) attached to the spectrometer. The maximum uncertainty for all relative emission measurements was $\pm 3\%$.

4.4 Results and discussion

4.4.1 Optimization of the atomic oxygen production

Telescopic Image of the Plasma Jet

In Figure 4-2, pictures of the plasma jet are presented for three different flow rates of He (no O₂ added). Under typical operating conditions (1 slm He), the plasma jet is approximately 2.5 mm long (the jet's visible diameter at the nozzle is 500 μm). One can see that the jet is symmetrical, confirming the proper alignment of the capillary electrode inside the quartz nozzle. The pictures reveal that an increase of the He flow rate increases the length of the jet, which is beneficial for the transport of reactive species to a remote substrate.

On the other hand, larger flow rates involve higher He consumption and more momentum transfer to the substrates which process, in the case of bio-applications, could also become a constraint (ex. detaching cells from a Petri dish). The exact cause for the flow structure that develops at 0.5 slm upon mixing of the plasma jet with the surrounding air (i.e. structure similar to a bow shock) is currently under investigation.

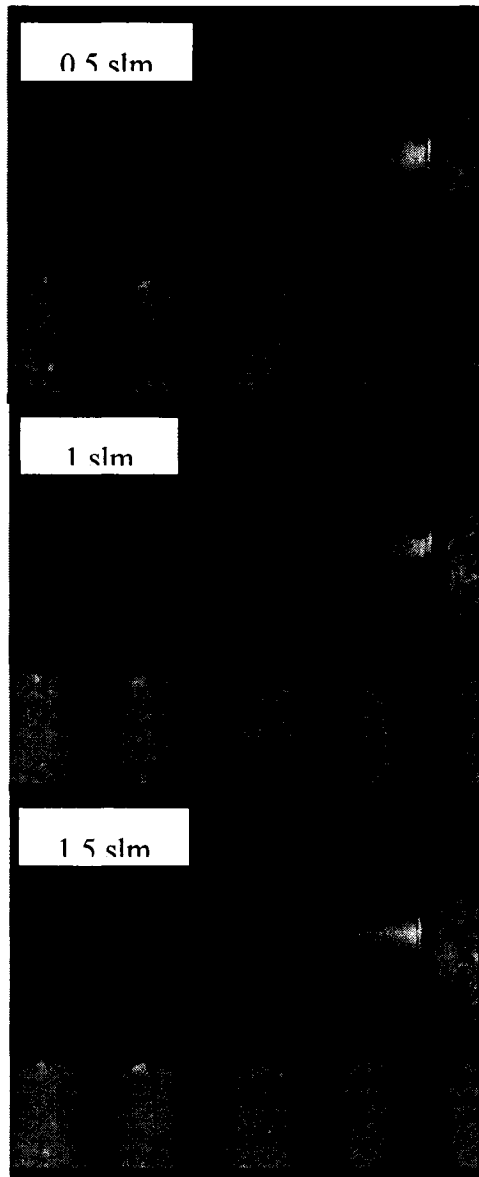


Figure 4-2: Pictures of the plasma jet produced by the APGD-*t* at ≈ 1 W for different He flow rates.

4.4.2 Effect of O₂ flow rate

From the preliminary telescopic image analysis and spectroscopic investigation, it was demonstrated that the injection of the source of reactive species (10 sccm O₂) in the capillary electrode leads to a negligible reduction of the plasma jet length, while the injection of an equivalent amount to the plasma-forming gas (mixture of 1 vol.-% of O₂ in He) quenched the plasma [73]. In order to optimize the O production, the amount of O₂ injected in the capillary electrode was varied from 0 to 50 sccm. Figure 4-3a shows the effect of the O₂ flow rate on the relative intensity of the atomic oxygen line (777 nm), along with the He (706 nm) and N₂⁺ (391 nm) lines measured at the nozzle exit. All emission intensities were normalized with respect to the maximum emission intensity of the O line (777 nm). The injection of ~3 sccm of O₂ in the capillary electrode produced a maximum of emission from the O (777 nm) line. This is referred as the optimum O₂/He ratio from now on; ~0.3 vol.-%. We infer from this observation that a small amount of O₂ is required to achieve an optimum production of O and that this production might be limited by the availability of electrons and other excited species such as He metastable atoms in the (2¹S) and (2³S) states. In this latter statement, we assume that the increase of the O₂ flow rate has a negligible effect on the electron (He excitation) temperature. From this point on, the combination of the He atoms in the (2¹S) and (2³S) metastable states will be represented by the unique symbol He*.

The He excitation temperature was measured to be ~1914 K, a value which accounts for a low level of excitation [73]. The very low emission from the N₂⁺ ion (391 nm) seems to indicate that the majority of He* atoms were quenched by Penning ionization with O₂ molecules (reaction 10, Table 4-1) and very few were left for the Penning ionization of the N₂ molecule (reaction 38). This agrees with the fact that the quenching rate of He* atoms by O₂ molecules is higher than that

by N₂ molecules. The rapid spatial decay of the excited neutral He line (706 nm) indicates that a significant fraction of the plasma electrons recombines through collision with the O₂ molecules (reaction 13) and are used to ionize (reaction 16), dissociate (reactions 17 and 30) and excite the O₂ molecules (reaction 36) instead of the He excitation.

Figure 4-3b shows that the corresponding circuit current, torch voltage and relative phase angle between those two signals are not altered by the O₂ flow rate. Since the end of the capillary electrode is only slightly recessed from the exit plane of the quartz nozzle, the mixing region for the two gas streams occupies a small volume of the inter-electrode region and thus, the presence of O₂ in this small volume does not significantly affect the plasma-sustaining conditions. The corresponding resistive power dissipated in the torch is ~0.24 W.

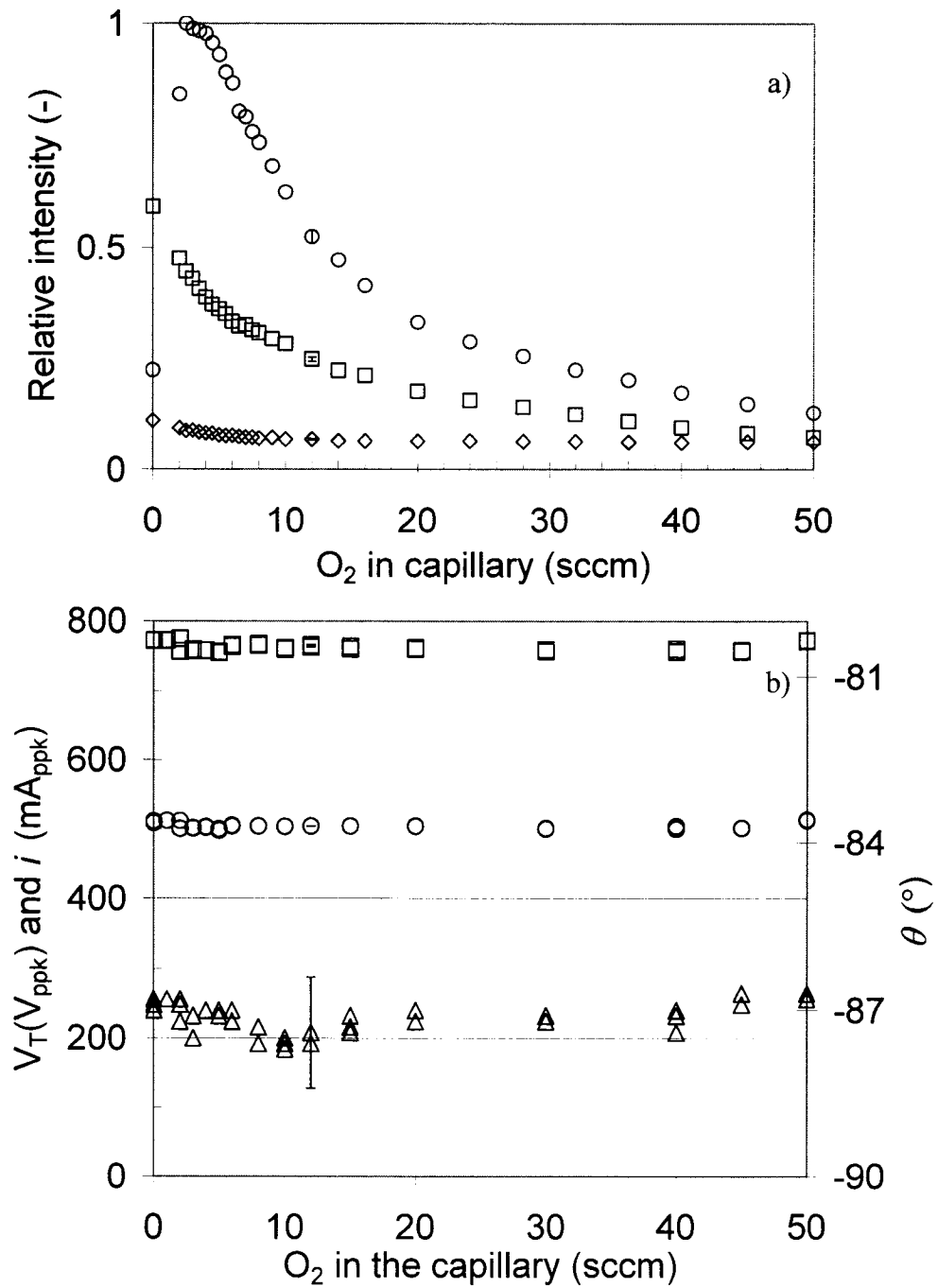


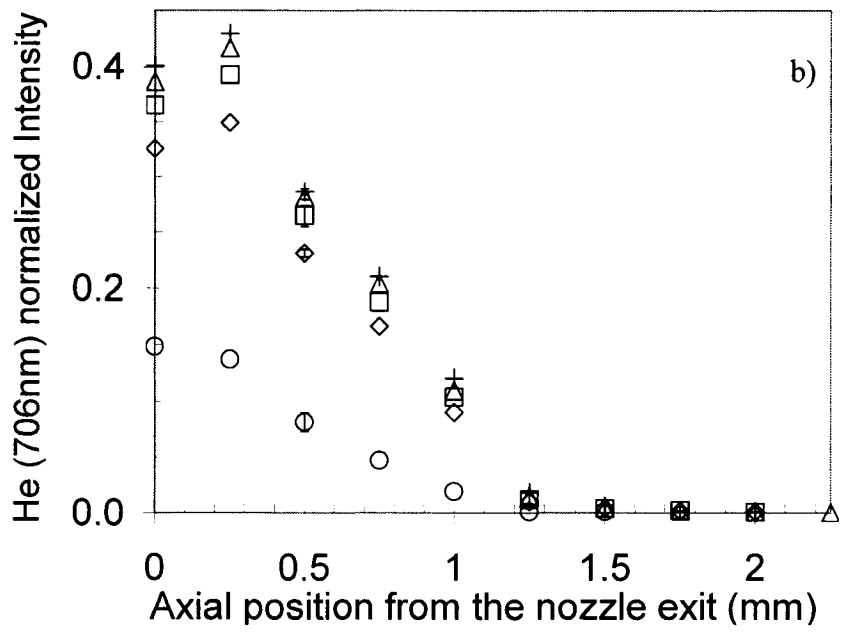
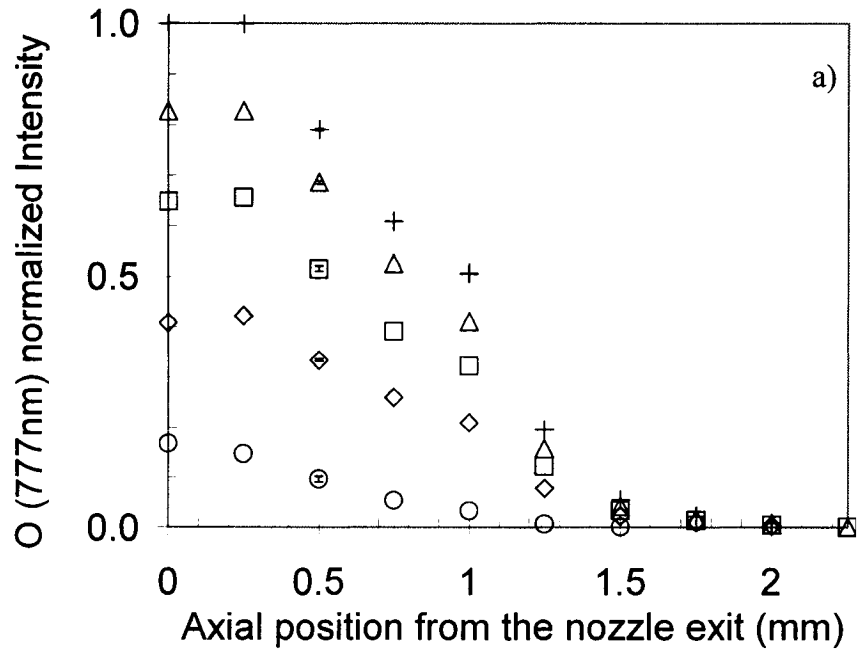
Figure 4-3: a) Normalized peak line emission intensity of O at 777 nm (o), He at 706 nm (□) and N_2^+ at 391 nm (◇) near the nozzle exit, and b) torch voltage V_T (□) and circuit current i (O) and their relative phase angle (Δ) for different O_2 flow rates in the capillary electrode.

4.4.3 Effect of He flow rate

He gas flow rate was also optimized to obtain a maximum of excited atomic O emission at the nozzle exit and to reduce the air entrainment in the jet. During this series of experiments, the O₂/He volumetric ratio was kept constant at the optimal value of 0.3 vol.-%, while the He flow rate was varied.

Figure 4-4a and b shows the normalized intensity of selected emission lines as a function of the distance to the torch nozzle exit plane. As can be seen with Figure 4-4a, an increase of the He flow rate leads to an increase of the emission intensity of the O (777 nm) line. This phenomenon is directly attributable to a more significant convective transport along the jet axis. The He (706 nm) line follows a similar trend, though the effect is not as pronounced and, in fact, the intensity of this line tends to reach a plateau at high He flow rates (Figure 4-4b).

It is interesting to note that Kieft *et al.* did not observe this phenomenon with the “Plasma Needle”, where the He intensity remained constant over the same range of flow rates [31]. We also attribute this phenomenon to a more significant convective transport in the APGD-*t* configuration, while this effect is not as important with the “Plasma Needle” since the plasma fills only a tiny fraction of the gas flow channel. Thus, in the APGD-*t*, the production of excited O is not limited over the range of He flow rates considered. This can be explained by the fact that the upper energy level of the O (777 nm) is lower than the upper energy level of He (706 nm) (10.74 eV and 22.72 eV, respectively).



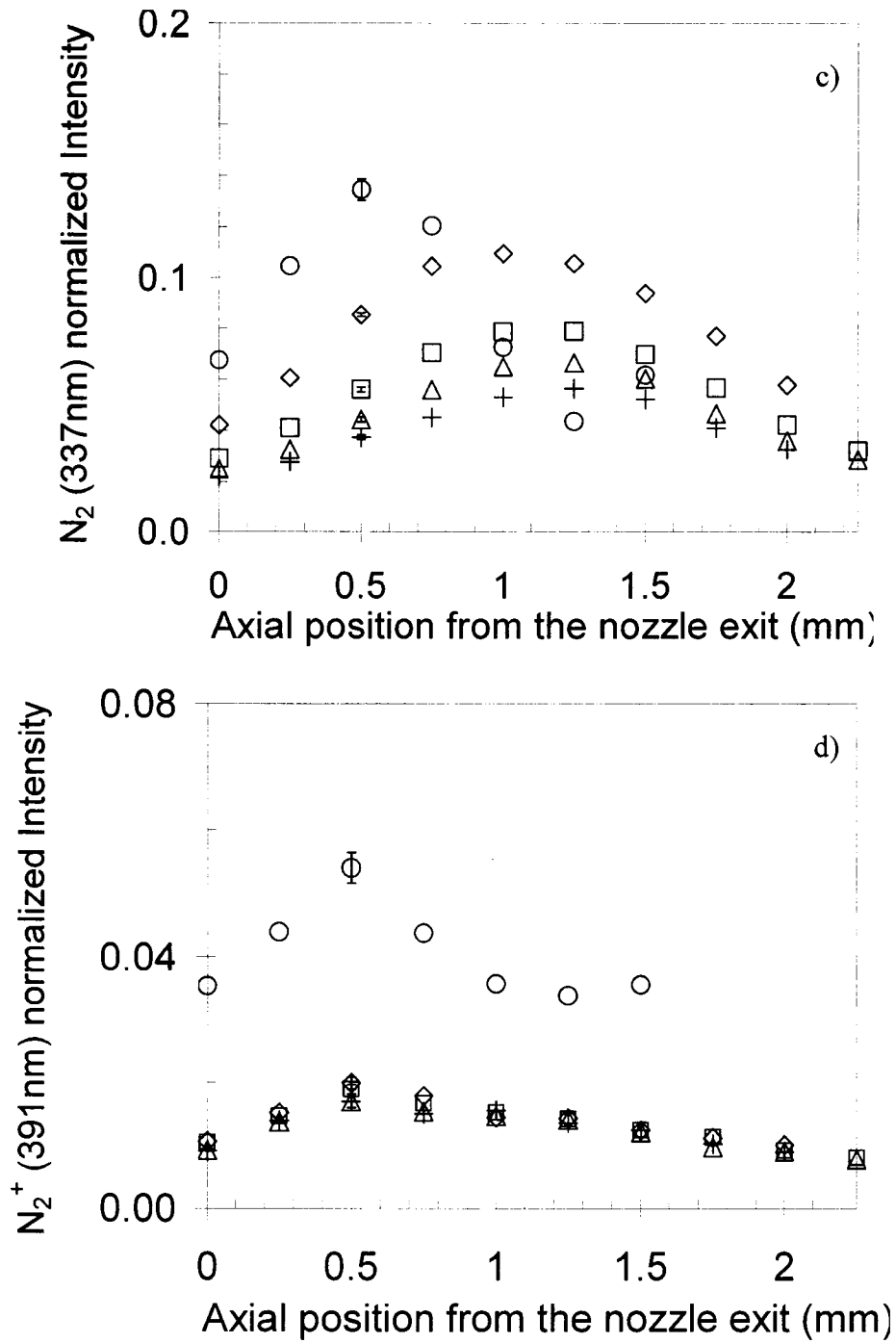


Figure 4-4: Axial distribution of the normalized peak emission intensity of a) O at 777 nm, b) He at 706 nm, c) N_2 at 337 nm and d) N_2^+ at 391 nm for 0.5 (o), 0.75 (◇), 1 (□), 1.25 (Δ) and 1.5 (+) slm of He.

Air entrainment in the plasma jet is confirmed with Figure 4-4c showing emission from N_2 molecules. Two phenomena are observed: 1) the emission intensity increases for all axial positions as the He flow rate is decreased and 2) the peak in emission intensity tends to shift toward the nozzle exit with the decrease of the He flow rate. The first observation can be explained by the diffusive entrainment of air into the plasma afterglow which, at a particular location in the afterglow, scales with the ratio of the species diffusion to gas convection time scales; i.e. the mass transfer Péclet number ($Pe_i = UR/D_i$, where U is the characteristic bulk velocity, R the characteristic dimension and D_i , the mass diffusivity of species i). The lower the gas velocity, the lower the Péclet number and thus, the more significant the extent of species diffusion is with respect to convection. The excitation temperature might play a role in the second observed phenomenon. Indeed, one expects the isotherms to recess back towards the torch nozzle as the He flow rate is reduced.

Intuitively, the He^* (~ 20 eV) atom density distribution should follow a similar optical emission trend as that of the excited He (706 nm) atoms. However, since the He^* atoms have a longer lifetime than the other excited states, one can postulate that such species would be found further downstream in the plasma afterglow. To verify this hypothesis, the emission from the $N_2^+(B^2\Sigma_u^+)$ state (391 nm) was monitored as N_2^+ ions are produced mainly by Penning ionization with He^* atoms in the afterglow (reaction 38) [72]. Figure 4-4d shows the effect of the He flow rate on the N_2^+ (391 nm) emission line intensity. It was observed that the N_2^+ emission is the highest at the lowest He flow rate (Figure 4-3). Interestingly, the peaks in the N_2^+ emission intensity coincide for all He flow rates. Also, the effect of the He flow rate on the emission intensity is weak for flow rates in the 0.75-1.5 slm range. Furthermore, the location of the peaks of the N_2^+ emission intensity for all He flow rates investigated is closer to the nozzle exit than what was observed with the N_2 (337 nm) line. Those results indicate that the He^* atoms

are produced but that the corresponding upper energy state is rapidly depopulated upon contacting with the N₂ molecules (and likely O₂ molecules too) from air. The fact that the N₂⁺ (391 nm) emission line intensity does not vary significantly with the He flow rate (for flow rates > 0.75 slm) is an indicator that the He* production does not increase with an increase of the He flow rate.

4.5 Afterglow plasma chemistry

This section of the article presents a survey of reaction pathways leading to the formation of reactive species in the He/N₂/O₂/H₂O plasma afterglow, that are likely to be transported and to react with a remote substrate exposed to the plasma stream, such as cells or polymeric surfaces.

To get a feeling of the excitation capability of the APGD-*t*, the average electron density (n_e) in the plasma-forming region was estimated from the plasma resistance and assuming $T_e \approx 1914$ K (the He excitation temperature at the nozzle exit) [73]. Its value was $\sim 10^{11}$ cm⁻³. This estimate for n_e compares well with the value of $\sim 10^{11}$ cm⁻³ reported by Kieft *et al.* for the “Plasma Needle” operating at power levels in the 10 -100 mW range [31]. Also, this estimated value further supports the claim that the APGD-*t* produces a non-thermal plasma, since its n_e value lies in the typical range for non-thermal plasmas (10^8 - 10^{14} cm⁻³) [107].

The measured excitation temperature at the nozzle exit plane was ~ 1914 K (~ 0.165 eV) for typical operating conditions [73]. Assuming an electron temperature of ~ 1914 K for a Maxwellian electron energy distribution, one finds that, near the nozzle exit plane, roughly ~ 0.2 electron/cm³ ($\sim 0.0001\%$) have enough energy to ionize the He atoms to the first ionization level (24.6 eV) and $\sim 4 \times 10^6$ electrons/cm³ (0.003 %) have enough energy to produce He* atoms in the (²S) state (19.8 eV). This latter percentage is extremely small, but Gorse *et al.*

demonstrated that a ratio of $[\text{He}(2^3\text{S})]/[\text{He ground state}]$ as low as 0.0001% affects the EEDF in an He/N₂ post discharge [108]. Thus, it is not expected that ionized He will be present in the plasma afterglow. However, it is expected that the APGD-*t* will produce a small concentration of He* atoms, He(2³S) or He(2¹S) states, that should affect the EEDF and participate to the plasma chemistry.

A non-exhaustive list of reactions possibly taking place in the afterglow of the APGD-*t* is presented in Table 4-1. These reactions have been chosen because their kinetic reaction rate constants are significant under the typical operating conditions (pressure, gas nature and temperature, electron temperature, electron and gas densities) of the APGD-*t*. The reactions were considered for three zones in the plasma: (1) in the inter-electrode plasma glow (0-2.5 cm upstream of the nozzle exit), (2) at the nozzle exit plane and (3) in the plume of the plasma jet (few mm downstream from the nozzle exit). Reactions in zone (1) are mainly determined by the magnitude of the electric field. It is assumed that reactions in zone (2) occur at an electron temperature of 0.165 eV while reactions in zone (3) involve heavy species only; thus their rate constants are calculated for a temperature that is as close as possible to the neutral gas temperature found in the APGD-*t* afterglow (≈ 313 K). For the sake of clarity, all atoms and molecules in the ground state were written without their electronic configuration (for instance, ground state O(³P) atom is written O).

Usually, the He* specie is formed by electron impact excitation with a rate constant proportional to the electric field (reaction 1). Two types of He* atoms can be formed: He(2¹S) and He(2³S). Some experimental studies have demonstrated that the He(2¹S) atom density is usually much lower than its He(2³S) counterpart [65,71].

Table 4-1: Reactions occurring in the plasma glow and afterglow, with their respective rate constants calculated for specific T_e or T_g .

#	Reactions	Rate constant, k ($\text{cm}^3 \text{mol}^{-1} \text{s}^{-1}$)	T_g / T_e (K/eV)	Pressure (bar)	Ref.
	He plasma				
1	$\text{He} + e \rightarrow \text{He}^* + e$	Function of (E/N)	-	-	[66]
2	$\text{He} + e \rightarrow \text{He}^+ + 2 e$	Function of (E/N)	-	-	[66]
3	$\text{He}^* + 2 \text{He} \rightarrow \text{He}_2 + \text{He}$	$2.0 \times 10^{-34} \text{ cm}^6 \text{ s}^{-1}$	n/a	n/a	[66]
4	$\text{He}^+ + 2 \text{He} \rightarrow \text{He}_2^+ + \text{He}$	n/a	n/a	n/a	[109]
5	$\text{He}_2 + \text{M} \rightarrow 2 \text{He} + \text{M}$	$1.0 \times 10^6 \text{ s}^{-1}$	n/a	1	[66]
6	$\text{He}_2^+ + e \rightarrow \text{He}^* + \text{He}$	8.9×10^{-9}	n/a	1	[66]
7	$2 \text{He}_2 \rightarrow 2 \text{He} + \text{He}_2^+ + e$	1.5×10^{-9}	n/a	n/a	[66]
8	$2 \text{He}^* \rightarrow \text{He}_2^+ + e$	1.5×10^{-9}	n/a	n/a	[66]
9	$2 \text{He}^* \rightarrow \text{He}^+ + \text{He} + e$	8.7×10^{-10}	n/a	n/a	[110]
	He/O ₂ / H ₂ O plasma				
10	$\text{He}^* + \text{O}_2 \rightarrow \text{He} + \text{O}_2^+ + e$	2.4×10^{-10}	n/a	n/a	[66]
11	$\text{He}_2 + \text{O}_2 \rightarrow 2 \text{He} + \text{O}_2^+ + e$	1.0×10^{-10}	n/a	1	[111]
12	$\text{He}_2^+ + \text{O}_2 \rightarrow 2 \text{He} + \text{O}_2^+$	1.0×10^{-9}	n/a	1	[111]

13	$O_2^+ + e \rightarrow 2O$	4.8×10^{-7}	n/a	n/a	[66]
14	$He^* + O \rightarrow He + O^+ + e$	4.3×10^{-10}	500	n/a	[84]
15	$O_2 + O^+ \rightarrow O_2^+ + O$	2.0×10^{-10}	n/a	n/a	[112]
16	$O_2 + e \rightarrow 2e + O_2^+$	3.3×10^{-15}	298	n/a	[112]
17	$O_2 + e \rightarrow e + [O(^1D) \text{ or } O(^1S)] + O$	1.8×10^{-19}	n/a	n/a	[113]
18	$O(^1D) + O_2 \rightarrow O_3$	2.4×10^{-10}	298	0.01	[114]
19	$O_3 + O(^1D) \rightarrow O_2 + [2O \text{ or } O_2(^3\Sigma_g^-, v)]$	3.8×10^{-10}	298	n/a	[115]
20	$O_3 + O(^1D) \rightarrow O_3 + O\cdot$	3.5×10^{-10}	300	0	[116]
21	$O(^1D) + H_2O \rightarrow 2 \cdot OH$	2.2×10^{-10}	200-350	n/a	[117]
22	$O_3 + O(^1D) \rightarrow 2O_2$	1.2×10^{-10}	n/a	n/a	[115]
23	$O_3 + H\cdot \rightarrow \cdot OH + O_2$	2.9×10^{-11}	300	n/a	[118]
24	$O(^1D) + O_2 \rightarrow O\cdot + O_2(^3\Sigma_g^-, v)$	4.0×10^{-11}	298	n/a	[117]
25	$O(^1D) + O_2 \rightarrow O\cdot + O_2(b^1\Sigma_g^+)$	7.4×10^{-11}	298	n/a	[115]
26	$O_2(^1D) + H\cdot \rightarrow \cdot OH + O\cdot$	$< 3.0 \times 10^{-13}$	298	n/a	[119]
27	$O(^1D) + O_2(b^1\Sigma_g^+) \rightarrow O + O_2(a^1\Delta_g)$	8.1×10^{-14}	n/a	n/a	[120]
28	$O_3 + O\cdot \rightarrow 2O_2$	1.9×10^{-14}	385	0.13	[121]
29	$He + O(^1D) \rightarrow He + O\cdot$	$< 1.5 \times 10^{-15}$	300	0	[116]
30	$O_2 + e \rightarrow 2O + e$	7.1×10^{-21}	n/a	n/a	[113]

31	$O_2(a^1\Delta_g) + O_2 \rightarrow O_3 + O\cdot$	2.9×10^{-21}	298	0	[122]
32	$O_2 + H\cdot \rightarrow \cdot OH + O\cdot$	2.5×10^{-21}	300	n/a	[123]
33	$O_2(a^1\Delta_g) + e \rightarrow O^- + O$	2.3×10^{-22}	n/a	n/a	[124]
34	$O_3 + H_2O \rightarrow H_2O_2 + O_2$	$< 1.1 \times 10^{-22}$	296	0.97	[125]
35	$O\cdot + H_2O \rightarrow 2 \cdot OH$	4.5×10^{-24}	300	n/a	[126]
36	$O_2 + e \rightarrow O_2(b^1\Sigma_g^+) + e$	3.1×10^{-26}	0.165 eV	n/a	[127]
37	$He + O_3 \rightarrow He + O_2 + O$	2.3×10^{-26}	n/a	n/a	[66]
	He/O₂/N₂ plasma				
38	$N_2 + He^* \rightarrow N_2^+ + He + e$	6.9×10^{-11}	298	1.06	[128]
39	$N_2 + He_2 \rightarrow N_2^+ + 2He + e$	3.0×10^{-11}	n/a	1	[129]
40	$N_2 + He_2^+ \rightarrow N_2^+ + He_2 + e$	1.4×10^{-9}	n/a	1	[129]
41	$N_2 + O(^1D) \rightarrow O + N_2$	5.4×10^{-11}	298	n/a	[115]
42	$N_2 + O\cdot \rightarrow NO + N$	3.9×10^{-22}	>1400	n/a	[123]
43	$N_2 \rightarrow N + N$	1.0×10^{-22}	>3390	1	[130]
44	$N_2 + N^+ \rightarrow N_2^+ + N$	9.4×10^{-29}	313	n/a	[131]
45	$N_2 + e \rightarrow 2N + e$	2.1×10^{-30}	0.165 eV	n/a	[131]
46	$N + e \rightarrow N^+ + 2e$	9.3×10^{-39}	0.165 eV	n/a	[131]
47	$N_2 + e \rightarrow N_2^+ + 2e$	4.0×10^{-46}	0.165 eV	n/a	[131]

In order to determine if the He(2^3S) specie was present in the plasma jet, we made an attempt to observe it by laser-induced fluorescence (LIF) spectroscopy with the round trip (i.e. wavelength of pumping laser is the same as the fluorescence wavelength) involving the He ($2^3S \rightarrow 2^3P$, 388 nm) transition. Unfortunately, due to the very small size of the APGD-*t* jet, the low plasma density and the heavy collisional quenching associated with the atmospheric pressure plasma conditions, the observed LIF signal was very weak and it was impossible to recover it from the noise.

An indirect method to detect He(2^3S) atoms is to observe the optical emission from the $N_2^+(B^2\Sigma_u, v=0)$ molecule, since this molecule is produced by Penning ionization with He(2^3S) (reaction 38) [63,72,132]. In order to excite the ground state levels of N_2 molecule and N_2^+ ions to the $N_2^+(B^2\Sigma_u, v=0)$ level, energies as high as 18.8 eV and 3.17 eV, respectively, are required [124]. The reaction rate constant for the electronic ionization of N_2 molecules (reaction 47) is negligible compared to the one for the Penning ionization of N_2 molecules in the afterglow. The other N_2^+ production mechanisms, which involve He_2 (reaction 39) and He_2^+ (reaction 40), have similar reaction rate constants compared to the Penning ionization with He(2^3S). However, the He_2 production implies the presence of He(2^3S) (reaction 3) and the He_2^+ production implies the presence of He^+ (reaction 4) atoms, which specie has been found to be present in a negligible amount at the nozzle exit plane. Therefore, Penning ionization dominates the $N_2^+(B^2\Sigma_u, v=0)$ ions formation and we deduce from this that the He(2^3S) specie is present in the APGD-*t* afterglow. The lifetime for the He(2^3S) state is much shorter than for the $N_2^+(B^2\Sigma_u, v=0)$, thus the He(2^3S) atoms are less likely to reach a substrate placed a few mm downstream from the nozzle exit [132].

In the previous section it was estimated that almost no electrons have enough energy to ionize He atoms (confirmed by a numerical study of an APG) [133].

Also, the He^+ specie is lost by recombination with ground state He specie to form the He_2^+ at atmospheric pressure (reaction 4). Therefore, it is suspected that He^+ will not play an important role in the plasma afterglow chemistry.

The helium dimer molecule, $\text{He}_2(a^3\Sigma_u^+)$, is produced mainly from the collision of He in the ground state with He^* (reaction 3), but it dissociates rapidly through impact with another collision partner (reaction 5), by Penning ionization with N_2 molecules (reaction 37) and by ionization of O_2 molecules (reaction 12). A study showed that a partial pressure of 200 mTorr N_2 in 1 atm of He was enough to consume all $\text{He}_2(a^3\Sigma_u^+)$ molecules, and that its presence could thus be neglected in the plasma [134]. Since the plasma generated by the APGD-*t* is discharged in air (79 vol.-% of N_2), the helium dimer is most likely to disappear. As a confirmation of this hypothesis, no emission from the strongest $\text{He}_2(a^3\Sigma_u^+)$ band around 465 nm is observed by OES. Therefore, the $\text{He}_2(a^3\Sigma_u^+)$ molecule is most likely to be consumed rapidly in the plasma afterglow and thus, will not react with a remote substrate.

Another molecule, He_2^+ , is produced by the dissociation of $\text{He}_2(a^3\Sigma_u^+)$ (reaction 7) molecules. The He_2^+ ions could also be produced from the collision of two He^* atoms with one He^+ ion (reaction 4) and by the impact of two He^* atoms (reaction 8). However, He_2^+ ions formed will be quenched by dissociative recombination with electrons (reaction 6), dissociative charge transfer with O_2 molecules (reaction 12) and by charge exchange with N_2 molecules (reaction 40). To support this hypothesis, a 2-D numerical study of an APG in He with N_2 as an impurity revealed that the $\text{He}_2(a^3\Sigma_u^+)$ and He_2^+ atom densities were two orders of magnitude lower than He^* and N_2^+ atom densities [133]. Based on those results, we conclude that the $\text{He}_2(a^3\Sigma_u^+)$ and He_2^+ molecules must be produced in the plasma zone but are quickly quenched by air molecules to form new chemical species such as N_2^+ and O_2^+ in the plasma afterglow.

The injection of O₂ molecules in the core of the plasma afterglow and the presence of entrained air provide a series of new reactions. The production of O₂⁺ ions can be accomplished through Penning ionization with He* atoms (reaction 10), by a charge transfer reaction involving O₂ molecules and O⁺ molecules (reaction 15), by dissociative charge transfer with He₂⁺ (reaction 12) and by electron impact ionization (reaction 16). No emission from O₂⁺ at 560 nm (strong band head) was observed by OES in the afterglow of the APGD-*t* [73]. This indicates that O₂⁺ ions in high energy states might recombine to give O atoms (reaction 13) or that very few of them are generated in the plasma afterglow.

In the plasma afterglow, the metastable states O(¹D) and O(¹S) could be formed. They are mainly produced by electronic impact dissociation (threshold energy > 5 eV) (reaction 17). However, the quenching rate constants of O(¹D) atoms by O₂ molecules (reaction 18) and by O₃ molecules (reaction 19) are very high. No emission from O(¹D) at 630 nm or 636 nm (³P - ¹D₁), nor O(¹S) at 557.7 nm was observed by OES [73]. Thus, we believe that O(¹D) and O(¹S) atoms are not appreciably present in the plasma afterglow and will not react with a remote substrate.

Regarding the ground state O(³P) specie, it could be produced in the afterglow through several reaction paths (reactions 13, 15, 17, 19, 20, 24-27, 29-33 and 37). In a previous paper, we mentioned that He* atoms could directly dissociate O₂ molecules (He* + O₂ → 2 O) [73]. However, in the O₂ and O₂⁺ energy diagram, no dissociation energy corresponds exactly to the upper energy levels of He* atoms and, thus He* atoms should not dissociate O₂ molecules by a one-step reaction [135]. In fact, the most probable channel of formation of O atoms through a reaction with He* atoms is the Penning ionization of O₂ molecules (ionization energy ~12 eV) (reaction 10), followed by the electron impact dissociation of O₂⁺ ions (reaction 13) [135]. Since excited O atoms (777 nm) were detected by OES

up to a few mm downstream from the nozzle exit and, logically, the corresponding ground state O atom density should be much higher, we infer that ground state O atoms are present far downstream from the nozzle exit plane.

The O^+ ion is formed mainly by the collision of He^* with O atoms (reaction 14), but it is also quenched by O_2 molecules (reaction 15). Based on the similarity of the reaction rate constants of formation and quenching of O^+ ions, we cannot conclude on the impact of this ion on the plasma chemistry. On the other hand, no O^+ emission was observed (at 465 nm) in the plasma afterglow, even very near the nozzle exit plane of the APGD-*t* [73]. Therefore, we assume that this specie will not play a role in surface reaction.

Singlet $O_2(b^1\Sigma_g^+)$ and $O_2(a^1\Delta_g)$ species are known to oxidize biomolecules and molecular functional groups (i.e. amines, amino acids, phospholipids, fatty acids, nucleic acids proteins, vitamins, etc.) [136]. The $O_2(b^1\Sigma_g^+)$ specie is produced by the collision of $O(^1D)$ atoms with O_2 molecules (reaction 25), and to a much smaller extent by the electronic excitation of O_2 molecules (reaction 36). It disappears when it collides with $O(^1D)$ specie to create $O_2(a^1\Delta_g)$ (reaction 27). The $O_2(a^1\Delta_g)$ specie is quenched by O_2 molecules (reaction 31) or disappears by electronic dissociative attachment (reaction 33) although the reaction rate constants associated with those processes are very weak ($\sim 10^{-21}$ - 10^{-22} $cm^3 mol^{-1} s^{-1}$). It was found that $O_2(b^1\Sigma_g^+)$ molecule concentration is usually much less important than that of its $O_2(a^1\Delta_g)$ counterpart [136]. No emission from $O_2(a^1\Delta_g)$ at 634 nm or 703 nm, nor from $O_2(b^1\Sigma_g^+)$ at 762 nm was detected by OES [73]. However, since those emission bands are weak in the visible spectral region, it is possible that the $O_2(a^1\Delta_g)$ and $O_2(b^1\Sigma_g^+)$ molecules, to a lesser extent, are present in the plasma afterglow of the APGD-*t* and will react with a remote biological surface.

The main formation path of O₃ molecule consists of the collision of an O(¹D) atom with the O₂ molecule (reaction 18). We tried to measure the O₃ density by absorption spectroscopy using a standard argon-mercury lamp (6035Hg/Ar, Oriel), but encountered difficulties due to the small volume of the plasma jet. Since O₃ is one of the most important molecules formed in a dielectric barrier discharge in air and in O₂, we presume that it is produced in the APGD-*t* afterglow and that it will react with a remote organic substrate or with biomolecules [137,138].

Concerning the OH radical, this specie is formed mainly through the collision of water molecules with O(¹D) atoms (reaction 21), and by the collision of O₃ molecules with atomic hydrogen (reaction 23). Since trace amounts of OH have been detected by OES in the APGD-*t* afterglow several mm downstream from the nozzle exit [73], OH is a reactive specie likely to react with a remote substrate.

The effect of nitrogen species on the plasma afterglow chemistry is now considered. It is observed that N₂ and N₂⁺ molecules were present a few mm downstream from the nozzle exit (Figure 4-4). Another nitrogen species, N(⁴S), could be produced by electron impact dissociation (energy threshold ~9.5 eV) (reaction 45) at the nozzle exit. However, it cannot be produced by collision of a N₂ molecule with an O atom (reaction 42) since this reaction requires $T_g > 1400$ K, and T_g in the plasma jet of the APGD-*t* is only near 313 K. Furthermore, it cannot be produced by thermal dissociation of N₂, since this reaction requires $T_g > 3390$ K (reaction 43). Since no significant emission from N(⁴S) at 575 nm or 746 nm is observed at the nozzle exit, we do not expect this specie to be present or to react with a remote substrate.

The NO molecule is formed by the collision of N₂ with an O radical (reaction 42). However, this reaction occurs at $T_g > 1400$ K, a temperature that is much higher than $T_g \approx 313$ K of the APGD-*t* plasma afterglow. Furthermore, no emission from

this molecule was observed by OES, and thus its potential participation in the surface chemistry is ignored. Another specie, N^+ , is not likely to be present in the APGD-*t* afterglow, since the N ionization energy threshold is 14.53 eV and the first N^+ energy level lies above 24 eV [139]. In fact, no emission from N^+ was observed in the 200-800 nm spectral window, even near the nozzle exit of the APGD-*t*.

In summary, the species present in the He/O₂ APGD-*t* jet discharging in air which are likely to reach a remote substrate are metastable He(2^3S) atoms, ground state O atoms and N₂, N₂⁺, O₂($a^1\Delta_g$), O₂($b^1\Sigma_g^+$), OH and O₃ molecules.

4.6 Conclusions

This article outlined the results of an optimization of gas flow rates in a miniature atmospheric pressure glow discharge torch (APGD-*t*) in an attempt to maximize the production of reactive species playing an important role in remote exposure surface treatments. The injection of O₂ in the APGD-*t* afterglow using a capillary electrode did not affect the plasma-sustaining conditions. Indeed, the circuit current, torch voltage and their relative phase angle were not altered by the O₂ flow rate. A plasma-forming gas flow rate (He) of 1-1.5 slm and a volumetric ratio of 0.3 vol.-% O₂/He allowed a maximum production of atomic oxygen with minimum air entrainment in the plasma jet. The electron density in the plasma-forming region was estimated to be $\sim 10^{11} \text{ cm}^{-3}$, a value which lies within the non-thermal plasma range. An analysis of the afterglow plasma chemistry suggests that the metastable He(2^3S), ground state O, OH, O₂($a^1\Delta_g$), O₂($b^1\Sigma_g^+$), N₂, N₂⁺ and O₃ molecules produced by the APGD-*t* are able to reach a remote substrate located a few mm away from the torch's nozzle. In future work, further characterization of the cells and polymeric surfaces treated by the plasma jet is

required in order to clearly identify which reactions occur at the surface and to elucidate which reactive species are participating.

4.7 Acknowledgments

The authors wish to thank Dr. Gorik Nersisyan and Dr. Richard Engeln for their constructive comments on the limits of the laser-induced fluorescence technique. The authors also wish to acknowledge the financial support provided by the Natural Sciences and Engineering Research Council of Canada (NSERC), through the Discovery, Canada Research Chairs and the Idea to Innovation grant programs (I2I), the Fonds québécois de la recherche sur la nature et les technologies (FQRNT) and McGill University.

4.8 Collected references

See the global bibliography at the end of the thesis document.

CHAPTER 5

ATTEMPT TO USE THE LASER-INDUCED FLUORESCENCE SPECTROSCOPY TECHNIQUE FOR MEASUREMENT OF THE METASTABLE HE ATOM DENSITY

This chapter reports an attempt to use the laser-induced fluorescence (LIF) spectroscopy technique to detect helium atoms in their metastable states in the plasma afterglow of the APGD-*t*. An introduction presents the rationale for using LIF to detect the He metastable state, which is followed by a description of the LIF experimental set-up. Some preliminary LIF measurements and a discussion on the limits of application of the LIF technique are also presented.

5.1 Introduction

He metastable atoms are very useful in the plasma afterglow because they act as an energy reservoir sustaining plasma excitation and they participate to the creation of reactive species. In Chapter 3, it was found that the detection of N_2^+ (391 nm) molecules by OES in the APGD-*t* afterglow was an indicator of the presence of He metastable atoms since N_2^+ (391 nm) can be produced by Penning ionization of N_2 . However, N_2^+ can also be produced by electron impact ionization of N_2 and molecules in lower energy levels of N_2^+ and by collisional impact ionization of N_2 with He_2 or He_2^+ . Therefore, direct measurement of the density of He metastable atoms in the plasma afterglow would help understanding the plasma afterglow chemistry.

Since the first metastable energy levels of He do not permit radiative transitions to the ground state, they are not observable by OES. Such energy levels can potentially be probed by LIF, whereby electrons from metastable energy states are

excited to higher energy levels which allow radiative transitions to lower energy levels. An attempt was made to probe the He atoms in the (2^3S) metastable state using LIF. The results are presented in this chapter.

5.2 Experimental set-up

The schematic of the LIF set-up is shown in Figure 5-1 and the time diagram for laser synchronization with the plasma pulse is shown in Figure 5-2. For all experiments, the typical operating conditions of the APGD-*t* are 870 V_{ppk}, 650 mA_{ppk}, power modulation frequency of 100 Hz, duty cycle of 10%, and 1 slm of He. A digital pulse generator (BNC 565, 500 ps resolution) is used to trigger (12 V, 1 ms, 100 Hz) the function generator (Racal-Dana F64, 100 ns fall time in 50 Ω), which modulates the carrier waveform signal (13.56 MHz) itself generated by a waveform generator (Hewlett-Packard 33120A, 15 MHz bandwidth). The resulting output is amplified by a RF amplifier (Amplifier Research 75A250, 75W, 10 kHz-250 MHz, 50 Ω input/output impedances) and delivered to the APGD-*t*. The pulse generator also triggers (5 V, 1 ms, 10 Hz) the flash lamp of the laser system, itself triggering the oscilloscope recording.

The LIF system consists of a pulsed NdYAG pump laser (Quantel Brilliant B, Q-switched, 10 Hz, 5 - 6 ns pulse, 1064 nm fundamental harmonic, 2nd and 3rd harmonics generators, 850 mJ/pulse max, 8.5 W max) and a tunable dye laser (Quantel TDL 90, UV extension, 200 - 750 nm spectral range, line width = 0.08 cm⁻¹). A remote control box is used to control the flash lamp voltage and synchronization mode as well as the delay between the flash lamp and the Q-switch firings. The dye laser wavelength scanning, scan speed and mode are controlled using another remote control box.

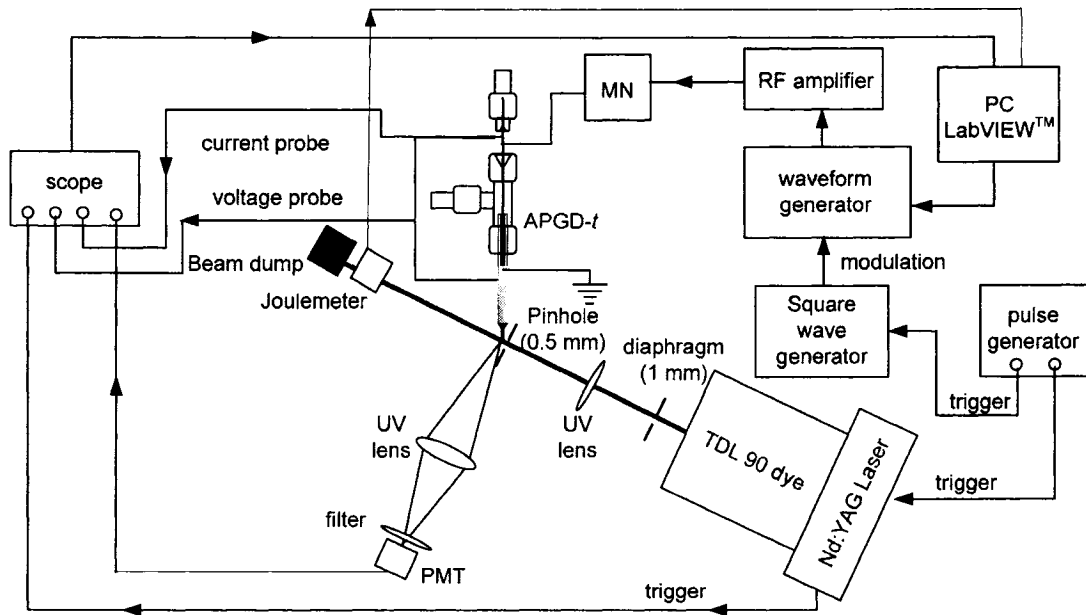


Figure 5-1: Diagram of the LIF experimental set-up.

The electron density was estimated to be $\sim 10^{11} \text{ cm}^{-3}$ in the plasma-forming region of the APGD-*t*, which value is relatively small (see Chapter 4). For such low electron density plasma, the 2-level system presented in Figure 1-2 accurately represents the processes occurring in the APGD-*t* plasma. The atoms in the He(2^3S) metastable state are excited by a 388.9 nm laser to the (3^3P) upper state and fluorescence at 388.9 nm is observed. To generate a laser beam at the wavelength of 388.9 nm, the frequency-doubled fundamental harmonic of the pump laser beam (532 nm) is used to pump the Rhodamine 640 dye, and the resulting laser beam is (frequency) mixed with the residual IR laser beam at 1064 nm. The determination of the exact dye laser wavelength required for frequency mixing is done using equation (5-1). The wavelength λ is the desired resulting laser wavelength (388.9 nm), λ_2 is the IR laser wavelength (1064 nm) and λ_1 is the dye laser wavelength to be determined. The resulting λ_1 is equal to 612.80 nm.

$$\frac{1}{\lambda} = \frac{1}{\lambda_1} + \frac{1}{\lambda_2} \quad (5-1)$$

The dye solution is prepared by dissolving 0.2 g of Rhodamine 640 perchlorate (Exciton, Inc. max $\lambda = 602$ nm, λ range = 589 - 623 nm) into 250 ml of 100% pure anhydrous ethyl alcohol (Commercial Alcohols Inc.). This latter solution is gradually diluted in ~500 ml of the anhydrous ethyl alcohol to get the right concentration (g/L) of dye in the laser system. The final dye concentrations in the oscillator and in the amplifier circulation systems are ~0.1 g / L and ~ 0.05 g / L, respectively.

The resulting UV laser beam at 388.9 nm has a diameter of 5 mm, which is then trimmed using a 1 mm diaphragm. A UV lens (Newport, SBX058, focal distance = 15 cm, diameter = 50 mm) is used to focus the laser beam onto the plasma jet at a perpendicular angle with respect to the torch axis. A second pinhole is placed just in front of the focal point of the lens in order to cut the laser beam down to 0.5 mm in diameter. The laser energy at 388.9 nm is measured by an energy meter (Gentec-EO, QE12SP-H-MB-DO, efficient surface = 12 mm², 0.19 - 20 μ m, 8 μ J - 840 mJ, 10 V/J). The laser energy measured after the pinhole is ~2 mJ when a minimum delay between the Q-switch and flash lamp firings is used (214 μ s). A second UV lens (Newport, SBX022, focal distance = 50.2 mm, diameter = 24.5 mm) is used to focus the laser-induced fluorescence onto a photomultiplier tube (PMT) (Hamamatsu, H6780-20, 300 - 900 nm, rise time = 0.78 ns, gain = 10⁶). A UV filter (Newport, P10-390-F, 390 nm \pm 2 nm, band pass = 10 nm, \varnothing = 25 mm) is placed just in front of the PMT to cut all light except the 388.9 nm laser light.

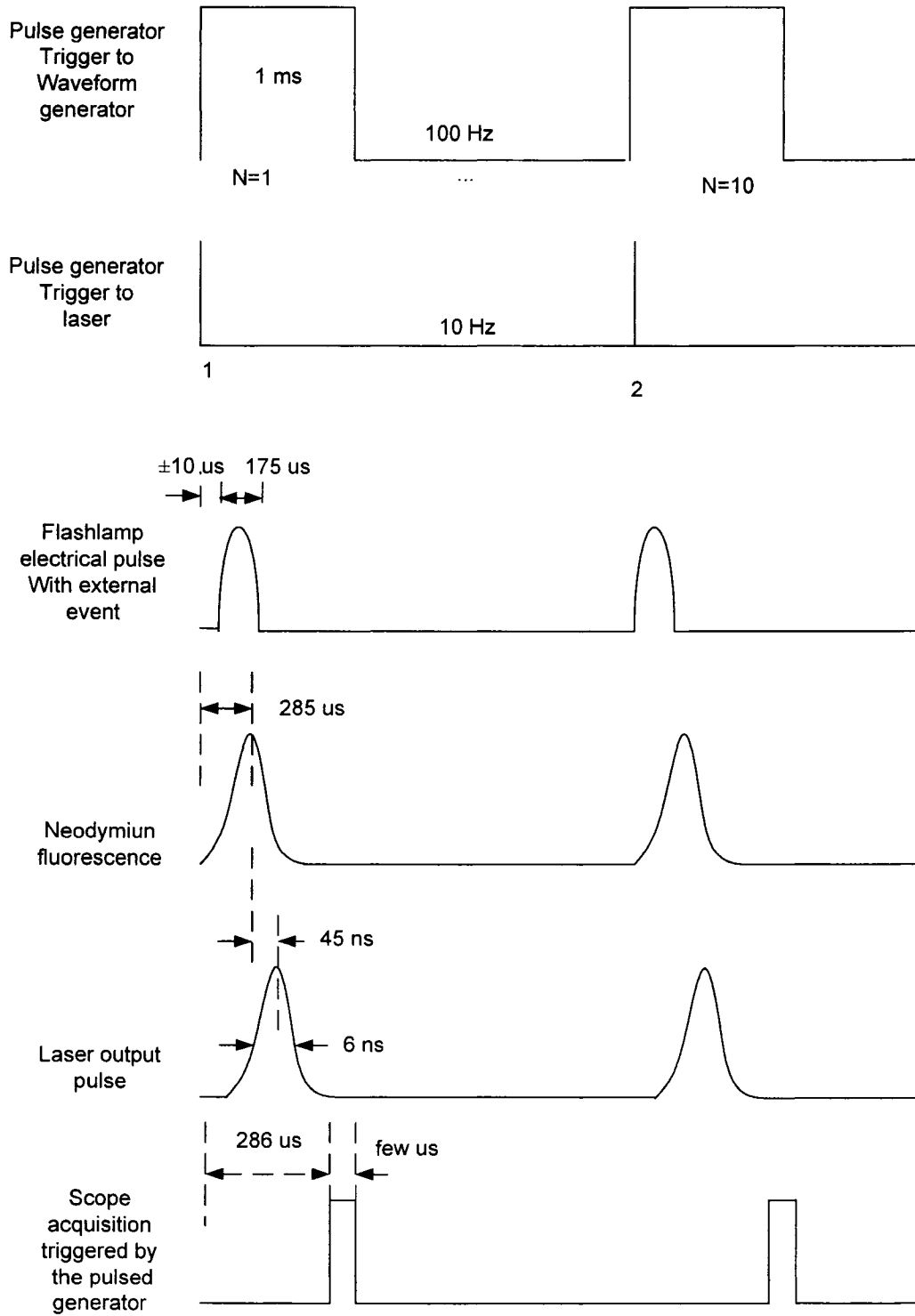


Figure 5-2: Time diagram of the laser synchronization with the plasma modulation signal.

The relative peak fluorescence intensity (PFI, [mV]) of the LIF signal is measured since it is a simple and accurate way to monitor the relative density of He atoms in their metastable state, as long as the laser has a short rise time [65]. The PFI measurements are made in the plasma jet at distances, d , of 3 mm and 1.5 mm from the nozzle exit. The PFI captured by the PMT is displayed on the scope and averaged over 3 samples of 64 cumulated waveforms. The measured PFI signal includes a strong signal coming from the stray laser light (SLL, [mV]). SLL is also measured before the plasma was ignited at the same location as the PFI measurements, in order to extract the LIF signal only.

5.3 Results and discussion

Table 5-1 presents typical results of LIF measurements. It can be seen that SLL signal is very strong and that the resulting corrected PFI signal is weak. The level of signal noise for those conditions was ~ 1 mV. When the laser beam is focused at a distance very far from the nozzle exit, no SLL is observed. At $d = 3$ mm, some SLL is present and at $d = 1.5$ mm, SLL is more than the double of the level observed at $d = 3$ mm. These observations indicate that one of the causes of SLL is reflection of the laser beam on the nozzle walls; the reflected rays are then captured by the PMT, resulting in the SLL signal.

Table 5-1: LIF signal measured at two different distances from the nozzle exit.

d (mm)	SLL (mV)	PFI + SLL (mV)	PFI (mV)
1.5	110 ± 1	129 ± 3	18 ± 4
3.0	48.7 ± 0.8	55.9 ± 0.2	7.2 ± 0.9

Another source of SLL is diffraction of the laser beam when it crosses the 0.5 mm pinhole opening. Some of the rays diffracted by the pinhole might be directed toward the PMT causing the SLL observed signal. No laser scattering due to dust is found. In addition, the operation of the APGD-*t* in an air and at atmospheric pressure provides ideal conditions for severe quenching of the He metastable atoms by the air molecules (O₂, N₂).

To be able to use the LIF technique for the detection of He metastable atoms, modifications of the present experimental set-up are required. These modifications are mainly the increase of the plasma volume, the increase of the power level and the operation of the APGD-*t* in a He (or other inert gas) environment. However, behavior of the He metastable states in the present and in a modified experimental set-up would be very different and comparisons and/or extrapolations might not be useful or even meaningful. The single modification that will preserve the plasma properties is operation of the APGD-*t* in a He environment. By doing so, the density of He metastable atoms produced in the plasma jet would be much higher since those species would not suffer from any quenching. However, this modification of the plasma system set-up makes the laser alignment quite difficult and, therefore it was decided not to pursue LIF measurements in the plasma afterglow of the APGD-*t* since it would have extended this Ph.D. project considerably.

5.4 Conclusions

In this chapter, the experimental set-up, preliminary results and the application limits of the LIF technique for the characterization of the He metastable in the APGD-*t* plasma jet were described. The LIF spectroscopy system was set up to detect the relative density of He(2³S) metastable atoms in the He plasma afterglow of the APGD-*t* operating in air. The detection of metastable He(2³S)

atoms in the plasma jet was unsuccessful due to unfavorable plasma operating conditions. Indeed, the small size (0.5 mm) of the laser light absorption volume, the strong intensity of stray laser light and the operating in air make the LIF measurements very difficult.

FINAL CONCLUSIONS

The main objective of this Ph.D. project was to design, develop and perform a preliminary characterization of an atmospheric pressure glow discharge torch for localized biomedical applications. This objective has been met, along with several sub-objectives, which are now reviewed.

In Chapter 2, the design of the atmospheric pressure glow discharge torch, and the results of a preliminary electrical and spectroscopic characterization were presented. The mini-torch produces a non-thermal plasma jet of 500 μm -diameter and ≈ 2.5 mm-length. A methodology for the determination of the electrical characteristics of this mini-torch from careful electrical probe measurements was developed. The use of pulsed RF excitations at low duty cycle (10%) allowed the operation of the mini-torch at a ≈ 1 W power level. Under these conditions, the gas temperature was ≈ 50 °C, while the He excitation temperature was less than 2000 K. The addition of 1 $\frac{1}{v}$ % O_2 to the plasma-forming gas led to a drastic contraction of the jet. Alternatively, the injection of 10 sccm O_2 through the capillary electrode led to the production and transport of atomic O further downstream in the plasma jet, without significantly altering the electrical properties and jet length.

Chapter 3 presented difficulties associated with the use of commercial passive voltage probes to assess the electrical properties of a miniature, high-capacitive impedance plasma source excited at radio-frequency. It was found that large differences in cable length, probe capacitance and excitation frequency resulted in the introduction of a considerable phase angle between the probed signals (circuit current and load voltage). Both experiments and model calculations confirmed that for each voltage probe, the phase angle must be calibrated when high-frequency excitation is used. This chapter also presented a practical, economic

and reasonably accurate method to assess the plasma parameters of the atmospheric pressure glow discharge torch. The resistive power dissipated in the torch was 1 W ($\pm 42\%$). For a better accuracy on the measurement of the electrical properties of the plasma device, it is recommended to select voltage probes with the smallest capacitance and cable lengths equal to the length of the current probe cable (if used). Furthermore, probe manufacturers should provide true values (not typical values) of the probe impedance and capacitance.

Chapter 4 outlined work done to optimize the operating conditions of the APGD-*t* toward localized biomedical applications. The parametric study considered a He flow rate ranging from 0.5 to 1.5 slm, and 0 to 50 sccm of O₂ was used as the source of reactive species. The injection of O₂ in the capillary electrode to produce atomic oxygen, the reactive species, had negligible effects on the visual appearance of the jet and electrical properties of the APGD-*t*. A He gas flow rate of 1-1.5 slm and a volumetric ratio of 0.3 vol.-% O₂/He led to a maximum production of atomic oxygen with minimum air entrainment in the plasma jet. A survey of the afterglow plasma chemistry suggested that some reactive species produced in the afterglow such as metastable He, O, OH, O₂(a¹Δ_g), O₂(b¹Σ_g⁺), N₂ and N₂⁺ and O₃ should be able to reach a remote substrate and react with it.

In Chapter 5, the laser-induced fluorescence technique, its experimental set-up, some preliminary results and its application limits were described. Laser-induced fluorescence spectroscopy (LIF) was set up to detect the relative density of helium metastable state (2³S) in the He plasma afterglow of the APGD-*t* operating in air. The fluorescence intensity corresponding to metastable He(2³S) states was weak due to the small size of the laser light absorption volume and operation of the plasma source at low-power levels in air at atmospheric pressure.

CONTRIBUTIONS TO KNOWLEDGE

This research project made significant contributions to knowledge. This report reveals that we:

1. Designed and constructed a bench-scale miniature atmospheric pressure plasma source, the APGD-*t*, for localized biomedical applications. The main design novelty is the use of a metallic capillary tube that acts as the powered electrode and also as an injection channel for the source of reactive species. The APGD-*t* is a hand-held device and its input power can be amplitude-modulated from 0.24 W to 5 W, giving rise to gas kinetic temperatures ranging from 40 to 120°C. The plasma jet produced has a diameter of 0.5 mm and a length of 2-3 mm.
2. Developed a calibration method for the phase angle that appears between the plasma load voltage and circuit current, as measured by electrical probes. It was found that the accuracy of the measured phase angle is strongly affected by the voltage probe capacitance and cable length, and by the excitation frequency.
3. Developed a methodology based on a simple circuit model of the plasma source to calculate the power dissipated in a highly capacitive plasma load. The method requires the measurement of the plasma load voltage, circuit current and relative phase angle.
4. Determined the optimal flow rates for the plasma-forming gas (He) and the source of reactive species (O₂) for the production of atomic oxygen. The He flow rate must range from 1 to 1.5 slm and 3 sccm of O₂ must be injected through the capillary electrode.
5. Identified several excited species, such as O, He, OH, N₂ and N₂⁺ by means of optical emission spectroscopy and analyzed the plasma afterglow chemistry. The presence of excited O atoms about 1 mm downstream from the nozzle exit

suggests that ground state O atoms might be found further in the afterglow and reach a remote surface. The rapid extinction of the excited He reveals the fast depletion of electrons in the plasma afterglow. OH, N₂ and N₂⁺ molecules found very far (5-6 mm) from the nozzle exit indicates that these species can reach a remote surface. Also, the presence of N₂⁺ far into the afterglow indicates that metastable He atoms are probably present at such a distance. The theoretical analysis of the plasma afterglow chemistry has shown that other species such as O₂(a¹Δg), O₂(b¹Σg⁺) and O₃ might also reach and react with bio or organic remote substrates.

6. Identified some experimental difficulties associated with the use of the laser-induced fluorescence (LIF) technique to investigate the He metastable state (2³S) in a small He plasma jet (3 mm x 0.5 mm) discharging in air at atmospheric pressure. The encountered difficulties were the low density of He metastable state atoms in such a small plasma volume, in addition to the strong quenching by air molecules.

RECOMMENDATIONS FOR FUTURE STUDIES

In order to continue assessing the properties and potential biomedical applications of the APGD-*t*, additional research work needs to be carried out. It would be interesting to continue 1) characterization of the plasma afterglow, in order to identify and if possible to quantify reactive species present a few mm downstream of the APGD-*t* nozzle exit, and 2) development of localized biomedical applications for the APGD-*t*.

a. Characterization of the plasma afterglow

The identification and, if possible, quantification of reactive species present a few mm downstream of the APGD-*t* nozzle exit is essential to gain more knowledge on the species that will reach a remote surface and react with it. In a parallel research project conducted by Miss Sara Yonson, the APGD-*t* was successfully used to locally remove mammalian cells from a polymeric surface, to temporary permeabilize human liver (HepG2) cells and to functionalize well-defined areas on a polymeric (polystyrene) surface to increase its hydrophilicity and, thus to enhance the adhesion of human mammalian cells (HAAE-1) [140]. However, as mentioned in the plasma afterglow chemistry analysis (Chapter 4), only the presence of OH, N₂ and N₂⁺ molecules has been confirmed at the location of a remote surface using optical emission spectroscopy (Chapters 2 and 3). Therefore, we propose as future work to investigate the presence of ground state O atoms and O₃ molecules at the location of a remote surface since those species, which have strong oxidative capabilities, should react with remote biological or organic surfaces.

One method to detect O atoms is to use LIF with a laser wavelength in the UV region (i.e. 226 nm) to excite the O atoms and then to observe the resulting fluorescence at 844 nm [58]. In order to generate this UV wavelength, the energy of two photons must be added using the TALIF technique. The TALIF and LIF set-ups are similar (see section 1.6 and Chapter 5 for more details), but differ in the way the laser beam is generated. Since the spatial resolution of the TALIF technique is determined by the laser beam diameter, according to our knowledge, it is the only technique that can detect ground state O atoms with a resolution in the order of magnitude of less than a millimeter. However, measurements will still give a relative O atoms density.

O₃ molecules are probably reaching a remote surface since they are an important product of the reaction of O atoms produced in the plasma with O₂ molecules from the air (see Chapter 4 for more details). However, due to the very small absorption volume of the APGD-*t* plasma jet, a low concentration of O₃ is produced and; therefore, a very sensitive absorption technique, such as cavity-ring-down spectroscopy (CRDS), is needed to detect the low concentration of O₃.

b. Development of localized biomedical applications

As mentioned before, the APGD-*t* was tested for localized biomedical applications [140]. First, the APGD-*t* was used to functionalize well-defined areas (150-500 μm) of a polystyrene (Petri dish) surface to create preferential paths for the adhesion of HAAE-1 cells. In future research studies, different types of surface could be treated with the APGD-*t* to compare their capability to act as a matrix for preferential cell adhesion. Moreover, the APGD-*t* could be used to perform the inverse treatment: well-defined areas repelling adhesion of cells could be created. These treatments could be useful in the fabrication of small-scale biological drug delivery systems, artificial human cell networks for fundamental

cell studies, and as a tool to prepare plates for the immobilization of cell lines for bio-molecular research analysis.

The APGD-*t* was also used to remove, with good spatial resolution (<1 mm), HAAE-1 cells from a polystyrene (Petri dish) surface. This study could be continued by testing different cell lines and different types of surface, in order to test the APGD-*t* as a universal tool for cell removal. This treatment could be valuable in cell pathology research, cancer therapy and thin layer analysis of biological tissues.

One promising biomedical application of the APGD-*t*, which was tested by Miss Yonson, is permeabilization of cells membrane. We define cells permeabilization as a change in the molecular structure of lipids or proteins composing the cells membrane, which creates temporary pores in the membrane. The preliminary results of Miss Yonson showed that HepG2 cells, which were plasma-treated using the APGD-*t*, were able to detach from a culture dish and adhere to a new dish without necrosis. In order to test if the membrane was altered by the plasma treatment, a fluorescence biological marker, propidium iodide (PI, 668 D), was added to the cells medium of the new dish at different times after plasma treatment. It was found that PI diffused in all cells a few minutes after plasma treatment. However, when PI was added at longer time points after plasma treatment, less cells allowed PI penetration. This seems to indicate that the cell membrane was permeabilized right after plasma treatment but resealed itself after. Therefore, as an extension of this research work, the APGD-*t* could be tested to permeabilize the most common cell lines for the transport of macromolecules with different sizes and morphologies, such as DNA plasmid, proteins, quantum dots and biological markers. This future work will determine the extent of applicability of the APGD-*t* as a tool to insert materials in the cells.

We are currently developing a hand-held APGD-*t*, with a portable control unit, so that biomolecular scientists and engineers can test the potential applications of the APGD-*t* in their laboratories. This research and development project is funded by the Natural Sciences and Engineering Research Council of Canada, through the Idea to Innovation (I2I) – Phase I program.

APPENDIX A : ELECTRIC FIELD CALCULATIONS

The radial distribution of the electric field, E , inside the APGD- t has been calculated at two positions: in the plasma-forming region and at the nozzle exit. The center (powered) electrode is a stainless steel capillary tube having an outside diameter of 0.3556 mm. The ground electrode is a ~1.5 mm-thick silver epoxy layer painted onto a quartz tube having a 4 mm outside diameter in its straight section, and the downstream end is tapered into a converging nozzle ending with a 3 mm outside diameter. In helium at 1 slm, the breakdown and operating voltages were 220 V_{pk-to-0} and 405 V_{pk-to-0}, respectively. Table A-1 presents the variables used to calculate E as well as their values and units. The E distributions calculated in the straight section of the quartz tube, and at the converging nozzle exit are shown in Figure A-1. The average E at any position in the straight section of the quartz tube (plasma-forming region) is 233 kV/m and at the nozzle exit it is 322 kV/m. The use of a tapered nozzle at the end of the quartz tube allows a 38% increase in the average electric field compared to that in the straight tube geometry.

Table A-1: Data for the calculation of the electric field distribution.

Data	Symbol	Value	Units
Radial distance between electrodes	r	Variable	mm
Breakdown voltage	V_b	220	V
Operating voltage	V_{rc}	405	V
Ground electrode voltage	V_o	0	V
Capillary electrode outside radius	R_c	0.1778	mm
Quartz tube outside radius (straight section)	R_{grd}	2	mm
Quartz tube outside radius (nozzle tip)	R'_{grd}	1.5	mm
Electric field	$E(r)$	$-(V_{rc}-V_o)/(r \cdot \ln(R_c/R_{grd}))$	kV/m

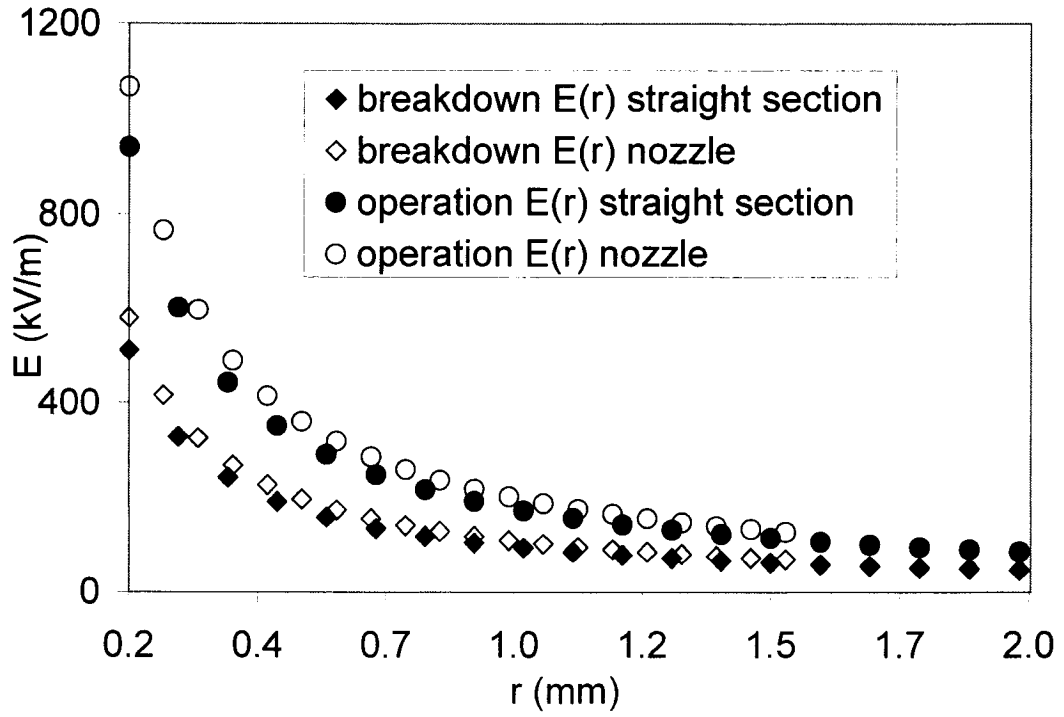


Figure: A-1: The radial distribution of the electric field, E , in the APGD- t .

APPENDIX B : THE LABVIEW™ INTERFACE

All the instruments used to operate and characterize the APGD-*t* are controlled using a virtual instrument (VI) programmed in the LabVIEW™ 6.1 environment (National Instrument™). Figure B-1 shows the block diagram with connections between the LabVIEW™ interface, the computer (Hewlett-Packard, Intel Pentium IV, 256 MB RAM, Windows 2000) and the instruments. A RF signal is generated using an arbitrary waveform generator (Hewlett-Packard 33120A, 15 MHz, 0.1-10 V_{ppk}, 12 bit, 40 MS/s) set at a carrier waveform frequency of 13.56 MHz, and which is amplitude-modulated by a variable duty-cycle pulse generator (Racal-Dana F64, 10-50% duty cycle).

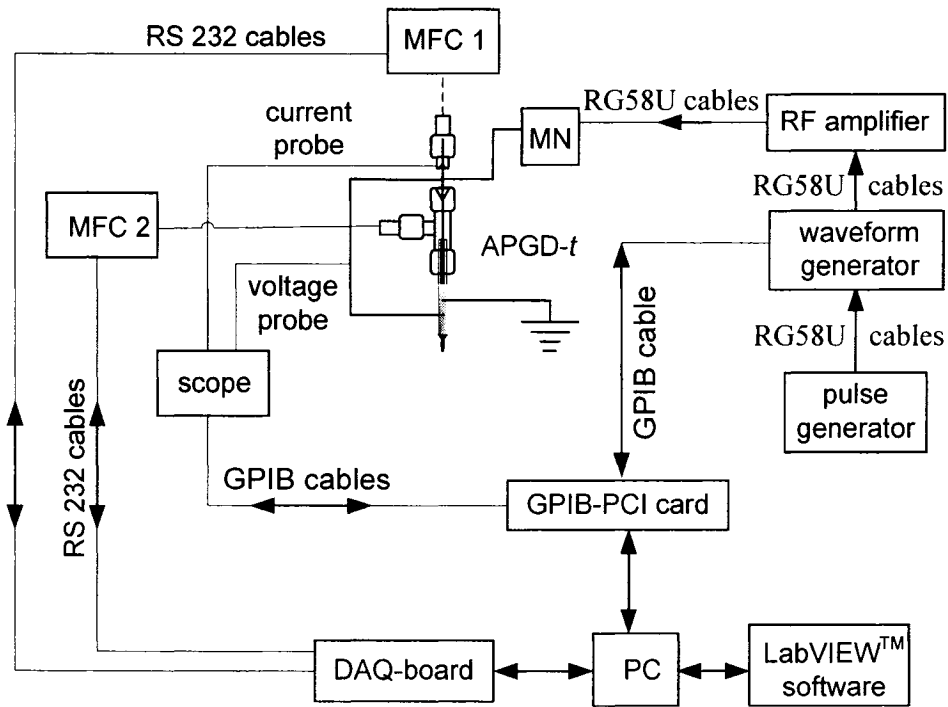


Figure B-1: Block diagram of the LabVIEW™ interface and instrumentation.

The signal is then amplified with a broadband RF amplifier (Amplifier Research 75A250, 75 W, 10 kHz-250 MHz, 50 Ω input/output impedance) and the load impedance is matched to the generator impedance using a homemade matching network (MN).

An oscilloscope (Tektronix TDS3054B, digital, 4 channels, 500 MHz, 5GS/s), a passive voltage probe (Tektronix P5100, 100X, 500 MHz, 10 M Ω , <2.75 pF) and a current probe (Tektronix CT-2 current transmitter, 1mV/1mA into 50 Ω , with Tektronix P6041 probe, 1X) are used to record the torch's voltage and circuit current, respectively. A PCI-GPIB card (National InstrumentTM, IEEE-488, 1.5 Mb/s) and GPIB shielded cables allow communication between the computer, the waveform generator and the oscilloscope. The GPIB-USB IEEE-488 drivers NI-488.2 v2.1 and NI-VISA v.3.01 (National InstrumentTM) are required to communicate with the scope and the waveform generator, respectively. The Measurement and Automation Explorer software (National InstrumentTM) is used to configure the National InstrumentTM hardware and software.

In addition, LabVIEWTM VI is used to control two mass flow controllers (MFC). The MFC 1 (Qualiflow, digital, AFC 80 MD, 0-5 VDC and 0-10 slm) is used to control the helium flow rate, and the MFC 2 (Qualiflow, digital, AFC 80 MD, 0-5 VDC and 0-50 sccm) is used to control the oxygen flow rate. The MFC are connected by RS 232 shielded cables (Sub-D 15 pins) to a PCI-DAS6025 board (Measurement ComputingTM, 16 A/D 12 bits single-ended channels, 200 kS/s, 32 digital I/O with 8 bits, 2 counters with 16 bits). LabVIEWTM VI allows to impose set-points for the flow rates of helium and oxygen and the actual (written as "present" on the VI panel) values of flow rate read by the MFCs are displayed as it is shown in the middle top section of the front panel (Figure B-2). The *InstaCal*TM and Universal Library software (Measurement and ComputingTM) are used to configure, test and calibrate the DAQ board.

The power delivered to the torch is controlled using the LabVIEW™ PID control toolset box in PI mode only. The PID parameters are set using the front panel and a waveform chart on the front panel helps to visualize the controlled process dynamics. The following aspects are considered for the PID controller tuning: (a) Minimum deviation of the actual power from the set-point, (b) avoidance of excessive variation of the PID output; (c) process control robustness for large disturbances such as an important increase in gas flow rates or power; and (d) minimum offset between power set-point and actual power.

The peak-to-peak values of the torch's voltage, circuit current and calibrated phase angle between them (see Chapter 3 for more details) are recorded on the oscilloscope and averaged over 256 samples to reduce the measurement noise. Their values are displayed in the upper left corner of the LabVIEW™ VI panel. The estimate of the actual power is calculated as the product of the torch's voltage, circuit current and cosine of the calibrated phase angle. The PID controller compares the estimated actual power to the set-point value and the PID voltage output, proportional to the difference between the actual and set-point values, is sent to the waveform generator. Consequently, the torch's voltage changes until the actual power equals the set-point. A PID control output range ($0.05 - 1.5 V_{ppk}$) is set to avoid exceeding the input voltage of the waveform generator. The bias voltage of $0.05 V_{ppk}$ is added to the PID output in order to always generate a positive voltage output.

The PID controller can be set to operate in automatic or manual mode: if set to the automatic mode, the control is done via a close loop where the PID settings are set by the user. In the manual mode, the control is done via an open loop, where the user changes the PID output directly. The response of the plasma is extremely fast ($R_p C_p \approx 1$ ns), thus the plasma responds instantaneously to a change in its voltage input. The PCI-GPIB card sampling rate is 10Mb/s, which corresponds to a

sampling period of 1 μ s. The PID VI sampling period is determined by the VI while loop execution speed, which is 1 ms by default. Those periods are much longer than the plasma time constant. To avoid any offset of the actual power, an integral action is added and the actual PID tuning parameters used are $P = 0.08$, $I = 0.1$ and $D = 0$.

A VI for the LIF measurements was also built to calculate and display the numerical integration of the laser-induced fluorescence (LIF) signal. The LIF is measured by a photomultiplier tube (Hamamatsu H6780-20, 300-900 nm, rise time = 0.78 ns, 1 $M\Omega$ and 22 pF cable output) and recorded on the oscilloscope. The oscilloscope signal is sent to the LabVIEWTM interface through a shielded GPIB cable. Another VI was built to monitor the laser energy simultaneously with the LIF signal. The laser energy is measured from a laser energy detector (Gentec-EO, QE12SP-H-MB-DO, 12 mm², 0.19-20 μ m, 8 μ J-840 mJ, 10 V/J) and the measured signal transferred to the LabVIEWTM interface using a mini USB cable. The laser energy measurements are displayed directly on the energy detector or on the LabVIEWTM front panel.

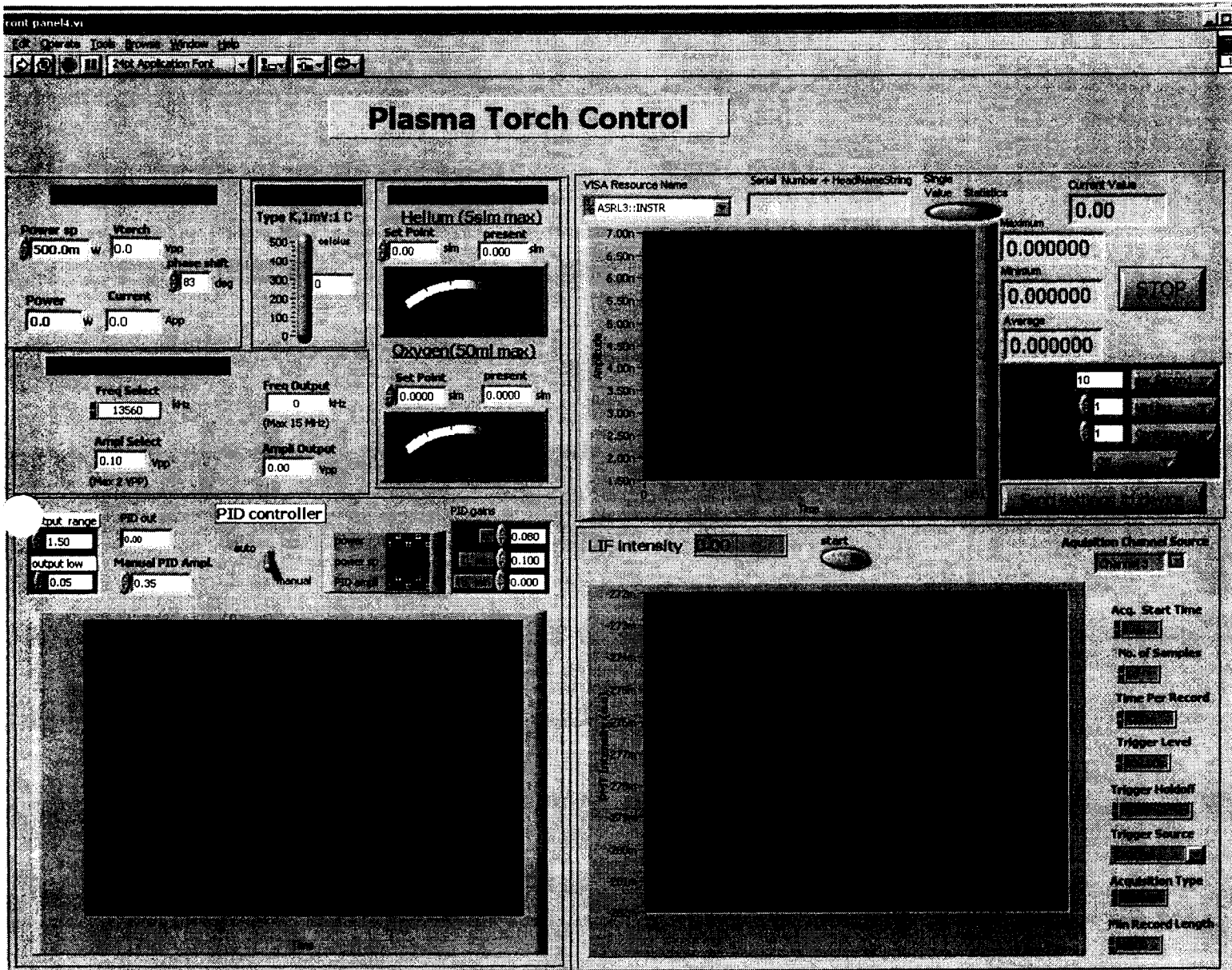


Figure B-2: Screen shot of the LabVIEW™ front panel.

APPENDIX C : EFFECT OF THE EXCITATION FREQUENCY ON THE APGD-*t* CHARACTERISTICS

At the beginning of this research project, excitation frequencies of 10 kHz and 65 kHz were used, in order to quickly and easily generate a plasma in the APGD-*t*. This step was required to obtain an estimate of the plasma properties.

Figure C-1 presents a picture of the APGD-*t* electrical set-up using plasma excitations at 10 kHz and 65 kHz. A low-frequency power generator (Eni Power System, EGR 800, 800 W max., 9-110 kHz) (not shown on the picture) is used and two voltage transformers (donated by *Plasma Technics, Inc.*) are used for plasma excitation at 10 kHz (1:120, 100 W max., 6 kV max.) and 65 kHz (1:59, 100 W max., 4 kV max.).

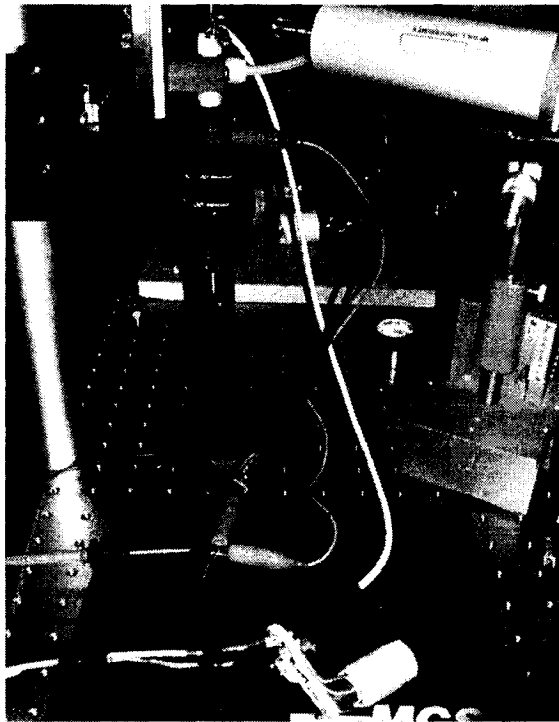


Figure C-1: Electrical set-up of the APGD-*t* for plasma excitations at 10 kHz and 65 kHz.

The torch voltage is measured using a high-voltage probe (Tektronix P6015A, 1000X, 75 MHz, 100 M Ω , 3 pF). The circuit current is obtained by measuring the voltage across a resistance (16.5 - 33 Ω), placed in series with the APGD-*t*, using a voltage probe (Tektronix, P6139A, 10X, 500 MHz, 10 M Ω , 8 pF). A different set-up is used for plasma excitation at 13.56 MHz (for details, see Chapter 2). In the set-up at 13.56 MHz, an amplitude modulator is used to reduce the average power (*P*) dissipated in the APGD-*t* and consequently, the plasma gas temperature (*T_g*).

A closer look at the APGD-*t* constructions and the plasma jets produced using the three excitation frequencies are presented in Figure C-2. One can observe a drastic reduction of the plasma jet size when excitation frequency moves toward higher frequencies.

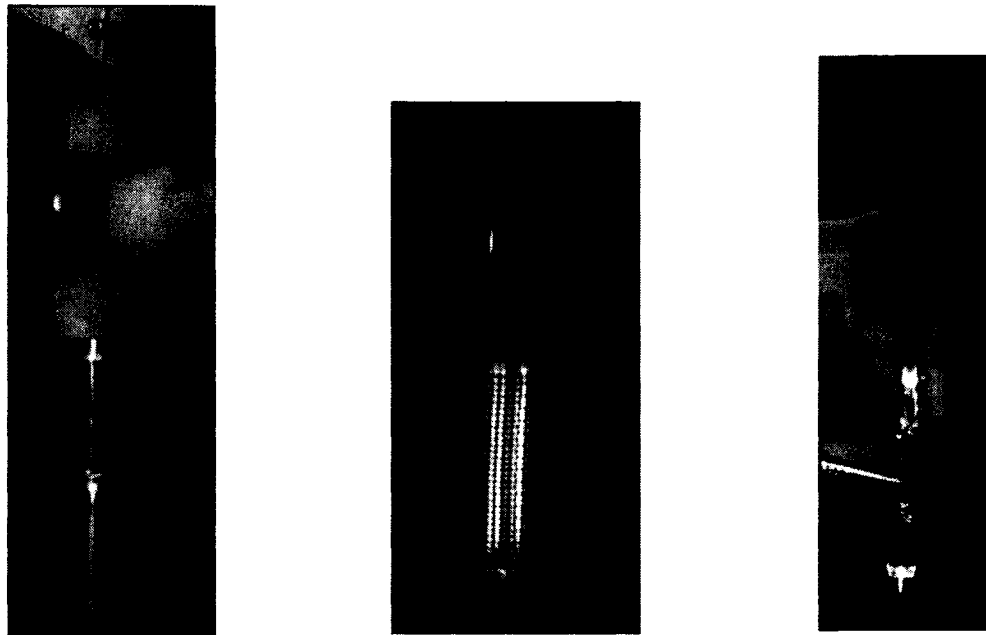


Figure C-2: Pictures of the APGD-*t* excited at 10 kHz (left), 65 kHz (middle), and 13.56 MHz (right).

Table C-1 presents a comparative summary of some characteristics of the APGD-*t* excited at 10 kHz, 65 kHz and 13.56 MHz. The APGD-*t* construction is the same for plasma excitations at 10 kHz and 65 kHz. However, the capillary electrode diameter (od) used for plasma excitation at 13.56 MHz is smaller. This change enables a geometrical enhancement of the electrical field at the electrode tip. Also, for an excitation frequency of 13.56 MHz, the quartz tube thickness (od - id) is increased in order to build a more robust APGD-*t*, and the length (L) of the capillary electrode is reduced, in order to decrease the total length of the APGD-*t*.

Table C-1: APGD-*t* characteristics at different plasma excitation frequencies.

Properties	Units	10 kHz	65 kHz	13.56 MHz
Q	slm	5	3	1
Quartz tube	od / id / L (mm)	4 / 3 / 50	4 / 3 / 50	4 / 2 / 50 0.5 mm nozzle
Capillary electrode	od / L (mm)	1.068 / 150	1.068 / 150	0.3556 / 80
Grounded electrode	od / L (mm)	~4 / 30 (sheath)	~4 / 30 (mesh)	~4 / 25 (epoxy)
U / Re	ms ⁻¹ / (-)	12 / 188	7 / 113	172 / 206
Jet	d / L (mm)	~5 / 50	~1-2 / 40-50	~0.5 / 2-3
T _g	°C	~30-35	~30-35	~25-50
V _{op} /V _b	V _{rms}	~1335 / 513	~636 / 382	~286 / 156
I	mA _{rms}	~1.5	~24	~200
P	W	~2	~17	~1

For all three excitation frequencies, helium is the plasma-forming gas and a minimum flow rate (Q) is necessary to produce a plasma jet. This flow rate is decreased from 5 slm to 1 slm when the excitation frequency changes from 10 kHz to 13.56 MHz.

The quartz tube used for the case where the plasma is excited at 13.56 MHz is tapered into a 0.5 mm nozzle exit, in order to elongate the jet and accelerate the flow. The resulting velocity (U) is increased by 10 fold compare to velocity obtained with the configuration without nozzle. The use of a nozzle also reduces the plasma jet diameter, which is beneficial for localized applications. For all cases, the flow regime is laminar (see Reynolds number in Table C-1).

Figure C-3 presents the torch voltage and circuit current waveforms for the APGD- t excited at 10 kHz. One can see small current spikes on the circuit current waveform, represented by aligned data points at random locations along the waveform. It is important to note that these waveforms were acquired with the fastest acquisition (no averaging) rate of a 500 MHz bandwidth oscilloscope, which rate corresponds to a sampling period of 2 ns. These current spikes are not observed on the circuit current waveform when an excitation frequency of 13.56 MHz is used (see Chapter 2 for an example of such waveforms).

On one hand, the increase of the plasma excitation frequency allows one to reduce the breakdown voltage (V_b) and operating voltage (V_{op}), which low voltage values favor a safer operation of the APGD- t . On the other hand, the circuit current (I) increases by 100 fold when the plasma excitation frequency increases from 10 kHz to 13.56 MHz. An increase of the current in the APGD- t plasma is not suitable for biomedical applications. Elevated plasma currents can desiccate and even burn biological tissues. However, amplitude-modulation of the current signal reduces in a controllable manner the averaged current passing through biological tissues.

It is also observed that the phase angle between the torch voltage and circuit current increases for an increasing excitation frequency. The phase angle measured at an excitation frequency of 10 kHz is $\sim 3.5^\circ$ (see Figure C-3) and $\sim 80^\circ$ for an excitation frequency of 13.56 MHz (see Chapter 2 for a description of the phase angle measurement). Simple models of the APGD-*t* electrical circuits excited at 10 kHz and 13.56 MHz reveal that an increase of the phase angle is due to an increase of the amplitude of the reactive part of the plasma impedance.

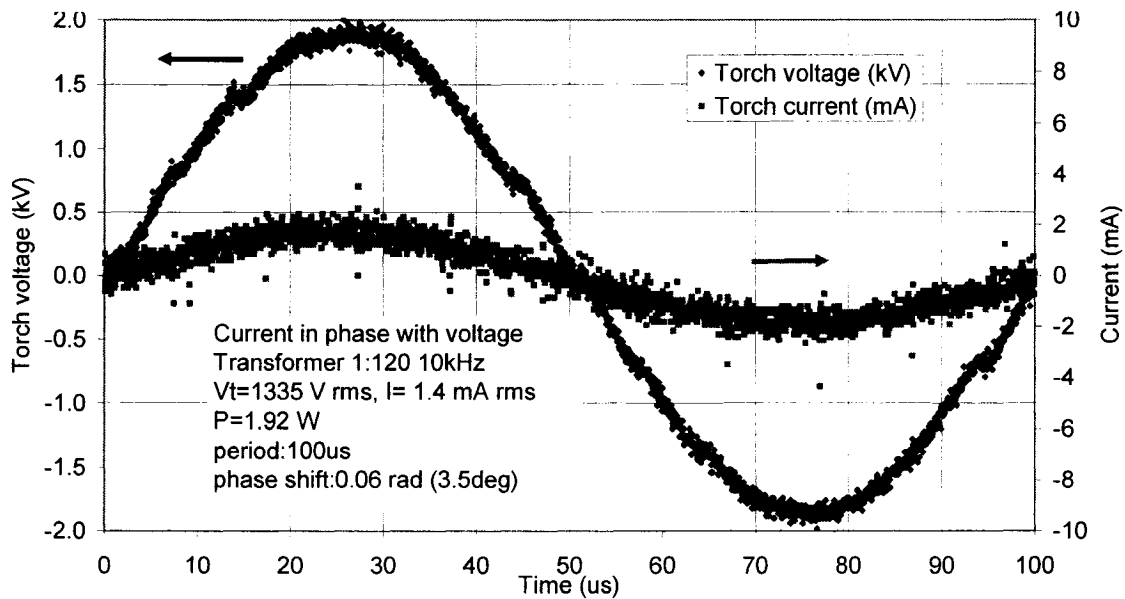


Figure C-3: Torch voltage and circuit current signals for the APGD-*t* excited at 10 kHz.

BIBLIOGRAPHY

- 1 A P Napartovich, "Overview of Atmospheric Pressure Discharges
Producing Nonthermal Plasma," *Plasmas and Polymers* **6** (1-2), 1-14
(2001).
- 2 G S Selwyn, H W Herrmann, J Park, and I Henins, "Materials Processing
Using an Atmospheric Pressure, RF-Generated Plasma Source,"
Contributions to Plasma Physics **6**, 610-619 (2001).
- 3 K H Becker, K H Schoenbach, and J G Eden, "Microplasmas and
applications," *Journal of Physics D: Applied Physics* (39), R55-R70
(2006).
- 4 Spectroscopymag: <http://www.spectroscopymag.com>
- 5 C Tendero, C Tixier, P Tristant, J Desmaison, and P Leprince,
"Atmospheric pressure plasmas: A review," *Spectrochimica Acta Part B:
Atomic Spectroscopy* **61** (1), 2-30 (2006).
- 6 T Ichiki, R Taura, and Y Horiike, "Localized and ultrahigh-rate etching of
silicon wafers using atmospheric-pressure microplasma jets," *Journal of
Applied Physics* **95** (1), 35-39 (2004).
- 7 H Koinuma, H Ohkubo, and T Hashimoto, "Development and application
of a microbeam plasma generator," *Applied Physics Letters* **60** (7), 816-
817 (1992).
- 8 J Y Jeong, S E Babayan, A Schutze, V J Tu, J Park, I Henins, G S Selwyn,
and R F Hicks, "Etching polyimide with a nonequilibrium atmospheric-
pressure plasma jet," *Journal of Vacuum Science Technology A- Vacuum,
Surfaces, and Films* **17** (5), 2581-2585 (1999).
- 9 J Park, I Henins, H W Herrmann, and G S Selwyn, "Gas breakdown in an
atmospheric pressure radio-frequency capacitive plasma source," *Journal
of Applied Physics* **89** (1), 15-19 (2001).
- 10 M H Guerra-Mutis, C V Pelaez U, and R Cabanzo H, "Glow plasma jet -
experimental study of a transferred atmospheric pressure glow discharge,"
Plasma Sources Science and Technology **12**, 165-169 (2003).
- 11 H Yoshiki, K Taniguchi, and Y Horiike, "Localized removal of a
photoresist by atmospheric pressure micro-plasma jet using RF corona
discharge," *Japanese Journal of Applied Physics* **41**, 5797-5798 (2002).
- 12 T Kikuchi, Y Hasegawa, and H Shirai, "RF microplasma jet at
atmospheric pressure: characterization and application to thin film
processing," *Journal of Physics D: Applied Physics* **37**, 1537-1543 (2004).

- 13 J Janca, L Zajickova, M Klima, and P Slavicek, "Diagnostics and Application of the High Frequency Plasma Pencil," *Plasma Chemistry and Plasma Processing* **21** (4), 565-579 (2001).
- 14 Q Jin, C Zhu, M W Borer, and G M Hieftje, "A microwave plasma torch assembly for atomic emission spectrometry," *Spectrochimica Acta B: Atomic Spectroscopy* **46**, 417-430 (1991).
- 15 R Stonies, S Schermer, E Voges, and J A C Broekaert, "A new small microwave plasma torch," *Plasma Sources Science and Technology* **13** (4), 604-611 (2004).
- 16 A M Bilgic, C Prokisch, J A C Broekaert, and E Voges, "Design and modelling of a modified 2.45 GHz coaxial plasma torch for atomic spectrometry," *Spectrochimica Acta B: Atomic Spectroscopy* **53**, 773-777 (1998).
- 17 R Konavko, A Konavko, and H Schmid, US10/236,747 Patent No. 518 (March 13 2003).
- 18 Plasmabrush(R) <http://www.reinhausen-plasma.com/plasma/en/produkte/>
- 19 K Schröder, A Meyer-Plath, D Keller, and A Ohl, "On the Applicability of Plasma Assisted Chemical Micropatterning to Different Polymeric Biomaterials," *Plasmas and Polymers* **7** (2), 103-125 (2002).
- 20 I G Brown, K A Bjornstad, E A Blakely, J E Galvin, O R Monteiro, and S Sangyuenyongpipat, "Growth of large patterned arrays of neurons using plasma methods," *Plasma Physics and Controlled Fusion* **45** (5), 547-554 (2003).
- 21 M Laroussi, D A Mendis, and M Rosenberg, "Plasma interaction with microbes," *New Journal of Physics* **5**, 41.41 - 41.10 (2003).
- 22 J R Roth, D M Sherman, R Ben Gadri, F Karakaya, Z Chen, T C Montie, K Kelly-Wintenberg, and P P-Y Tsai, "A Remote Exposure Reactor (RER) for Plasma Processing and Sterilization by Plasma Active Species at One Atmosphere," *IEEE Transactions on Plasma Science* **28** (1), 56-63 (2000).
- 23 A Bruil, L M Brenneisen, J G A Terlingen, T Beugeling, W G van Aken, and J Feijen, "*In Vitro* Leukocyte Adhesion to Modified Polyurethane Surfaces: II. Effect of Wettability," *Journal of Colloid and Interface Science* **165** (1), 72-81 (1994).
- 24 K E Schmalenberg, H M Buettner, and K E Uhrich, "Microcontact printing of proteins on oxygen plasma-activated poly (methyl methacrylate)," *Biomaterials* **25**, 1851-1857 (2004).

- 25 M Kuzuya, S-I Kondo, and Y Sasai, "Plasma Techniques for Preparation of Controlled Drug Release System," *Plasmas and Polymers* **6** (3), 145-162 (2001).
- 26 D Storek, K E Grund, G Gronbach, G Farin, and H D Becker, "Endoskopische Argon-Gas-Koagulation-erste klinische Erfahrungen " *Zeitschrift für Gastroenterologie (German)* **31**, 675-679 (1993).
- 27 J C Letard, "La coagulation au plasma Argon (APC)," *Acta Endoscopica* **30 S2** (3), 414-415 (2000).
- 28 J Schreiber, B Hofman, H J Schumann, and W Rosahl, "Influence of Oxygen Concentration on Argon Plasma Coagulation-Induced Tissue Damage in Isolated Pig Tracheas," *Respiration* **67**, 287-290 (2000).
- 29 E Stoffels, I E Kieft, and R E J Sladek, "Superficial treatment of mammalian cells using plasma needle," *Journal of Physics D: Applied Physics* **36** (23), 2908-2913 (2003).
- 30 E Stoffels, A J Flikweert, W W Stoffels, and G M W Kroesen, "Plasma needle: a non-destructive atmospheric plasma source for fine surface treatment of (bio)materials," *Plasma Sources Science and Technology* **11** (4), 383-388 (2002).
- 31 I E Kieft, E P v d Laan, and E Stoffels, "Electrical and optical characterization of the plasma needle," *New Journal of Physics* **6** (149), 1-14 (2004).
- 32 I E Kieft, J L V Broers, V Caubet-Hilloutou, D W Slaaf, F C S Ramaekers, and E Stoffels, "Electric discharge plasmas influence attachment of cultured CHO K1 cells," *Bioelectromagnetics* **25** (5), 362-368 (2004).
- 33 M Laroussi and X Lu, "Room-temperature atmospheric pressure plasma plume for biomedical applications," *Applied Physics Letters* **87** (113902), 1-3 (2005).
- 34 C C O Goble, K Penny, C Hancock, and F Amoah, US09/789,550 Patent No. 6,723,091 B2 (April 20 2004).
- 35 R M Clements, "Plasma diagnostics with electric probes," *Journal of Vacuum Science and Technology* **15** (2), 193-198 (1978).
- 36 J S Logan, N M Mazza, and P D Davidse, "Electrical Characterization of Radio-Frequency Sputtering Gas Discharge," *Journal of Vacuum Science and Technology* **6** (1), 120-123 (1969).
- 37 W E Mlynko and D W Hess, "Electrical characterization of RF glow discharges using an operating impedance bridge," *Journal of Vacuum*

- Science and Technology A: Vacuum, Surfaces, and Films **3** (3), 499-503 (1985).
- 38 ABCs of Probes, Tektronix, 48,
http://www.tek.com/Masurement/App_Notes/ABCsProbes/60W_6053_9.pdf.
- 39 Rohde & Schwarz: <http://www.rohde-schwarz.com>
- 40 Agilent Technology: <http://www.home.agilent.com>
- 41 R Brandenburg, V A Maiorov, Y B Golubovskii, H-E Wagner, J Behnke, and J F Behnke, "Diffuse barrier discharges in nitrogen with small admixtures of oxygen: discharge mechanism and transition to the filamentary regime," *Journal of Physics D: Applied Physics* **38** (13), 2187-2197 (2005).
- 42 G Fortunato, "End-point determination by reflected power monitoring," *Journal of Physics E: Scientific Instruments* **20** (8), 1051-1052 (1987).
- 43 Z-Scan RF probe: <http://www.advanced-energy.de>
- 44 W-C Zhu, B-R Wang, Z-X Yao, and Y-K Pu, "Discharge characteristics of an atmospheric pressure radio-frequency plasma jet," *Journal of Physics D: Applied Physics* (9), 1396 (2005).
- 45 S Wang, V Schulz-von der Gathen, and H F Dobeles, "Discharge comparison of non-equilibrium atmospheric pressure Ar/O₂ and He/O₂ plasma jets," *Applied Physics Letters* **83** (16), 3272-3274 (2003).
- 46 R Rahul, O Stan, A Rahman, E Littlefield, K Hoshimiya, A P Yalin, A Sharma, A Pruden, C A Moore, Z Yu, and G J Collins, "Optical and RF electrical characteristics of atmospheric pressure open-air hollow slot microplasmas and application to bacterial inactivation," *Journal of Physics D: Applied Physics* **38** (11), 1750-1759 (2005).
- 47 M A Sobolewski, "Electrical characterization of radio-frequency discharges in the Gaseous Electronics Conference Reference Cell," *Journal of Vacuum Science and Technology A* **10** (6), 3550-3562 (1992).
- 48 S Vacquié, *L'arc électrique*, 1st Ed. (Centre national de la recherche scientifique, Paris, 2000), pp.237-253.
- 49 W Demtröder, *Laser Spectroscopy: Basic Concepts and Instrumentation*, 3rd Ed. (Springer-Verlag, Berlin, 2002), p.987.
- 50 M A A Clyne and I S McDermid, *Dynamics of the Excited State*. (John Wiley & Sons Ltd, New York, 1982), p.667.
- 51 M Minsky, US Patent No. 3,013,467 (1961).

- 52 A Schultz, H W Cruse, and R N Zare, "Laser-Induced Fluorescence: A Method to Measure the Internal State Distribution of Reaction Products," *The Journal of Chemical Physics* **57** (3), 1354-1355 (1972).
- 53 K H Becker, U Schurath, and T Tatarczyk, "Fluorescence Determination of Low Formaldehyde Concentrations in Air by Dye Laser Excitation," *Applied Optics* **14** (2), 310-313 (1975).
- 54 C C Wang and L I Davis Jr., "Measurement of Hydroxyl Concentrations in Air Using a Tunable uv Laser Beam," *Physical Review Letters* **32** (7), 349-352 (1974).
- 55 I S McDermid and J B Laudenslager, "Perturbations in the $B^3\Pi(0^+)$ state of ClF: A new low-lying electronic state," *Chemical Physics Letters* **79** (2), 370-374 (1981).
- 56 R A Stern and J A I Johson, "Plasma Ion Diagnostics Using Resonant Fluorescence," *Physical Review Letters* **34** (25), 1548-1551 (1975).
- 57 X Hu, G-B Zhao, S V B Janardhan Garikipati, K Nicholas, S F Legowski, and M Radosz, "Laser-Induced Fluorescence (LIF) Probe for *in-situ* Nitric Oxide Concentration Measurement in a Non-thermal Pulsed Corona Discharge Plasma Reactor," *Plasma Chemistry and Plasma Processing* **25** (4), 351-370 (2005).
- 58 K Niemi, V S-v der Gathen, and H F Döbele, "Absolute atomic oxygen density measurements by two-photon absorption laser-induced fluorescence spectroscopy in an RF-excited atmospheric pressure plasma jet," *Plasma Sources Science and Technology* **14** (2), 375-386 (2005).
- 59 M G H Boogaarts, S Mazouffre, G J Brinkman, H W P van der Heijden, P Vankan, J A M van der Mullen, D C Schram, and H F Döbele, "Quantitative two-photon laser-induced fluorescence measurements of atomic hydrogen densities, temperatures, and velocities in an expanding thermal plasma," *Review of Scientific Instruments* **73** (1), 73-86 (2002).
- 60 R Ono and T Oda, "Measurement of hydroxyl radicals in pulsed corona discharge," *Journal of Electrostatics* **55** (3-4), 333-342 (2002).
- 61 W K Bischel, B E Perry, and D R Crosley, "Two-photon laser-induced fluorescence in oxygen and nitrogen atoms," *Chemical Physics Letters* **82** (1), 85-88 (1981).
- 62 L Magne and S Pasquiers, "LIF spectroscopy applied to the study of non-thermal plasmas for atmospheric pollutant abatement," *Comptes Rendus Physique* **6** (8), 908-917 (2005).
- 63 S De Benedictis and G Dilecce, "Laser-induced fluorescence measurements of $He(2^3S)$ decay in $He-N_2/O_2$ pulsed RF discharges:

- Penning ionization," *Journal of Physics D: Applied Physics* **28**, 2067-2076 (1995).
- 64 W M Fairbank Jr, T W Haensch, and A L Schawlow, "Absolute measurement of very low sodium vapor densities using laser resonance fluorescence," *Journal of the Optical Society of America* **65**, 199-204 (1975).
- 65 K Tsuchida, "Density Measurement of Helium Metastable Atoms in Plasma by the Laser-Induced Fluorescence Method," *Japanese Journal of Applied Physics* **23** (3), 338-345 (1984).
- 66 D Lee, J M Park, S H Hong, and Y Kim, "Numerical Simulation on Mode Transition of Atmospheric Dielectric Barrier Discharge in Helium-Oxygen Mixture," *IEEE Transactions on Plasma Science* **33** (2), 949-957 (2005).
- 67 E A Den Hartog, T R O'Brian, and J E Lawler, "Electron Temperature and Density Diagnostics in a Helium Glow Discharge," *Physical Review Letters* **62** (13), 1500-1503 (1989).
- 68 S De Benedictis and G Dilecce, "Relaxation of excited species in He/N₂ pulsed RF discharges: kinetics of metastable species," *Plasma Sources Science and Technology* **4**, 212-223 (1995).
- 69 G Herzberg, *Atomic Spectra and Atomic Structure* (Dover publications, New York 1945), p.257.
- 70 K B Boudam, Master thesis, Université de Montréal, Montréal (Québec) Canada, 2002.
- 71 J Jolly, M Touzeau, and A Ricard, "Determination of non-Boltzmann vibrational level populations of excited nitrogen using the Penning ionisation technique," *Journal of Physics B: Atomic and Molecular Physics* **14** (3), 473-481 (1981).
- 72 G Nersisyan, T Morrow, and W G Graham, "Measurements of helium metastable density in an atmospheric pressure glow discharge," *Applied Physics Letters* **85** (9), 1487-1489 (2004).
- 73 V Léveillé and S Coulombe, "Design and preliminary characterization of a miniature pulsed RF APGD torch with downstream injection of the source of reactive species," *Plasma Sources Science and Technology* **14** (3), 467-476 (2005).
- 74 V Poenariu, M R Wertheimer, and R Bartnikas, "Spectroscopic Diagnostics of Atmospheric Pressure Helium Dielectric Barrier Discharges in Divergent Fields," *Plasma Processes and Polymers* **3** (1), 17-29 (2006).

- 75 J H Kim, Y H Kim, Y H Choi, W Choe, J J Choi, and Y S Hwang, "Optical measurements of gas temperatures in atmospheric pressure RF cold plasmas," *Surface and Coatings Technology* **171** (1-3), 211-215 (2002).
- 76 I E Kieft, M Kurdi, and E Stoffels, "Reattachment and Apoptosis After Plasma-Needle Treatment of Cultured Cells," *Plasma Science, IEEE Transactions on* **34** (4), 1331-1336 (2006).
- 77 M Laroussi, "Sterilization of contaminated matter with an atmospheric pressure plasma," *IEEE Transactions on Plasma Science* **24** (3), 1188-1191 (1996).
- 78 T Yokoyama, M Kogoma, T Moriwaki, and S Okazaki, "The mechanism of the stabilisation of glow plasma at atmospheric pressure," *Journal of Physics D: Applied Physics* **23**, 1125-1128 (1990).
- 79 F Massines, G Gouda, N Gherardi, M Duran, and E Croquesel, "The Role of Dielectric Barrier Discharge Atmosphere and Physics on Polypropylene Surface Treatment," *Plasmas and Polymers* **6** (1 - 2), 35-49 (2001).
- 80 S Moreau, M Moisan, M Tabrizian, J Barbeau, J Pelletier, A Ricard, and L H Yahia, "Using the flowing afterglow of a plasma to inactivate *Bacillus subtilis* spores: Influence of the operating conditions," *Journal of Applied Physics* **88** (2), 1166-1174 (2000).
- 81 M Moisan, J Barbeau, S Moreau, J Pelletier, M Tabrizian, and L H Yahia, "Low-temperature sterilization using gas plasmas: a review of the experiments and an analysis of the inactivation mechanisms," *International Journal of Pharmaceutics* **226**, 1-21 (2001).
- 82 K Kelly-Wintenberg, T C Montie, C Brickman, J R Roth, A K Carr, K Sorge, and P P-Y Tsai, "Room temperature sterilization of surfaces and fabrics with a One Atmosphere Uniform Glow Discharge Plasma," *Journal of Industrial Microbiology & Biotechnology* **20**, 69-74 (1998).
- 83 NIST Handbook of Atomic Spectroscopic Data
<http://physics.nist.gov/PhysRefData/Handbook>
- 84 K L Bell, A Dalgarno, and A E Kingston, "Penning ionization by metastable helium atoms," *Journal of Physics B: Atomic and Molecular Physics* **1** (2), 18-22 (1968).
- 85 R B Bird, W E Stewart, and E N Lightfoot, *Transport phenomena*. (John Wiley & Sons, New-York 1960), p.780.
- 86 S C Brown, *Basic Data of Plasma Physics*. (Technology Press of the Massachusetts Institute of Technology Cambridge 1959), p.336.

- 87 H J Baker, "Direct measurement of the electrical impedance of narrow gap radio frequency gas discharges in the 100 MHz region," *Measurement Science and Technology* **7** (11), 1631-1635 (1996).
- 88 D DeMaw, *The Radio Amateur's Handbook*, 56th Ed. (W1FB American Radio relay league, Newington, 1979), pp.2-11.
- 89 K R Stalder, D F McMillen, and J Woloszko, "Electrosurgical plasmas," *Journal of Physics D: Applied Physics* **38** (11), 1728-1738 (2005).
- 90 D Ziegler, P Mayer, K Wiefels, and F A Gries, "Assessment of small and large fiber function in long-term type 1 (insulin-dependent) diabetic patients with and without painful neuropathy," *Pain* **34**, 1-10 (1988).
- 91 R D Adams, M Victor, and A H Ropper, *Principles of neurology*. (McGraw Hill Inc., New York, 1993), p.1171.
- 92 A G Gaydon, *The spectroscopy of flames*. (Chapman & Hall Ltd., London, 1957), p.279.
- 93 Y-H Lee, C-H Yi, M-J Chung, and G-Y Yeom, "Characteristics of He/O₂ atmospheric pressure glow discharge and its dry etching properties of organic materials," *Surface and Coatings Technology* **146-147**, 474-479 (2001).
- 94 D-c Seo and T-h Chung, "Observation of the transition of operating regions in a low-pressure inductively coupled oxygen plasma by Langmuir probe measurement and optical emission spectroscopy," *Journal of Physics D: Applied Physics* **34** (18), 2854-2861 (2001).
- 95 K Tanabe, H Haraguchi, and K Fuwa, "Some spatial characteristics of an atmospheric pressure helium microwave-induced plasma," *Spectrochimica Acta B: Atomic Spectroscopy* **38** (1-2), 49-60 (1983).
- 96 G Nersisyan and W G Graham, "Characterization of a dielectric barrier discharge operating in an open reactor with flowing helium," *Plasma Sources Science and Technology* **13** (4), 582-587 (2004).
- 97 H Yoshiki and Y Horiike, "Capacitively Coupled Microplasma Source on a Chip at Atmospheric Pressure," *Japanese Journal of Applied Physics* **40** (Part 2 4A), L360-L362 (2001).
- 98 The MATHWORKS: <http://www.mathworks.com/>
- 99 W-C Zhu, B-R Wang, Z-X Yao, and Y-K Pu, "Discharge characteristics of an atmospheric pressure radio-frequency plasma jet," *Journal of Physics D: Applied Physics* **38** (9), 1396-1401 (2005).
- 100 P J Hargis Jr, K E Greenberg, P A Miller, J B Gerardo, J R Torczynski, M E Riley, G A Hebner, J R Roberts, J K Olthoff, J R Whetstone, R J Van Brunt, M A Sobolewski, H M Anderson, M P Splichal, J L Mock, P

- Bletzinger, A Garscadden, R A Gottscho, G Selwyn, M Dalvie, J E Heidenreich, J W Butterbaugh, M L Brake, M L Passow, J Pender, A Lujan, M E Elta, D B Graves, H H Sawin, M J Kushner, J T Verdeyen, R Horwath, and T R Turner, "The Gaseous Electronics Conference radio-frequency reference cell: A defined parallel-plate radio-frequency system for experimental and theoretical studies of plasma-processing discharges," *Review of Scientific Instruments* **65** (1), 140-154 (1994).
- ¹⁰¹ Z Chen, "Impedance matching for one atmospheric uniform glow discharge plasma (OAugDP) reactors," *IEEE Transactions on Plasma Science* **30** (5), 1922-1929 (2002).
- ¹⁰² W Guo and C A DeJoseph Jr, "Time-resolved current and voltage measurements on a pulsed rf inductively coupled plasma," *Plasma Sources Science and Technology* **10** (1), 43-51 (2001).
- ¹⁰³ I E Kieft, D Darios, A J M Roks, and E Stoffels, "Plasma Treatment of Mammalian Vascular Cells: A Quantitative Description," *IEEE Transactions on Plasma Science* **33** (2), 771-775 (2005).
- ¹⁰⁴ S Coulombe, V Léveillé, R Leask, and S Yonson, US Appli. No. #11/383,581 (May 16 2006 2006).
- ¹⁰⁵ F Clément, B Held, N Soulem, and C Guimon, "Plasmas, discharges and processes - XPS analyses of polystyrene thin films treated under DC pulsed discharges conditions in nitrogen, oxygen and oxygen-argon mixtures," *The European Physical Journal - Applied Physics* **18** (2), 135-151 (2002).
- ¹⁰⁶ S Coulombe, V Léveillé, S Yonson, and R L Leask, "A miniature atmospheric pressure glow discharge torch (APGD-*t*) for local biomedical applications," *Pure and Applied Chemistry* **78** (6), 1137-1146 (2005).
- ¹⁰⁷ M A Lieberman and A J Lichtenberg, *Principles of Plasma Discharges and Materials Processing*. (John Wiley & Sons Inc., New York, 1994), pp.255-256.
- ¹⁰⁸ C Gorse, S De Benedictis, G Dilecce, and M Capitelli, "Electron energy distribution functions in He/N₂ mixtures in the presence of metastable states," *Spectrochimica Acta B: Atomic Spectroscopy* **45** (4-5), 521-525 (1990).
- ¹⁰⁹ A Kunde, N J Wiegart, and H-J Kunze, "A quantitative study of the role of molecular impurities in the emission spectroscopy of He I in pulsed discharges," *Journal of Physics B: Atomic and Molecular Physics* **18** (3), 567-576 (1985).
- ¹¹⁰ J M Pouvesle, A Bouchoule, and J Stevefelt, "Modeling of the charge transfer afterglow excited by intense electrical discharges in high pressure

- helium nitrogen mixtures," *The Journal of Chemical Physics* **77** (2), 817-825 (1982).
- 111 S V Kvitov, B N Lomakin, V R Solov'ev, A A Sunarchin, M G Tikhonov, and N V Cherkasskii, "Relaxation of a Low-Temperature Helium Plasma Produced by a Pulsed Electron Beam in a Large-Volume Chamber," *Fizika Plazmy* (Russian) **22**, 1134 (1996).
- 112 C Lee, D B Graves, M A Lieberman, and D W Hess, "Global Model of Plasma Chemistry in a High Density Oxygen Discharge," *Journal of The Electrochemical Society* **141** (6), 1546-1555 (1994).
- 113 B Eliasson and U Kogelschatz, Report No. KLR-11C CH5405, 1986.
- 114 S T Amimoto, A P Force, and J R Wiesenfeld, "Ozone photochemistry: production and deactivation of O(2^1D_2) following photolysis at 248 nm," *Chemical Physics Letters* **60** (1), 40-43 (1978).
- 115 J Heicklen, *Atmospheric chemistry*. (Academic press, New York, 1976), p.406.
- 116 R F Heidner III, D Husain, and J R Wiesenfeld, "Kinetic study of electronically excited oxygen atoms, O(2^1D_2), by time-resolved atomic absorption spectroscopy in the vacuum ultra-violet ($\lambda=115.2$ nm, O($3^1D_2^0 \rightarrow 2^1D_2$)," *Chemical Physics Letters* **16** (3), 530-533 (1972).
- 117 R Atkinson, D L Baulch, R A Cox, R F Hampson Jr, J A Kerr, M J Rossi, and J Troe, "Evaluated kinetic and photochemical data for atmospheric chemistry: supplement VI. IUPAC subcommittee on gas kinetic data evaluation for atmospheric chemistry," *Journal of Physical and Chemical Reference Data* **26**, 1329-1499 (1997).
- 118 H G Yu and A J C Varandas, "Dynamics of H(D) + O₃ reactions on a double many-body expansion potential-energy surface for ground state HO₃," *Journal of the Chemical Society, Faraday Transactions* **93** (16), 2651-2656 (1997).
- 119 K Schofield, "The Rate of Destruction of O₂ ($^1\Delta_g$) by Atomic Hydrogen," *International Journal of Chemical Kinetics* **4** (3), 255-263 (1972).
- 120 S P Sharma, B A Cruden, M V V S Rao, and A A Bolshakov, "Analysis of emission data from O₂ plasmas used for microbe sterilization," *Journal of Applied Physics* **95** (7), 3324-3333 (2004).
- 121 S W Benson and A E Axworthy Jr, "Mechanism of the Gas Phase, Thermal Decomposition of Ozone," *The Journal of Chemical Physics* **26** (6), 1718-1726 (1957).

- 122 R K Datta and K N Rao, "Kinetics of Reactions of Singlet Molecular Oxygen(1g) with Organic Compounds," *Indian Journal of Chemistry A* **18**, 102-105 (1979).
- 123 D L Baulch, C J Cobos, R A Cox, P Frank, G Hayman, T Just, J A Kerr, T Murrells, M J Pilling, J Troe, R W Walker, and J Warnatz, "Evaluated Kinetic Data for Combustion Modelling. Supplement I," *Journal of Physical and Chemical Reference Data* **23** (6), 847-1033 (1994).
- 124 R F Barrow, D A Long, and D J Millen, *Molecular Spectroscopy* (Billing & Sons Limited, London, 1974), p.579.
- 125 S Hatakeyama and M-T Leu, "Rate constants for reactions between atmospheric reservoir species. 2. H₂O," *Journal of Physical Chemistry A* **93**, 5784-5789 (1989).
- 126 W Tsang and R F Hampson, "Chemical Kinetic Data Base for Combustion Chemistry. Part I. Methane and Related compounds," *Journal of Physical and Chemical Reference Data* **15** (3), 1087-1279 (1986).
- 127 J T Gudmundsson, "Recombination and detachment in oxygen discharges: the role of metastable oxygen molecules," *Journal of Physics D: Applied Physics* **37** (15), 2073-2081 (2004).
- 128 F W Lee and C B Collins, "Measurement of the rate coefficients for the bimolecular and termolecular de-excitation reactions of He(2³S) with Ne, Ar, N₂, CO, CO₂, and CH₄," *The Journal of Chemical Physics* **65** (12), 5189-5197 (1976).
- 129 Y B Golubovskii, V A Maiorov, J Behnke, and J F Behnke, "Modelling of the homogeneous barrier discharge in helium at atmospheric pressure," *Journal of Physics D: Applied Physics* **36** (1), 39-49 (2003).
- 130 K Thielen and P Roth, "N atom measurements in high-temperature N₂ dissociation kinetics," *American Institute of Aeronautics and Astronautics Journal* **24** (7), 1102-1105 (1986).
- 131 V Nemchinsky, "Dissociation reactive thermal conductivity in a two-temperature plasma," *Journal of Physics D: Applied Physics* **38** (20), 3825-3831 (2005).
- 132 Q Chen, Y Zhang, E Han, and Y Ge, "Atmospheric pressure DBD gun and its application in ink printability," *Plasma Sources Science and Technology* **14** (4), 670-675 (2005).
- 133 P Zhang and U Kortshagen, "Two-dimensional numerical study of atmospheric pressure glows in helium with impurities," *Journal of Physics D: Applied Physics* **39** (1), 153-163 (2006).

- 134 J M Pouvesle, A Khacef, J Stevefelt, H Jahani, V T Gylys, and C B
Collins, "Study of two-body and three-body channels for the reaction of
metastable helium atoms with selected atomic and molecular species," *The
Journal of Chemical Physics* **88** (5), 3061-3071 (1988).
- 135 W S Struve, *Fundamentals of Molecular Spectroscopy*. (John Wiley &
Sons Inc., New York, 1989), p.379.
- 136 A A Frimer, *Singlet O₂: Physical-Chemical Aspects*. (Chemical Rubber
Company, Boca Raton, Florida, 1985), p.248.
- 137 B Eliasson and U Kogelschatz, "Nonequilibrium Volume Plasma
Chemical Processing," *IEEE Transactions on Plasma Science* **19** (6),
1063-1077 (1991).
- 138 J Y Jeong, J Park, I Henins, S E Babayan, V J Tu, G S Selwyn, G Ding,
and R F Hicks, "Reaction Chemistry in the Afterglow of an Oxygen-
Helium, Atmospheric-Pressure Plasma," *Journal of Physical Chemistry A*
104, 8027-8032 (2000).
- 139 R Álvarez, M C Quintero, and A Rodero, "Radial description of excitation
processes of molecular and atomic species in a high-pressure helium
microwave plasma torch," *Journal of Physics D: Applied Physics* **38** (20),
3768-3777 (2005).
- 140 S Yonson, S Coulombe, V Léveillé, and R L Leask, "Cell treatment and
surface functionalization using a miniature atmospheric pressure glow
discharge plasma torch," *Journal of Physics D: Applied Physics* **39** (16),
3508-3513 (2006).